Diagnostics and control of complex plasmas by means of tunable lasers

Aleksandr Pikalev

München 2021

Diagnostics and control of complex plasmas by means of tunable lasers

Aleksandr Pikalev

Dissertation
an der Fakultät für Physik
der Ludwig-Maximilians-Universität
München

vorgelegt von
Aleksandr Pikalev
aus Petrosawodsk, Russland

München, den 28. Oktober 2021

Erstgutachter: PD Dr. Christoph Räth
Zweitgutachter: PD Dr. Alexei Ivlev
Tag der mündlichen Prüfung: den 13. Dezember 2021

Contents

List of Figures

List of Tables

Abbreviations

1D, 2D, 3D — one-dimensional, two-dimensional, three-dimensional.

CCRF — Capacitively coupled radio frequency.

COMPACT — COMplex PlAsma faCiliTy.

DC — Direct current.

DDW — Dust density waves.

DLR — Deutsches Zentrum für Luft- und Raumfahrt (German Aerospace Center).

ICCD — Intensified charge-coupled device

IDF — Ion drag force.

ISS — International Space Station.

LIF — Laser induced fluorescence.

MF — Melamine formaldehyde.

OML — Orbital-motion limited.

PIC — Particle-in-cell.

PK-3 Plus — Plasmakristall-3 Plus.

PK-4 — Plasmakristall-4.

PKE — Plasmakristall-Experiment.

PROES — Period/phase-resolved optical emission spectroscopy.

RF — Radio frequency

TDLAS — Tunable diode laser absorption spectroscopy.

Zusammenfassung

Komplexe oder staubige Plasmen sind elektroneutrale Medien, die ionisiertes Gas und Mikroteilchen enthalten. Sie sind weitverbreitet in der Natur (Leuchtende Nachtwolke, Planetenringe, Kometen usw.) und Industrie (Plasmarand im Tokamak, Herstellung von Nanoteilchen, Plasmaätzen und plasmagestützte Abscheidung). Flüsse von Elektronen und Ionen auf die Mikroteilchen laden sie elektrisch auf. Deswegen wechselwirken die Mikroteilchen im Plasma miteinander und können stark gekoppelte Subsysteme bilden. Man benutzt sie, um generische Phänomene in klassischer kondensierter Materie auf dem Partikelniveau zu untersuchen. Gleichzeitig beeinflussen die Mikroteilchen andere Komponenten des Plasmas und ändern oft wesentlich die Gegebenheiten im Plasma. In dieser kumulativen Dissertation geht es um die Untersuchung der Interaktionen zwischen den Mikroteilchen und Plasmen in einer kapazitiv gekoppelten HF-Entladung in Argon.

Mittels der Diodenlaser-Absorptionsspektroskopie (tunable diode laser absorption spectroscopy, TDLAS) detektierten wir kleine mikroteilcheninduzierte Erhitzung des Gases und bestimmten die Wirkung der Mikroteilchen auf die Dichte der metastabilen Atome. Dann versuchten wir die Einschränkungen der Absorptionsspektroskopie mittels planarer laserinduzierter Fluoreszenz zu bewältigen. Dadurch erhielten wir eine zweidimensionale Verteilung der Dichte der metastabilen Atome.

Gleichzeitige Beobachtungen der Anordnung der Mikroteilchen und der Plasmaemission zeigten, dass das Void (ein Raum innerhalb der Mikroteilchenwolke ohne Mikroteilchen) in zwei Formen existieren kann, die wir "matt" ("dim") und "hell"("bright") nannten. Das matte Void entspricht niedrigen Entladungsleistungen und zeichnet sich durch ein diffuses Emissionsprofil in und um das Void aus. Das helle Void entspricht höheren Entladungsleistungen und hat helle Plasmaemission in seinem Inneren. Der Übergang des Voids von der matten zur hellen Erscheinungsform erfolgte diskontinuierlich und wies einen Knick in der Abhängigkeit der Voidgröße von der Entladungsleistung auf. Eine Modellierung lieferte Hinweise, dass sich die Bildungsmechanismen des Voids für die beiden Erscheinungsformen qualitative unterschieden: Im hellen Void heizt ein starkes, zeitlich gemitteltes elektrisches Feld an der Grenze des Voids die Elektronen. Für das matte Void ist das Feld viel schwächer, und die radiale Diffusion spielt eine wichtige Rolle in der Ionenbilanz im Void.

In gewissen Parameterbereichen (einschließlich hoher Dichte der Mikroteilchen und bestimmter Gasdrücke sowie Entladungsleistungen) wird das Void instabil und verändert periodisch seine Größe. Dieses Phänomen heißt "Herzschlag (=Heartbeat) Instabilität". Wir untersuchten es und legten dabei einen besonderen Schwerpunkt auf die optogalvanische Kontrolle der Instabilität mittels eines durchstimmbaren Lasers. Wir fanden heraus, dass kontinuierliche Laserstrahlung die Mikroteilchenwolke stabilisieren kann, während ein modulierter Laser die Variationen des Voids entweder transient oder resonant anregen kann. Die Resonanz wurde beobachtet, wenn die Modulationsfrequenz mit der Frequenz

von kleinen radialen Schwingungen übereinstimmte. Die Schwingungen werden für eine Voraussetzung für die Heartbeat Instabilität gehalten. Auf Grund der experimentellen Ergebnisse und der Theorie der matten und hellen Erscheinungsformen des Voids konnten wir schließen, dass die Kontraktionen des Voids durch einen abrupten Übergang von der matten in die helle Erscheinungsform des Voids ausgelöst werden.

Da es sich bei der Heartbeat Instabilität um einen komplexen Prozess, der viele Zeitskalen umfasst, handelt, kann die Instabilität nicht direkt simuliert werden. Deshalb gibt es auch immer noch kein vollständiges Verständnis dieses Phänomens. Die in dieser Arbeit vorgestellten experimentellen Untersuchungen ermöglichen es allerdings nun, den Ablauf der Instabilität in einzelne Phasen zu unterteilen, die getrennt untersucht werden können.

Abstract

Complex or dusty plasmas are electrically quasineutral media containing ionized gas and micron-sized solid particles. They are widely spread in nature (noctilucent clouds, planet rings, comets etc.) and technological devices (plasma edge in tokamaks, nanoparticle production, plasma etching and deposition). Fluxes of electrons and ions onto the microparticle surface charge it. Interacting with each other, the microparticles can form a strongly coupled subsystem, which is used for particle resolved studies of generic phenomena in classical condensed matter. At the same time, microparticles interact with other plasma components and modify in many cases significantly the background plasma conditions. This cumulative thesis is devoted to the microparticle-plasma interactions in a capacitively-coupled RF discharge in argon.

Using tunable diode laser absorption spectroscopy (TDLAS), we detected small microparticle-induced gas heating and measured the effect of the microparticles on the metastable density. Then we tried to overcome limitations of TDLAS diagnostics by means of planar laser induced fluorescence and obtained qualitative two-dimensional distributions of the metastable density.

Simultaneous observations of the microparticle arrangement and the plasma emission revealed that the void (a microparticle-free area inside the suspension) can exist in two regimes, which we termed "dim" and "bright". The dim void regime corresponds to relatively low discharge power conditions and is characterized by a diffuse emission profile inside and around the void. The bright void regime corresponds to the conditions with higher RF discharge power and is characterized by the bright plasma emission inside the void. The transition between the regimes has a discontinuous character and is manifested by a kink in power dependencies of the void size. A modelling suggested that the void formation mechanism differs qualitatively in these regimes: In the bright void regime, strong time-averaged electric field at the void boundary heats the electrons. In the case of dim void, the electric field is much lower, and the radial diffusion plays a significant role for the ion balance inside the void.

In some conditions (including high density of microparticles and specific gas pressures as well as discharge powers) the void becomes unstable and contracts periodically. This phenomenon is called the heartbeat instability. We investigated this phenomenon with particular attention to its optogalvanic control with a tunable laser. We found out that the continuous laser beam can stabilize the microparticle suspension whereas the modulated laser can induce the void contractions either transiently or resonantly. The resonance was observed when the modulation frequency coincided with the frequency of the small breathing oscillations, which are supposed to be a precursor for the heartbeat instability. Based on the experiments and the theory of dim and bright void regimes, we could conclude that the void contractions are triggered by an abrupt transition of the dim void to the bright regime.

Being a complex multi-timescale process, the heartbeat instability cannot be simulated directly, and its full understanding is still unavailable. However, we decomposed the instability cycle into individual stages, which can be investigated separately.

Chapter 1

Introduction

This work is devoted to microparticle-plasma interactions in RF discharge complex plasmas. In particular, such phenomena as dust-induced heating of the neutral gas, the void formation and the heartbeat instability are considered in this work. The state-of-the-art understanding of the interactions and related experimental results are described in our recent review [3]:

> M. Y. Pustylnik, A. A. Pikalev, A. V. Zobnin, I. L. Semenov, H. M. Thomas, O. F. Petrov "Physical aspects of dust-plasma interactions", *Contributions to Plasma Physics*, vol. 61, p. e202100126, 2021.

In the introduction, we shortly reproduce main concepts from this review which are significant for the presented research.

1.1 Complex plasma

Dusty (or complex) plasmas represent a class of low-temperature and (usually also) low-pressure plasmas containing along with free electrons, ions, neutral molecules and radiation also nanometer- or micrometer-sized solid particles, which we will call "dust particles" or "microparticles". Such plasmas can be found in nature in the form of planetary rings, comet tails or noctilucent clouds, as well as in industrial plasma reactors. Several reviews on complex and dusty plasmas are published [12–19].

Dust particles immersed in plasmas represent a new plasma component with unusual properties: They (i) absorb the fluxes of plasma species on their surfaces, (ii) acquire relatively large negative charges that are non-negligible in the net charge balance of the plasmas and are self-consistently coupled to the local plasma conditions, (iii) exhibit relatively slow dynamics due to the low charge-to-mass ratio and (iv) become sensitive to fluxes and temperature gradients in charged as well as in the neutral components of the plasma. Therefore, dusty plasmas cannot be treated as ensembles of dust particles immersed in dust-free plasmas, and dust-plasma interactions need to be taken into account. Such investigation is necessary for such plasma applications as synthesis of nanoparticles as well as for fundamental research.

The possibilities of using plasmas for production of nanocrystals are being actively investigated [19]. Semiconductor nanocrystals have led to promising advancements in such fields as solar cells, quantum dot light-emitting diodes, bioimaging or nanocomposite materials [20]. Plasma synthesis of dust particles exhibits a number of advantages if

compared to wet chemistry or other gas-phase synthesis approaches. It requires neither solvents nor ligands, allows to work with high melting point materials, prevents the dust particles from coagulation by means of charging, etc. Recently, a great progress has been achieved in this field. Elemental, alloy and doped group IV semiconductor nanocrystals, compound semiconductor nanocrystals, metal dust particles can be presently synthesized using plasmas. Further advances in this field which would result in plasma synthesis of heterostructures or multicomponent materials is hardly possible without deep understanding of dust-plasma interactions.

The other field involving complex plasmas is the basic interdisciplinary research, in which the subsystem of strongly coupled dust particles is used as a model system for the particle-resolved investigations of generic phenomena of classical condensed matter physics [17,18]. These experiments target such fundamental interdisciplinary questions as e.g., phase transitions, electrorheology [21] or turbulence [22]. To be individually resolved, the dust particles must have the size in the micrometer range. For such large particles, the gravitational force becomes very important. Although gravity can be roughly compensated by thermophoresis under ground laboratory conditions [23], the unstressed 3D dust suspensions can only be studied in microgravity. Under microgravity conditions, the dust particles occupy significant fraction of the plasma volume and dust-plasma interactions become therefore very important. The complex plasma laboratories on the International Space Station (ISS) — PKE-Nefedov [24], PK-3 Plus [25] and PK-4 [26] — yielded great scientific success. However, the microparticle suspensions observed in these experiments are in a certain parameter range far from the desired condition of calmness and uniformity [2,27,28]. Understanding of the fundamentals of dust-plasma interactions is the key to the progress in the quality of the microgravity complex plasma experiments as well as to the correct interpretation of their results.

1.2 Basic processes in complex plasma

1.2.1 Microparticle charging

The micrometer-sized particles in low-temperature plasma usually acquire high negative charges ($\sim 10^3 - 10^4 e$) due to the collection of ions and electrons. The particles become charged negatively because the mobility of electrons is much higher than that of positive ions. The stationary value of the dust charge can be calculated from the balance equation

$$\sum_{\alpha} I_\alpha = 0, \tag{1.1}$$

with I_α being the currents of different plasma components at the microparticle surface. Equation (1.1) is typically used to find the microparticle surface potential, φ_p. The microparticle charge, q_p, is then estimated using the simple identity $q_\mathrm{p} = 4\pi\varepsilon_0\varphi_\mathrm{p}a$, with a being the microparticle radius. The microparticle charge depends on the gas type, the ratio of the ion to electron temperatures, T_i/T_e, the ratio of the ion to electron number densities, n_i/n_e, and plasma collisionality.

In collisionless plasmas, the collection of ions and electrons by a single dust particle is well described by the orbital-motion limited (OML) theory [29]. Within this approach, the collection cross-sections for ions and electrons are derived from the analysis of their trajectories in the central field of a charged particle taking into account the conservation of

energy and angular momentum. The ion and electron currents are calculated by averaging the collection cross-sections over an appropriate velocity distribution function. Despite known limitations [30], the OML theory provides a reliable estimate for the particle charge under conditions where the mean free path for ion-neutral collisions, λ_{in}, is much longer than the characteristic screening length (Debye length), λ_{D}, in plasma.

In weakly collisional plasmas where $\lambda_{\mathrm{in}} \sim \lambda_{\mathrm{D}}$, the ion-neutral collisions affect the ion orbital motion and increase the probability of ion absorption by the dust particle. This increases the ion current to the particle and decreases the absolute value of particle charge. The reduction of particle charge due to ion-neutral collisions has been measured experimentally in direct current (DC) discharge plasma [31]. The ion flux in the weakly collisional regime was addressed with analytical models [32–34] as well as self-consistent numerical simulations [35–39].

1.2.2 Forces acting on a microparticle

Under ground laboratory conditions, gravity is the dominant force for the micron-sized particles. The force scales with their radius as a^3:

$$\mathbf{F}_{\mathrm{g}} = m_p \mathbf{g} = \frac{4}{3}\pi a^3 \rho_{MF} \mathbf{g}, \tag{1.2}$$

where m_p is the microparticle mass, $\mathbf{g}$ is the free fall acceleration, $\rho_{MF} \approx 1.5\,\mathrm{g/cm^3}$ is the melamine formaldehyde mass density [23].

If the microparticle is moving relative to the gas medium, it experiences the neutral drag force. This force damps the microparticle motion. Due to it, instabilities in complex plasmas are suppressed at higher gas pressures. The force can be estimated using the kinetic theory of gases. In our experiments, the microparticle size is much smaller than the mean free path for the neutral-neutral collisions in gas (see section 2.6), hence the well-known Epstein formula [40] can be used:

$$\mathbf{F}_{\mathrm{n}} = -\frac{32}{3}\delta a^2 p \frac{\mathbf{u}}{\langle v_{Ta} \rangle}, \tag{1.3}$$

where p is the gas pressure, $\mathbf{u}$ is the microparticle velocity relative to the gas, $\langle v_{Ta} \rangle$ is the averaged atomic thermal speed and δ is a coefficient in the order of one depending on the gas-surface interaction.

The thermophoretic force also plays an important role in the experimental investigations of dusty plasmas. It can be estimated using the following expression [41]:

$$\mathbf{F}_{\mathrm{th}} = -\frac{32}{15}\frac{a^2}{\langle v_{Ta} \rangle}\kappa_{\mathrm{n}} \nabla T_{\mathrm{n}}, \tag{1.4}$$

where κ_{n} is the thermal conductivity of the gas and T_n is the gas temperature.

Obtaining the charge, the microparticle becomes sensitive to the electric field. The electrostatic force is proportional to the microparticle charge, which is roughly proportional to its radius.

The scattering of ions by dust particles is known to affect noticeably the dynamics of dust in gas discharges. The drag force exerted on dust particles by drifting ions (ion drag force, IDF) can be comparable with the electrostatic force caused by the ambipolar

electric field in a plasma. For collisionless plasmas, the IDF is typically calculated using the binary-collision formalism [42–44]. Within this approach, the IDF is given by

$$\mathbf{F}_\mathrm{d} = m_\mathrm{i} \int \mathbf{v} \upsilon f_\mathrm{i}(\mathbf{v}) \sigma(\upsilon) d\mathbf{v}, \tag{1.5}$$

where σ is the momentum transfer cross-section for ion-dust collisions and f_i is the ion velocity distribution function ($\mathbf{v}$ is the ion velocity and $\upsilon = |\mathbf{v}|$). The momentum transfer cross-section for ion scattering on dust particles can be computed numerically [45] or using an analytical approximation [42, 43, 46].

The effect of ion-neutral collisions on the IDF was studied in detail using results of particle-in-cell (PIC) Monte Carlo simulations [47, 48]. It was shown that in the weakly-collisional regime ($\lambda_\mathrm{in} \sim \lambda_\mathrm{D}$), the IDF slightly increases (by a factor of two) as compared to the collisionless limit. In highly collisional plasmas, the IDF is known to decrease below the collisionless limit [47–49].

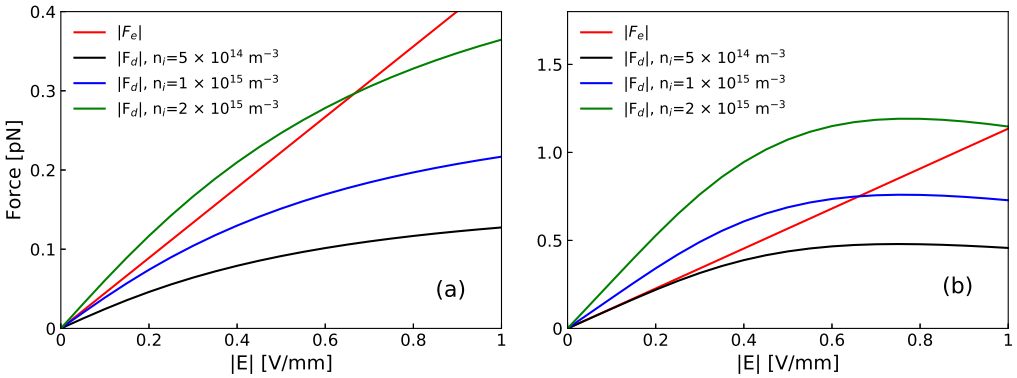

Figure 1.1: The ion drag force, $\mathbf{F}_\mathrm{d}$, and the electric force, $\mathbf{F}_\mathrm{e} = q_\mathrm{p}\mathbf{E}$, for the mobility-limited ion flow. Panels (a) and (b) correspond to the conditions of experimental studies [1] and [2], respectively. The figure is taken from [3].

The typical values of the IDF are presented in Figure 1.1. The estimates are shown for the mobility-limited ion flow under a uniform electric field. The IDF is calculated using the same model as [1].

1.3 Effect of the microparticles on plasma

1.3.1 Experimental observations

First direct experimental evidence of plasma absorption by dust particles dates back to 1970 [50], when it was shown that the duration of the plasma afterglow decreases if plasma contains dust. However, measurements in the steady-state discharges appeared only with the development of the entire field of dusty plasmas.

Already the earliest experiments, in which dust particles were synthesized in the plasma [51, 52], showed the main features of dust-plasma interactions. The growth of dust was accompanied by the reduction of the phase angle between the voltage and current of the capacitively coupled RF (CCRF) discharge. At the same time, the intensity of the plasma emission increased, and even flattening (of usually two-humped) axial

emission profile of a CCRF discharge was observed. Spectroscopic [51] and Langmuir probe [52] measurements revealed the dust-induced increase of electron temperature. The electron and ion densities decreased, whereas the number density of metastable atoms increased [51]. The observed transition was, in its appearance, similar to the $\alpha - \gamma$ transition in CCRF discharges [53] and was therefore termed $\alpha - \gamma'$ transition [54]. These findings were confirmed in further works [55–58]. Later, this regime was termed "volume-dominated" [59, 60] or $\Omega-$mode [61, 62] since secondary electrons are not primary ionization source in this regime. The investigations of the effect of growing dust on the electrical parameters of the CCRF discharge gave rise to the dust detection techniques and even dust metrology methods which rely on the electrical measurements only and do not require any optics [63, 64].

Further progress in the experiments on CCRF discharges was achieved on the suspensions of industrially manufactured microparticles injected into the plasma. Spatiotemporal patterns of the plasma emission obtained using RF period-resolved optical emission spectroscopy (PROES) [61, 62] showed that the emission spots associated with the RF sheath expansion, which in the microparticle-free discharge concentrate in the vicinity of electrodes, penetrated much deeper into the plasma and were even able to reach the opposite sheath in the case of a dusty discharge. Later work [65] confirmed this result and showed how this spatiotemporal pattern evolves with the increase of the amount of microparticles in the plasma. PROES observations were therefore in accord with earlier electrical and time-averaged spectroscopic measurements and confirmed the heating of electrons in dusty discharges as compared to dust-free discharges.

Even small amount of microparticles can produce measurable effect on the plasma. In this case, the dust particles absorb the plasma species and affect the plasma electric field only locally. The resulting effect can be however non-local due to the non-locality of electron kinetics in low-pressure discharges. It was revealed for the first time by PROES measurements in an argon CCRF discharge with a very thin layer of microparticles [66]. The exact pattern of the dust-induced modification of the spatiotemporal emission profile strongly depended on the microparticle size: For smaller microparticles, the emission was increasing at the beginning of the sheath expansion, whereas for bigger particles, it was, on the contrary, decreasing at the beginning of the sheath expansion. Experiments with somewhat larger amount of microparticles [67] confirmed the nonlocal character of the dust-plasma interactions. However, the effect shifted towards the increase of the emission above the microparticle layer for all microparticle sizes. The effect was much stronger for larger microparticles. In most cases, a decrease of plasma emission was observed inside the layer of microparticles. In experiments with hydrogen-silane plasma [62] with the nanoparticles shifted towards one of electrodes by the thermophoresis, the nanoparticles increased the plasma emission, which was especially bright, in contrast with [67], in the area with the nanoparticles.

Measurements using microwave interferometry [68] performed above the microparticle layer showed a modification of the electron density: Larger microparticles were found to cause its increase, and smaller microparticles — its decrease. Also, in accord with the later PROES measurements [67], a decrease of the plasma emission inside the microparticle layer was observed for smaller microparticles. For larger microparticles, the plasma emission was increased in the entire discharge volume.

Early emission spectroscopy measurements [51] as well as later TDLAS measurements [69] demonstrated that the presence of large amount of microparticles in CCRF plasmas

affects not only the electrons, but also the neutral component. The number density of metastable states increases.

TDLAS measurements [70] in a neon CCRF discharge containing a thin (several mm) layer of dust showed the appearance of a dip in the axial distribution of the number density of metastable atoms, which could be compared with the decrease of the plasma emission inside the suspension reported in [67]. The width of the dip corresponded to the thickness of the dust layer. At the same time, the radial distribution of the same metastable atoms measured at the height of the dust layer exhibited a decrease in the central area. Quenching of the metastable atoms on the dust was the only feasible explanation. On the other hand, the absorption measurements on the metastable atoms (performed with a single mirror method) [71] revealed the dust-induced increase of the number densities not only inside the microparticle suspension, but also far above it. It corresponds to the increase of metastable density detected for a discharge with nanoparticles in [51].

The dust-plasma interactions were also investigated in DC discharges. It was shown in a ground-based experiment that the average axial electric field in the positive column containing a dust suspension increases up to 25% compared to that in a dust-free positive column [72]. The spectroscopic investigation of the plasma emission under microgravity conditions [73] indicated the increase of the electron temperature in the dusty DC discharge in an analogy to CCRF discharges. Absorption of electrons in the tube center causes broadening of the radial emission distribution [73–76].

1.3.2 Physical interpretation

Dust-free low-temperature low-pressure plasmas are usually characterized by the non-local ionization balance: The electron-ion pairs are produced in the bulk by electron impact ionization, whereas the recombination occurs on the walls of the plasma reactor or on the electrodes [77, 78]. This leads to the formation of the ambipolar electric field that adjusts the fluxes of electrons and ions in such a way that the quasineutrality can be supported at every point of the plasma.

In presence of dust in the plasma, the ionization balance inside the dust suspension can localize. This was for the first time clearly shown by Sukhinin *et al.* [79], who investigated the radial distributions of plasma parameters in a DC discharge using a hybrid model. Radial distribution of dust was also calculated using the drift-diffusion approximation taking into account the macroscopic electrostatic force as well as the Yukawa interaction between neighbouring dust particles. It turned out that the dust self-consistently arranges in such a way that the radial ambipolar electric field is zero, which is the manifestation of the locality of the ionization balance. This result was confirmed also for the case when IDF was taken into account [80].

On the other hand, when considering the same problem of the radial stability of the dust suspensions in a DC discharge at considerably larger currents compared to previous works [79, 80], Fedoseev *et al.* [81] encountered strong (of the order of several V/cm) electric fields inside the suspensions. In this case, the mechanical balance was realized by the detailed balance between the electrostatic force and IDF at non-zero electric field.

Generalizing the results of the simulations [79–81], we can formulate two principles of the self-organization of the microparticle suspensions immersed in low-temperature plasmas in presence of only two dominating forces — electrostatic force and IDF (see figure 1.1): (i) The ambipolar electric field inside the suspension vanishes. As a result, the electrostatic force and IDF disappear and the ionization balance localizes. (ii) The

ambipolar electric field inside the suspension does not vanish. Detailed local balance of electrostatic forces and IDF has to be satisfied for the dust particles. Ionization balance is non-local (as in a dust-free discharge). The parameter that defines the principle is the ionization rate in the plasma, which determines the ion density: At low ionization rates, the ion fluxes in the plasma are insufficient to compensate the electrostatic force by the IDF, and the suspension self-organizes according to the first principle. Increase of the ionization rate makes the second self-organization principle possible. In this dissertation, we demonstrate that similar regimes exist in the complex plasma of CCRF discharge, and changing the discharge power causes a transition between them (see section 3.3 and paper [1]).

The dust change the electron energy and density in plasmas even in the experiments with small amount of microparticles. The increase of plasma emission and of number densities of metastable atoms above the dust layers levitating in the CCRF discharges suggests that the electrons in that area are excessively heated. The combined three-dimensional PIC and molecular dynamics model of dust-plasma interactions [67] was able to explain the increase of plasma emission above the dust layer. It was, however, only applied to a single large (10 μm diameter) microparticle in a plasma and, therefore, could not explain the entire variety of the observed phenomena. It can be nevertheless supposed that the local absorption of plasma species on dust competes with the heating of the electrons. The same happens when dust occupies significant fraction of the plasma volume [61, 65].

In the CCRF discharge, the RF electric field increased due to the depletion of negative charges inside the dust layer [61,65]. In a dust-free CCRF discharge, the plasma electrons are heated mainly by the sheath electric field [53]. At the same time, the electrons effectively screen this electric field due to their high mobility. Therefore, ionization and glow are concentrated in the narrow layers close to the sheaths. However, in a dusty CCRF discharge, the free electron density considerably decreases. Their negative charge gets immobilized on the surfaces of dust particles. This allows the sheath electric field to penetrate much deeper into the bulk plasma. Similar effect is well-known for electronegative discharges [82, 83].

Although the spatiotemporal redistribution of the ionization rate in a dusty CCRF discharge was obtained in PIC simulations long ago [84], the above-mentioned mechanism was revealed considerably later by Killer *et al.* [61]. In the simulations performed in that work, the static homogeneous distribution of dust in an argon plasma was implemented. A more advanced model that allowed self-consistent fluid treatment of dust component [65] confirmed the above-mentioned mechanism. Spatiotemporal profiles of the plasma emission measured using PROES [61,65] were in agreement with the respective spatiotemporal profiles obtained in the simulations.

The dust-induced electron heating also occurs in DC discharges, as it was demonstrated numerically [75, 85–87] and experimentally [73–75]. The physical mechanism of the excessive electron heating in the dusty DC discharge is connected with the necessity to keep the discharge current constant. The plasma losses on the surfaces of the dust particles effectively result in the increase of the plasma resistance. In order to support the same current as in dust-free plasma, the discharge voltage and consequently the axial electric field in the discharge are increased. This is in accord with the experimentally observed increase of the axial electric field after the injection of dust into a DC discharge striation [72].

1.4 Effect on the gas temperature

The microparticle suspension can also influence the gas temperature and change the temperature gradients. It may play an important role for dust due to thermophoresis: Gradients of the order of 1 K/cm may exert significant forces on the microparticles [26]. Nevertheless, this issue is very rarely accounted for in the literature and is, therefore, quite poorly studied.

There are two dust-related effects that affect the neutral gas temperature: (i) Redistribution of the heat sources associated with the elastic electron-neutral and ion-neutral collisions (existing also in the dust-free plasma) and (ii) heat exchange between the dust particle surface and neutral gas.

The temperature of dust particles in plasmas increases due to their interaction with other plasma components. The equilibrium temperature of dust particles can be estimated by considering the balance between the incoming and outgoing energy fluxes. The incoming energy flux includes the kinetic energy contributions of ions and electrons and the energy released due to their recombination at the dust particle surface. Recombination is known to dominate over the kinetic energy contributions [88]. Thus, the incoming energy flux can be estimated as

$$\mathcal{J}_{\text{in}} = J_{\text{e}}(E_{\text{ion}} + E_{\text{ek}} + E_{\text{ik}} - E_{\text{ak}}), \tag{1.6}$$

where J_{e} is the electron flux to the particle ($J_{\text{e}} = J_{\text{i}}$), E_{ion} is the ionization potential, E_{ek} is the average kinetic energy of colliding electrons and $E_{\text{ik}} - E_{\text{ak}}$ is the average difference between kinetic energies of colliding ions and outcoming atoms after neutralization. In the case of low gas pressure, E_{ik} could be estimated as the microparticle surface potential.

The outcoming energy flux is mainly determined by the thermal conduction between the gas and the dust particles. According to the results of the kinetic theory, this flux can be estimated as [89]

$$\mathcal{J}_{\text{out}} = \alpha\pi a^2 \sqrt{\frac{8}{\pi}} \frac{p\,\langle v_{Ta}\rangle}{2} \frac{\gamma+1}{\gamma-1} \left(\frac{T_p}{T_g} - 1\right), \tag{1.7}$$

where α is the thermal accommodation coefficient, T_p is the dust particle surface temperature, T_g is the gas temperature, $\langle v_{Ta}\rangle$ is the mean thermal speed of gas molecules, p is the gas pressure and γ is the adiabatic coefficient (for noble gases $\gamma = 5/3$). Radiation emission and absorption could also be significant for the thermal balance. These processes are suppressed for dust particles smaller than the radiation wavelength [90]. According to the theoretical estimates and experimental measurements [91], the dust particle temperature can be up to 10 - 20 % higher than the gas temperature for typical experimental conditions.

Perrin *et al.* [92] were the first to discuss the self-consistent neutral gas temperature in a dusty discharge. According to their calculations, appearance of dust in a plasma leads to a significant (~ 10 K) increase of the temperature difference between the central area of the plasma and the walls of the reactor.

According to the simulations by Akdim and Goedheer [93, 94], the influence of the plasma-produced temperature gradients on the dynamics of micrometer-sized dust is in general negligible. In spite of this conclusion, the models in the subsequent papers of that research group [95–98] always contained the heat balance for the neutral gas as well as the thermophoretic force.

In contrast to that, a very simple drift-diffusion discharge model by Vasilyak *et al.* [99] (similarly to Perrin *et al.* [92]) exhibited rather a strong dust effect on the neutral gas temperature field [100]. The radial neutral gas temperature distribution in a DC discharge was considered in this work. The dust configuration was considered static. The cylindrically shaped dust suspension occupied half of the diameter of the discharge tube. The model exhibited a 2 K jump in the axial value of the neutral gas temperature when changing from $n_\mathrm{d} = 0$ to $n_\mathrm{d} = 10^{11}$ m^{-3}.

Experiments [101] showed that the growth of dust particles in an argon-acetylene mixture was accompanied by a drastic (about 50 K) drop of the argon gas temperature. On the other hand, reference [69] reported strong (40–70 K, depending on the discharge power) dust-induced growth of the gas temperature in the discharge center in argon. The achieved temperature gradient should have led to the thermophoretic forces comparable to electrostatic forces.

We can therefore state that the issue of the microparticle-induced modification of the temperature field in discharges is controversial, potentially important for the complex plasmas, and, therefore, requires careful investigation. In the thesis, we propose and discuss a rigorous approach to the tunable diode laser absorption spectroscopy (TDLAS) measurements of gas temperatures in argon discharges. Since small (~ 0.1 K/cm) temperature gradients may play a role in complex plasmas, we took great care of characterizing the uncertainties. After minimizing the uncertainties, we compared the measurements in dust-free and dusty discharges.

1.5 Void

The void is a dust-free area inside a dust suspension immersed in a plasma. It is one of most common disturbances of the homogeneity of CCRF dusty plasmas under microgravity conditions. Void formation and growth also determine the dust particle generation cycle in plasma reactors. It was observed already in early works related to dust growth in reactive [102] or sputtering [103] plasmas as well as in microgravity experiments [104]. In ground experiments, the void can be obtained using the thermophoretic gravity compensation. The radial void may exist also in the DC discharge [81, 105, 106]. In spite of significant effort, the mechanisms that control the void formation and provide its stability are still not completely clear.

The void appears if the CCRF discharge power exceeds a certain threshold, as it was observed in experiments [2, 107, 108] and reproduced in simulations [96, 97, 109, 110]. The dependence of the void onset on the pressure is not clear. According to the simulations of PKE-Nefedov [98, 110], the discharge power of the void onset is lower for lower discharge pressures. On the other hand, in the experiments with IMPF-KT chamber [107], the void closure voltage increased with decreasing the gas pressure from 15 to 5 Pa. No significant dependence on the amount of the microparticles was revealed [96, 97, 109], although increase of the amount of microparticles leads to the decrease of the void size. These experiments as well as the simulations showed that the void size grows with the increase of the discharge power. At certain discharge power, the void size can stabilize [2, 107]. The microparticle density experiences a maximum close to the void boundary [2]. The density peak disappears with the increase of the discharge power.

Thermophoretic force and IDF were considered to be responsible for the void formation. Both forces scale as a^2, which explains the void formation and growth in experi-

ments with growing dust particles [56, 111–113]. First estimations of the IDF by Morfill *et al.* [104] suggested that it is too small to compensate the electrostatic force. However, later it was shown by Khrapak *et al.* that the IDF was about an order of magnitude underestimated [42]. The results of void closure experiments by Lipaev *et al.* [2] were interpreted in terms of a single-particle approach, i.e., the force balance was treated for a single microparticle immersed in the simulated field of dust-free plasma parameters. It demonstrated that the void can form due to the balance of electrostatic force and IDF. This idea, even nowadays, remains the baseline in the understanding of the physics of the void.

A group of experiments was dedicated to the measurement of forces acting on microparticles in the vicinity of the void boundary. In those experiments, the microparticles were injected into the void by a manipulation laser [114] or due to the trampoline effect (see section 1.6) [115]. The observation of the microparticles which fell through the void after the discharge power reduction [116], were injected by a special accelerator [117], or penetrated the void due to an unspecified reason [118] allowed to measure the force in the entire void volume. In each of these experiments, the results were reported for only a single set of conditions.

In early theoretical works, the stable void [119–121] as well as the void formation [122,123] were described based on 1D fluid equations. Neither RF-period-resolved electron dynamics nor external boundary of the suspension was considered. In some models [123], even ionization and recombination on the microparticles were neglected.

To get better insight into microparticle-plasma interaction, the entire discharge was simulated [61, 65, 93, 95–98, 109, 110, 124]. 1D fluid model by Gozadinos *et al.* [124] included both the absorption of plasma electrons and ions on the microparticles and the contribution of the microparticles to plasma quasineutrality. This model reproduced the appearance of the void with reducing the pressure and a peak of microparticle density at the void boundary.

2D fluid model [93,95–97,109] of PKE-Nefedov experiment demonstrated the increase of the electron energy in presence of dust. The simulated void size was compared [96, 97] with the experiment [2]. Although the model qualitatively reproduced the void formation and growth with increasing RF voltage, it predicted higher RF voltage of the void formation compared to that observed in the experiment. The coincidence with the experiment was achieved only by neglecting ion-neutral charge-exchange collisions. The "single-particle" void was shown to be larger and appear for lower powers than the void with the microparticle suspension effect considered. The electron density inside the void was much higher than inside the dust suspension.

In the early works, the dimensions of void and the onset of its formation were compared between the model and experiment. Plasma conditions were normally left without validation. Even the development of PIC codes [98,109] with a more thorough treatment of the electron kinetics did not lead to an immediate breakthrough. The first attempt [61] to compare the outcome of the PIC simulations with the microparticle arrangement and the RF PROES-measured spatiotemporal emission patterns in the experiment was unsuccessful in the sense of void problem since in the simulations, "the sharp dust density gradients at the void edges resulted in unwanted boundary effects". Another PIC model [65] was able to qualitatively reproduce the spatiotemporal emission pattern, but was unable to reproduce the formation of void. Imposing a fixed configuration of microparticles with a void in the simulation led to tremendous forces on the void boundaries and to the drastic distortion of the spatiotemporal emission pattern.

Results of the spectroscopic and Langmuir probe investigations of the plasma conditions inside the void were controversial. The electron energies in the void were qualitatively investigated using line-ratio method [125–127] and were found to be lower inside the void region compared to those inside the dust suspension. On the other hand, measurements with a Langmuir probe by Schulze *et al.* [128] revealed that both the electron temperature and density are higher inside the void than in the suspension. Klindworth *et al.* [129] performed Langmuir probe measurements under microgravity conditions in a parabolic flight. In their experiment, the probe tip could be moved radially as well as axially. The measurements revealed axial and radial increase of electron temperature from the void towards the periphery of the suspension with a small maximum in the void center.

RF PROES measurements by Killer *et al.* [61] showed strong increase of the discharge emission in the center of the discharge, where the void was located. However, the void in that experiment was so large that it was not clear if the emission was coupled with the void. Similar experiments by Pustylnik *et al.* [65] with thermophoretic variation of the void position showed no void-related feature in the spatio-temporal emission patterns. In an experiment with growing (due to sputtering) dust particles [130,131], a bright emission from the void was clearly visible. Similar feature was also present in the distribution of excited argon atoms measured with laser-induced fluorescence. On the other hand, in an experiment with dust particles growing in an argon-acetylene mixture [112], the plasma emission and the metastable density decreased during the void growth, and no local effects could be seen.

In the thesis, we present a next step in the understanding of the void problem. We performed a systematic investigation of capacitively-coupled RF complex plasmas with the void. The investigation included measurements of the microparticle configurations, time-averaged emission profiles and RF-period-resolved spatiotemporal emission profiles. The experiments showed that the void can exist in "dim" and "bright" regimes with qualitatively different appearance. We interpret these data using a simplified and flexible 1D fluid model of a microparticle-containing RF discharge with artificially added radial diffusion. Using the experimental data and the model, we were able to demonstrate the limits of applicability of the old void formation mechanism (due to a strong ion flow from the void to the suspension) and suggest a novel mechanism explaining the void formation outside those limits.

1.6 Heartbeat instability

In the first microgravity experiments with complex plasmas, a spontaneous periodic contraction of the void boundary was reported [132]. Because of its characteristic appearance as well as due to very low repetition frequency (from single contractions to hundreds Hz), this phenomenon was termed "heartbeat" instability. The heartbeat instability was investigated under microgravity conditions on board the ISS [27, 133], in experiments with grown dust particles [134–137] and with the thermophoretic gravity compensation [138]. The heartbeat instability stands in a row of instabilities in complex plasma that includes dust density waves [139], transverse instability [28], filamentary mode and the void rotation [103, 125, 140], plasmoids and carousel instability [141, 142]. Being multi-timescale phenomena, the instabilities in complex plasma pose a hard problem for numerical studies. The physical mechanism of most of these instabilities is still unknown.

The self-excited heartbeat instability exists within a certain range of discharge power and gas pressure and requires relatively high density of the dust suspension [138]. The heartbeat self-excitation region in pressure - discharge power space is expanding with the increase of the amount of microparticles. The heartbeat frequencies depend on gas pressure, discharge power and size of the microparticles [27, 134].

The experiments showed that oscillations of the discharge electrical parameters and the plasma emission are inherent in the heartbeat instability. In the case of the instability with low repetition rate, when the void nearly restores between the contractions, the emission has a well defined spatiotemporal pattern. Just before the void contraction, the plasma glow flashes along the discharge axis, especially in the void. The flash duration is several ms. At the same time, the discharge edge regions become darker. After that, the emission decreases in the contracted void, whereas the emission from the edge regions increases above the level before the flash [134, 135, 137, 138]. In other regimes, it is more difficult to match the flash with the microparticle motion.

The reported data on the variation of the electrical parameters are contradictory. The RF discharge current patterns for the growing dust particles could have qualitatively different shapes for different conditions [134]. In the experiments with grown dust particles [135] and low repetition rate, the flash was accompanied by a peak of the RF discharge current. For the high repetition rate, there was also another sharp peak after the flash. In the microgravity experiments, the oscillations of the RF and DC currents as well as the RF voltage were also observed [27, 133], although low sampling rate could leave certain features unresolved.

Small oscillations of the plasma emission and the RF current can occur between the heartbeat contractions [135–137, 143]. They were termed also "failed contractions". In [138], the heartbeat instability was resonantly stimulated by modulating the ionization rate with a tunable laser. It remained, however, unclear, which oscillatory mode of the void was excited by the tunable laser.

The particle tracking velocimetry was used to determine velocity and acceleration of the microparticles during the instability [27, 133]. The particle tracing during the "trampoline effect" was used to determine the force distribution near the void boundary [115]. This effect is similar to the heartbeat instability. It involves, however, only a few microparticles that are pushed into the void.

The heartbeat instability is a source of waves [27, 133] and turbulence [22, 144]. The generated waves include low frequency waves moving from the center to the edge of the suspension, which were termed "oscillons".

The physical mechanism of the heartbeat instability is still unclear. According to rather a complicated static fluid theory of the void by Vladimirov *et al.* [145], the void can acquire several stable or unstable configurations with different sizes. The heartbeat was supposed to be a transition between those configurations. A lot of simplifications and input parameters, which are difficult to evaluate experimentally, complicate the comparison of this model with the experiments. Another description of the heartbeat instability was based on an equivalent circuit model of the complex plasma [133]. The void oscillations were associated with the variation of the discharge capacitance. The heartbeat instability was also supposed to occur due to a critical transformation on the void boundary [138].

In the dissertation we present a comprehensive investigation of the optogalvanic control of the heartbeat instability. Combining the experimental results with the concept of dim and bright void, we decompose the entire heartbeat process into several stages, which can be investigated separately.

Chapter 2

Experimental setup and diagnostics

2.1 PK-3 Plus chamber

The experiments were conducted in the ground-based PK-3 Plus chamber [25]. The plasma was produced by means of a symmetrical capacitively coupled RF discharge driven in a push-pull mode. Two electrodes were disc-shaped aluminium plates with a diameter of 6 cm. The electrodes were surrounded by a 1.5 cm wide ground shield with three microparticle dispensers on the top side. The sinusoidal signal with the frequency $f_{RF} = 13.56\,\mathrm{MHz}$ was coupled to the electrodes via a matching circuit. We measured forward and reflected RF power after the matching circuit as well as RF voltage and RF current for each electrode. An example of the voltage and current power dependencies for the microparticle-free plasma and the discharge with relatively large amount of the microparticles is shown in figure 2.2. The injection of the microparticles caused the decrease of the discharge current and less pronounced decrease of the voltage for the same discharge power.

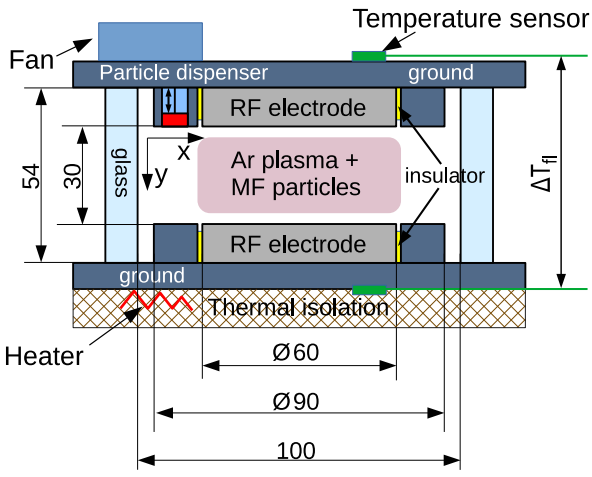

Figure 2.1: Scheme of the PK-3 Plus chamber. The electrodes are driven in a push-pull mode with the frequency of 13.56 MHz. The bottom flange of the chamber can be heated to control the temperature gradient between the electrodes. The dimensions are shown in millimeters.

We used monodisperse melamine formaldehyde spheres as the microparticles. The microparticles were dispersed through a sieve from the dispenser storage volume into the

plasma chamber by electromagnetically driven strokes of a piston. The microparticles were illuminated by a laser sheet with the wavelength of 532 nm.

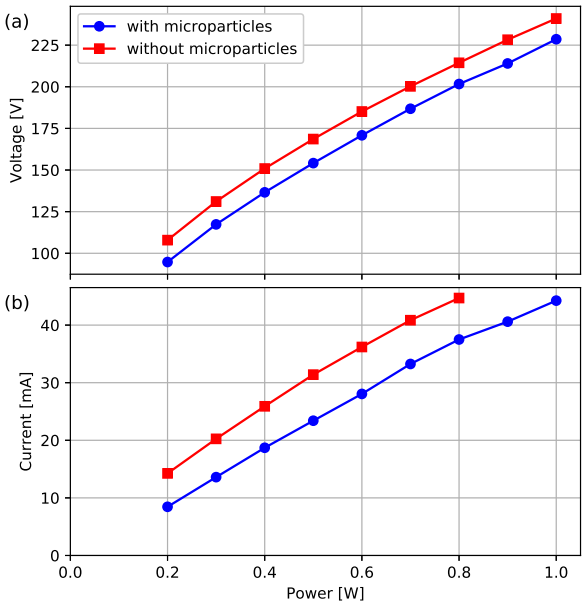

Figure 2.2: Peak-to-peak voltage (between the electrodes) and current dependences on the discharge power. Argon pressure was 35 Pa. The microparticles with the diameter of 1.95 μm were used. The experiments were reproduced with increasing and decreasing the discharge power, the difference between the results was less than the point size.

The chamber was pumped by a turbomolecular pump to 10^{-3} mbar limited by a residual gas flow through the flow controller. Argon was fed into the chamber with 3 sccm gas flow over all experiments. Switching off the gas flow did not cause a change of the microparticle motion.

Under ground laboratory conditions, the microparticles concentrate themselves in the vicinity of the lower electrode. To mimic microgravity conditions and obtain the void, we compensated the gravitational force by means of thermophoresis [23]. The temperature gradient between the electrodes was controlled by heating the bottom flange with an electric heater and cooling the top flange with fans. We measured temperatures on the outer surfaces of the two chamber flanges with Tinytag Explorer data logger. The void appeared in the top part of the suspension if the gravity was undercompensated and in the bottom part if the gravity was overcompensated, similar to [107]. A symmetrical void position was achieved with the temperature difference of 14–15 K for the 1.95 μm diameter microparticles and 15–17 K for the 2.15 μm diameter microparticles. According to [146], the horizontal temperature gradient on the bottom electrode induced by the external heating was 0.5 % of the vertical temperature gradient.

In the experiments with the void, some very small particles were visible near the upper void boundary. They appeared right after an injection and seem to be a contamination of the injected microparticles. These small particles are supposed to be responsible for an asymmetry of vertical velocities in the experiments with the heartbeat instability (see section 3.4).

2.2 Laser absorption spectroscopy

We adopted tunable diode laser absorption spectroscopy (TDLAS) to measure the effect of the microparticles on the gas temperature and metastable density in the discharge. This method is based on the Beer-Lambert law [147]:

$$I(\nu) = I_0(\nu)\exp(-k(\nu)l). \tag{2.1}$$

Here, $I_0(\nu)$ is the incoming laser intensity, $I(\nu)$ — the intensity after the absorption, l is the length of absorbing medium and $k(\nu)$ — the absorption coefficient averaged along l.

The absorption strength characterizes the metastable density:

$$\int_0^\infty k(\nu)\,d\nu = \frac{\Delta\nu_D}{2}\sqrt{\frac{\pi}{\ln 2}}k(\nu_0) = h\nu_0 B_{ik}\langle N_i^*\rangle. \tag{2.2}$$

Here, h is the Plank constant, B_{ik} — the Einstein coefficient, $\langle N_i^*\rangle$ — averaged density of the absorbing atoms. The integral is calculated considering the Doppler shape of the spectral line, which is the shape of the profiles in our experiments (see section 2.6.2).

To measure temperatures and metastable densities at different heights, the beam from the Toptica DL Pro laser was divided into two beams which passed through the RF discharge. The laser scanned the wavelength over a certain range around the 772.38 nm argon spectral line, which was several times wider than the spectral line profile. The scanning frequency was 10 Hz. The laser excited the atoms from the lowest metastable state $1s_5$ to the higher state $2p_7$ (see figure 2.8). To prevent the saturation broadening, the laser beams were attenuated with neutral density filters to the level about 1.5 μW. At these laser light powers, the measured absorption line width exhibited no power dependence, which is in accord with the estimations in section 2.7.2.

In every experiment, we measured two frequency-dependent intensities $I_{abs}(\nu)$ and $I_{laser}(\nu)$ and two constant intensities I_{plasma} and I_{dark}. By $I_{abs}(\nu)$, we mean the intensity of the laser light passed through the plasma. This intensity contains the absorption profile. By $I_{laser}(\nu)$, we mean the laser intensity passed through the discharge chamber without plasma. I_{plasma} is the plasma emission seen by the photodiode and I_{dark} is its dark current. Since $I(\nu) = I_{abs}(\nu) - I_{plasma}$ and $I_0(\nu) = I_{laser}(\nu) - I_{dark}$, from equation (2.1), we obtain [148, 149]:

$$k(\nu)l = \ln\left(\frac{I_{laser}(\nu) - I_{dark}}{I_{abs}(\nu) - I_{plasma}}\right). \tag{2.3}$$

For our estimations, we take the absorption length $l = 6$ cm, equal to the diameter of the electrodes.

The $I_{laser}(\nu)$ curves had complicated shapes, most likely, due to interference on the chamber walls. The chamber wall width is $h_w = 8$ mm and its refractive index $n_w = 1.458$. The wall can be considered as a Fabry-Perot interferometer with free spectral range $\Delta\nu_w = \frac{c}{2h_w n_w} \approx 13$ GHz, which is comparable to the laser scanning range of 4 GHz. To reduce this effect, the incidence angle of the laser beam was slightly detuned from the normal to the wall.

2.3 Laser-induced fluorescence (LIF)

The laser-absorption spectroscopy provides the line-averaged metastable temperatures and densities at only two heights. For deeper insight, space resolved measurement techniques are required. We performed these measurements using laser-induced fluorescence. The method uses illumination of the plasma with a laser whose wavelength is tuned in resonance with an absorption line. A metastable atom is excited by the laser to the state with higher energy, which can spontaneously relax in several transitions (see figure 2.8). The larger the density of atoms in the lower excited state, the stronger is the fluorescence. The LIF diagnostic was applied to complex plasmas to measure resonant and metastable atoms populations [76, 112, 130, 131, 150, 151], ion [152, 153] and neutral [151] flow. Some attempts to determine the neutral gas temperature using LIF were published without any discussions about their accuracy [130, 152] or were contradictory [151].

In our experiments, the fluorescence was stimulated by the same laser that we used in the absorption experiments. The laser tuned in resonance with the 772.38 nm spectral line caused the fluorescence in 810.4 nm spectral line (see figure 2.8). The fluorescence captured by video cameras through narrow-band spectral filters with the central wavelength of 810 nm. The filter transmits also the 811.5 nm spectral line compromising the sensitivity and accuracy of the measurements.

2.3.1 Gas temperature measurements with LIF

The experiments with LIF measurements of the temperature were conducted with the same configuration of the laser beams as in the TDLAS experiments, but, instead of measuring the transmitted laser power, we observed the LIF signal with Photron FASTCAM-1024PCI high-speed camera, whose view direction was orthogonal to the laser beams. The framerate of the camera was 125 fps, and it took 2.5 s for the laser to scan the spectral range once. During the video capture, the oscilloscope registered the intensity of the laser light passing the Fabry-Perot interferometer and a trigger signal from the laser control block, similar to the TDLAS experiments. Start of the video capturing triggered the oscilloscope data acquisition.

2.3.2 Planar LIF

The laser induced fluorescence can give qualitative information about the distribution of the metastable atoms. To obtain the 2D distribution we shaped the beam of the tunable laser into a sheet. The microparticles were illuminated by another laser sheet with the wavelength of 532 nm.

Three Ximea MQ042RG-CM video cameras with interference bandpass filters captured the microparticle motion and the plasma emission in the same discharge area (see figure 2.3). The filters had the central wavelengths of 532, 750, and 810 nm, respectively, and the width of transmission band of the filters was about 10 nm. Hence, one plasma glow observation camera captured the plasma radiation in 750.4 and 751.5 nm spectral lines. Another camera captured the light in 810.4 and 811.5 nm spectral lines. The spatial resolution of the cameras was about 37 μm/pixel. All three cameras were focused on the central cross-section of the discharge chamber as it is described in section 2.4.

We tested two schemes of the laser sheet formation for the tunable laser. First, we tried a system of two cylindrical lenses. After the first lens ($F = 7.7\,mm$) the laser beam

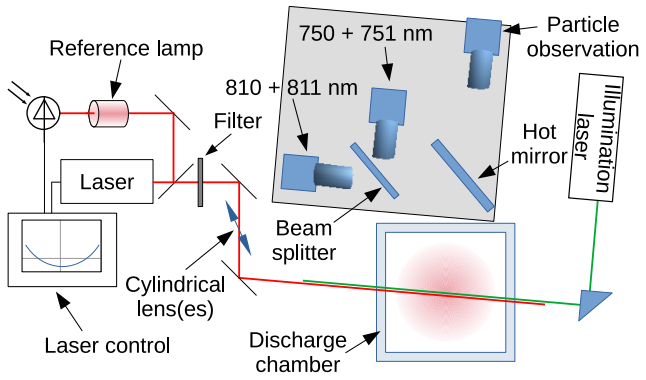

Figure 2.3: Scheme of the planar LIF diagnostic. Both laser beams are transformed to sheets. The laser beams and the cameras are under an angle to the chamber to reduce fluorescence in the chamber walls. The cameras observe the microparticle motion and plasma emission. The reference Ar lamp is used to control the wavelength of the tunable laser.

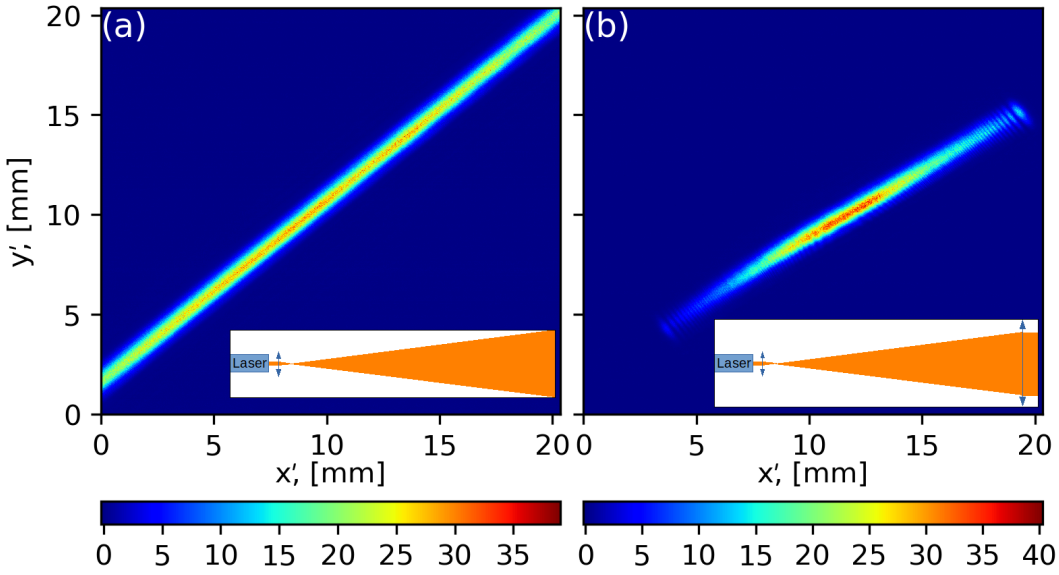

Figure 2.4: Profiles of the laser sheet with one (a) and two (b) lenses. The profiles were captured with Beamage-4M-FOCUS laser beam profiler. The profiler was rotated to have the sheet along the sensor diagonal. Intensities are in arbitrary units. The optical schemes are shown in the inserts.

expanded vertically to the size about 2 cm, and the second lens (F = 140 mm) made it keep this size further. The experiments showed that the laser sheet intensity profile in this case is strongly inhomogeneous (see figure 2.4(b)). We could improve the beam homogeneity by removing the second lens (see figure 2.4(a)). We preferred the single-lens scheme, although it produced small divergence of the laser sheet.

Nevertheless, the laser sheet was not homogeneous, which introduced inaccuracy to the measured distribution of metastable atoms. The influence of the inhomogeneity can be reduced by increasing the laser power to work in the saturated regime. However, the high-power laser beam disturbs the plasma conditions, which could be even significant for the microparticle configuration (see sections 2.7 and 3.4.4).

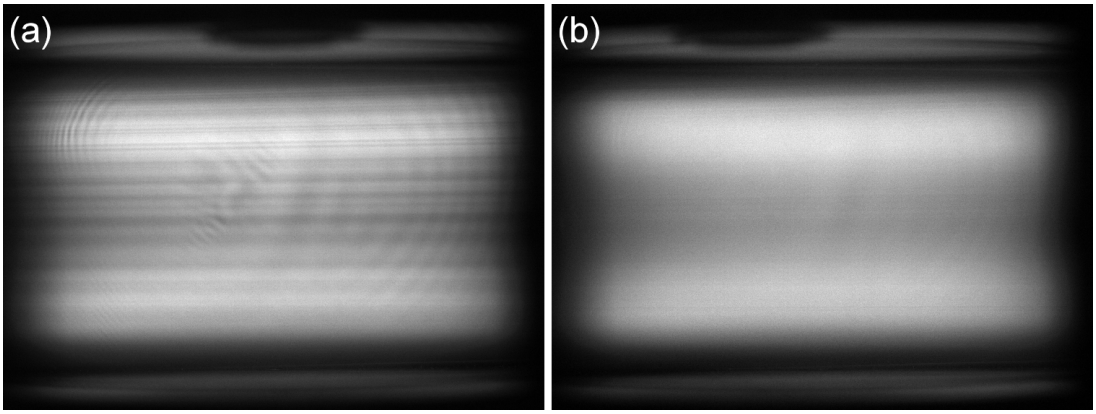

Figure 2.5: LIF obtained with (a) normal incidence of the laser sheet and (b) with the rotation. Discharge power was 200 mW, the gas pressure was 37 Pa, no microparticles were injected. The laser intensity was reduced by a filter with the transmission of 0.12.

Another source of the sheet inhomogeneity is the interference in the glass chamber wall. To reduce this effect, we detuned the laser sheet by a small angle ($\sim 5°$) from the normal incidence. The cameras were rotated respectively to look orthogonally to the laser sheet. The result is shown in figure 2.5. The circular interference pattern visible in the frames is related to the filter on the camera and disappeared when we used FBH810-10 filter instead of FB810-10 (both from Thorlabs), which had higher transmission within the band and higher optical density out of it.

Although the laser sheet had a maximum of intensity in the center (see figure 2.4(a)), the vertical distribution of LIF signal exhibited a minimum in the discharge center. It suggests, that the metastable atoms were mostly born near the sheaths, and the volume sinks were significant. The sinks include not only internal plasma processes listed in section 2.6.1, but also depopulation caused by the laser (see section 2.7). This effect explains the dependency of the LIF vertical distribution on the laser intensity shown in figure 2.6(a). The higher was the laser intensity, the more pronounced was the minimum of the LIF signal in the middle between the electrodes. Nonlinearity of the LIF dependence on the laser power is clear in figure 2.6(b), where the LIF distributions are divided by the transmission of the filters, which determined the laser power. If the LIF signal had been proportional to the laser power, the curves would coincide with each other. As expected, the nonlinearity is stronger for higher laser powers.

2.4 Optical emission spectroscopy

We investigated the emission of the complex plasma using the system of three cameras described in section 2.3.2. In the experiments other than the planar LIF measurements, the view direction of the cameras was orthogonal to the plasma chamber window. The video capture of all three cameras was started by the software approximately at the same time. The difference between the timestamps of the frames with the same number was less than the duration of a single frame.

The images from the cameras were shifted and slightly rotated with respect to each other. To superimpose the images, we had to find the correspondence between their pixels. To do that, we took images of a white point-like light source (output of an optic fiber)

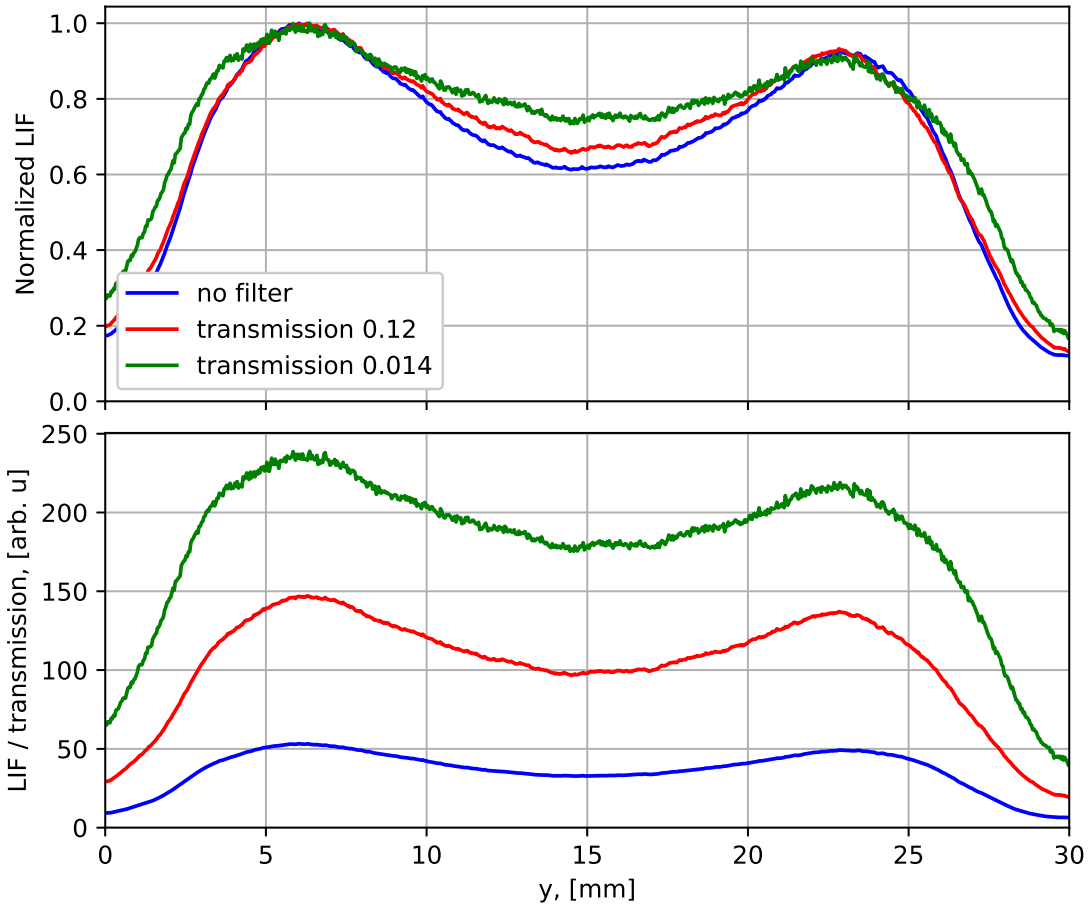

Figure 2.6: LIF vertical distributions obtained with different laser sheet powers. The laser beam was attenuated by neutral-density filters with different transmission. The distributions are calculated by averaging the intensities horizontally in an area with the width of 3 cm in the center of the discharge image. The distributions are (a) normalized to their maximal values, (b) divided by the transmission of the filters.

at several positions in the object plane of the cameras. Using such a light source allowed us to focus all three cameras on the same plane and define a linear transformation of the coordinates between the images of different cameras. At the same time, the camera with the 532 nm filter was focused on the microparticles illuminated in the central cross-section of the chamber.

Dynamic processes captured with this system are presented as spatiotemporal distributions. The x and y distributions of emission intensity were obtained by stacking the profiles of the averaged emission intensities across the respective narrow stripes. The stripes were chosen at the position of the void and had the width of 2.4 mm. The x axis was directed along the beam of the microparticle illumination laser, and the y axis was directed from the top to the bottom (see figure 2.1). In the same way we obtained the spatiotemporal distributions for the velocities of microparticles, which were calculated using OpenPIV software [154, 155]. Preparation of the spatiotemporal distributions is described in more details in [10].

2.5 RF-period-resolved optical emission spectroscopy (PROES)

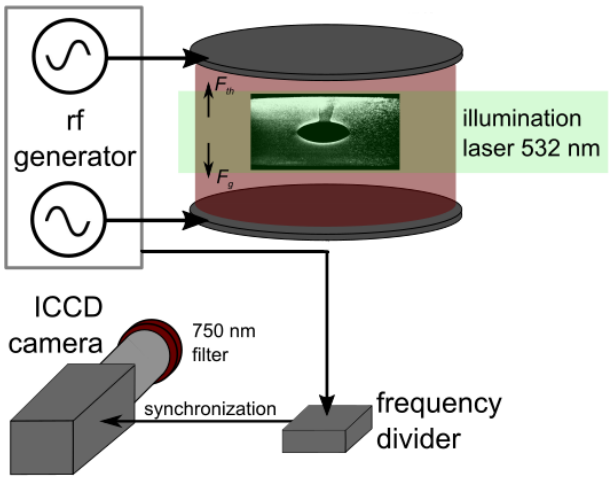

Figure 2.7: Scheme of the PROES diagnostic. The camera is synchronized with the RF generator and observes the discharge via a narrow-band spectral filter.

We also performed RF-period(phase)-resolved optical emission spectroscopy (PROES) experiments, described in details in [1]. The same setup was also employed in [65]. RF-period-resolved evolution of the plasma emission was captured by an ICCD camera (see figure 2.7) which observed the discharge chamber from the side opposite to the three cameras system described in section 2.3.2. The camera was equipped with a 750 nm central wavelength and 10 nm bandwidth filter. The 750.4 and 751.5 nm argon lines transmitted by it have the lifetimes of 22.5 ns and 24.9 ns, respectively [4]. The camera was synchronized with the RF signal through the frequency divider, which sent a synchronization pulse after every 512 RF cycles. The gate width of the ICCD camera was set to 10 ns. The signal was accumulated over the total exposure time of 1 s. The ICCD gate was moved over almost three RF periods with a step of 2 ns. The spatial resolution of the ICCD camera was about 92 μm/pixel. The camera was focused on the central cross-section of the discharge chamber.

2.6 Plasma conditions

In this section, we estimate plasma parameters for typical conditions in our experiments. Most of the experiments were conducted with argon pressure $p = 36$ Pa. Argon atomic mass $M = 40$ a.m.u.. The gas and ion temperatures are supposed to be equal and close to the room temperature: $T_i = T_g = 300$ K (see measurement results for T_g in section 3.1.1). This results in the atomic concentration $N_a = \frac{p}{kT_g} \approx 8.7 \cdot 10^{21}$ m^{-3}, averaged thermal speed $\langle v_{Ta} \rangle = \sqrt{\frac{8kT_g}{\pi M}} \approx 400$ m/s, mean free path $\lambda_a = \frac{1}{\sqrt{2} N_a \sigma_k} \approx 0.2$ mm (here $\sigma_k = 4.02 \cdot 10^{-19}$ m^2 — argon kinetic cross-section [77]) and mean frequency of the atomic collisions $\nu_{ac} = \langle v_{Ta} \rangle / \lambda_a \approx 2 \cdot 10^6$ s^{-1}.

Collisions of a microparticle with atoms cause damping of the microparticle motion. Since $\lambda_a \gg a$, the damping rate for our conditions can be estimated using the Epstein equation (1.3):

$$\gamma_{epst} = \frac{F_n}{m_p u} = \frac{8p\delta}{\pi a \rho_{MF} \langle v_{Ta} \rangle} \approx 200\,\mathrm{s}^{-1}. \tag{2.4}$$

The coefficient $\delta = 1.32 \pm 0.08$ is obtained by averaging results from [156]. It means that any microparticle motion without an energy supply is damped on the timescale of 5 ms.

In [65], the discharge was simulated for the conditions similar to our experiments ($p =$ 27 Pa, 54 V RF amplitude and the microparticle diameter of 1.95 μm) using 1D hybrid model. According to the simulation, the electron and ion densities $n_e = n_i \sim 10^{15}$ m^{-3} in the bulk without the microparticles. The electrons were mostly heated near the expanding sheath. The electron temperature T_e was about 3 eV, which gives average electron speed $\langle v_e \rangle \approx 1{\cdot}10^6$ m/s. The injection of the microparticles caused the electron depletion making n_e significantly less than n_i, and the electron heating became more uniform increasing the electron energy.

Based on these data, we estimate the Debye radius $\lambda_D \approx \lambda_{Di} = \sqrt{\frac{\varepsilon_0 k T_i}{e^2 n_i}} \sim 10\,\mu$m and the plasma frequency $\omega_e = \sqrt{\frac{n_e e^2}{m_e \varepsilon_0}} \sim 1\,$GHz. According to [77], average frequency of electron collisions with atoms $\nu_{ec} \sim 10^9\,\mathrm{s}^{-1}$. So, $\nu_{ec} \sim \omega_e \gg f_{RF}$.

2.6.1 Metastable atoms

Argon has two metastable levels: $1s_5$ and $1s_3$ in the Paschen notation (see figure 2.8). Due to very long lifetime, atoms in these states have relatively high concentrations in the discharge.

Table 2.1: Volume sinks of the metastable atoms. Units for the rate coefficients are cm^3/s except for k_{3q} which is in cm^6/s. $N^* \sim 5 \cdot 10^{10}\,\mathrm{cm}^{-3}$ is the metastable density (see section 3.2.1). The coefficients are taken from [11]

Process	Rate coefficient	Rate, s^{-1}
Quenching to resonant: $Ar^* + e \rightarrow Ar^r + e$	$k_r = 2 \cdot 10^{-7}$	$\nu_r = k_r n_e \sim 10^2$
Step-wise ionization: $Ar^* + e \rightarrow Ar^+ + 2e$	$k_{si} < 10^{-7}$	
Superelastic collisions: $Ar^* + e \rightarrow Ar + e$	$k_{sc} < 2 \cdot 10^{-9}$	
Metastable pooling: $Ar^* + Ar^* \rightarrow Ar^+ + Ar + e$	$k_{mp} = 6 \cdot 10^{-10}$	$\nu_{mp} = k_{mp} N^* \sim 10$
Two body quenching: $Ar^* + Ar \rightarrow 2Ar$	$k_{2q} = 3 \cdot 10^{-15}$	$\nu_{2q} = k_{2q} N_a \approx 30$
Three body quenching: $Ar^* + 2Ar \rightarrow Ar_2 + Ar$	$k_{3q} = 1 \cdot 10^{-31}$	$\nu_{3q} = k_{3q} N_a^2 \approx 8$

Metastable atoms can be quenched on the chamber surfaces. According to [157], the diffusion coefficients of the argon metastables are $D_{1s5} p \approx D_{1s3} p \approx 60\,\mathrm{cm}^2\mathrm{s}^{-1}$torr. For our conditions it gives $D^* \approx 200\,\mathrm{cm}^2\mathrm{s}^{-1}$. The diffusion rate can be estimated as $\nu_{D^*} = D^*/\Lambda^2 \approx 200\,\mathrm{s}^{-1}$, where the diffusion length $\Lambda \approx 1\,$cm is determined by the chamber size. To determine Λ more accurate, we would need to consider the distribution of metastable atoms sources.

Main volume sinks for the metastable atoms are summarized in table 2.1. Together their rates are comparable with the quenching rate on the electrodes in our conditions. The quenching rate due to collisions with electrons is dependent on the discharge power.

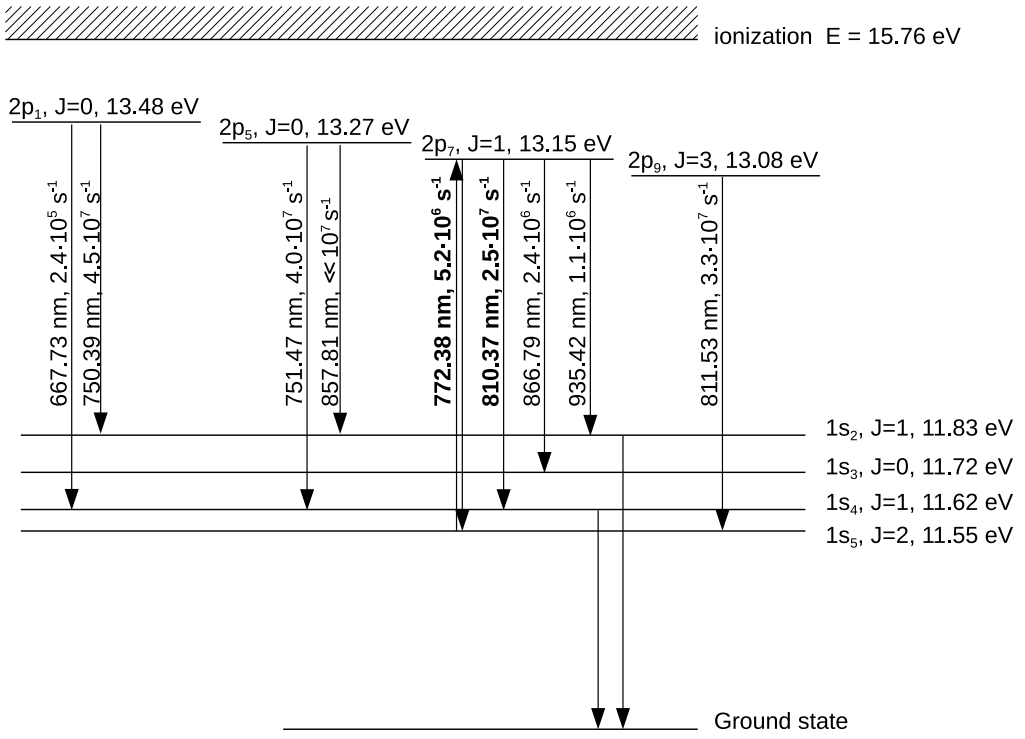

Figure 2.8: Argon spectral lines and energy levels related to this thesis. The transition pumped by the laser and the transition of observed fluorescence are marked bold. The excitation levels are designated using the Paschen notation with denoted total angular momentum J and energy. For the transitions, the wavelengths and the transition probabilities are shown. The data are taken from [4–8].

Taking into account that $n_e \approx 10^{15}$ was obtained in [65] for low discharge power and the gas pressure lower than in most of our experiments, we can consider $\nu_r = 200\,\mathrm{s}^{-1}$ as lower estimate. More than it, in real experiments, the gas contains impurities, which could increase the quenching rate. Summarizing the volume sinks with the quenching on the walls, we can estimate the metastable quenching rate in the microparticle-free discharge as $\nu^*_{free} \sim 10^3\,\mathrm{s}^{-1}$.

The microparticles in complex plasmas represent an additional sink for the metastables. The quenching rate of the metastable atoms on the microparticles can be found as $k_d = \pi r_d^2 \langle v_{Ta} \rangle \approx 1.3 \cdot 10^{-3}\,\mathrm{cm}^3/\mathrm{s}$. In our experiments, the microparticle concentration $N_d \sim 10^5\,\mathrm{cm}^{-3}$ resulting in the metastable quenching rate on the microparticles $\nu_d \sim 10^2\,\mathrm{s}^{-1}$, which is comparable with other sinks.

2.6.2 Spectral line profile

The spectral line broadening is essential for the laser spectroscopy. In the experiments, the laser pumped the transition with the wavelength of $\lambda = 772.38\,\mathrm{nm}$, $\nu = 3.88 \cdot 10^{14}\,\mathrm{Hz}$. Since the lower level of this transition is metastable, the natural broadening is determined by the lifetime of the upper level. Taking into account only spontaneous radiation decay, it gives $\Delta\nu_{nat} \approx 5.4\,\mathrm{MHz}$.

Stark broadening due to collisions with the electrons could be estimated as [147, 158]:

$$\Delta\nu_{st} \approx 1.82 C_4^{2/3} \langle v_e \rangle^{1/3} n_e \tag{2.5}$$

Coupling constants $C_4 \sim 10^{-15}$–$10^{-12}\,\mathrm{cm}^4/\mathrm{s}$. So, the Stark broadening $\Delta\nu_{st} < 10^4\,\mathrm{Hz} \ll \Delta\nu_{nat}$

The metastable atoms collide with other atoms. It does not only disturb the phase during the radiation processes, but also changes the atom velocity along the laser beam. The collision frequency can be estimated from the diffusion coefficient using the kinetic theory of gases:

$$\nu_{col}^* = \frac{\langle v_{Ta} \rangle^2}{3D^*} \approx 2.7 \cdot 10^6\, s^{-1}, \tag{2.6}$$

which is similar to the collision frequency for the atoms in ground state ν_{ac}. Supposing that the atom in the upper state has comparable cross-section of elastic collisions with ground state atoms, we will take homogeneous line width $\Delta\nu_{hom} = 10\,\mathrm{MHz}$ for further estimations. The homogeneous line profile has Lorentzian shape [147]:

$$\varphi_L(\nu) = \frac{2}{\pi\Delta\nu_{hom}} \frac{(\Delta\nu_{hom}/2)^2}{(\nu - \nu_0)^2 + (\Delta\nu_{hom}/2)^2} \tag{2.7}$$

The spectral line profile in our conditions is mainly determined by Doppler broadening:

$$\varphi_D(\nu) = \frac{c}{\nu_0}\sqrt{\frac{M}{2\pi k T_a}} \exp\left(-\frac{Mc^2}{2kT}\frac{(\nu - \nu_0)^2}{\nu_0^2}\right). \tag{2.8}$$

Here, c is the speed of light, and ν_0 is the spectral line center. Doppler spectral line width is

$$\Delta\nu_D = \frac{2\nu_0}{c}\sqrt{\frac{(2\ln 2)kT_a}{M}}. \tag{2.9}$$

For our spectral line, it gives $\Delta\lambda_D \approx 1.5\,\mathrm{pm}$, $\Delta\nu_D \approx 760\,\mathrm{MHz}$.

2.7 Laser-plasma interaction

An atom in the state 1 can resonantly absorb a photon with the frequency ν and be excited to the upper state 2 with rate [147]

$$r_{abs}(\nu_0 - \nu) = B_{12}\rho_\nu \varphi(\nu_0 - \nu). \tag{2.10}$$

Here, ρ_ν is the light power density, B_{12} is the Einstein coefficient for absorption, which can be determined from the spontaneous emission coefficient A_{21} as

$$B_{12} = \frac{g_2}{g_1}\frac{c^3}{8\pi h\nu^3} A_{21}. \tag{2.11}$$

Here, g_1 and g_2 are the statistical weights of the lower and upper levels, respectively. For the 772.38 nm argon spectral line, $g_1 = 5$, $g_2 = 3$ and $A_{21} = 5.2 \cdot 10^6\,\mathrm{s}^{-1}$. Therefore, $B_{12} \approx 8.6 \cdot 10^{19}\,\mathrm{m}^3/(\mathrm{J{\cdot}s})$.

The spectral line profile $\varphi(\nu_0 - \nu)$ is normalized in such a way that $\int_{-\infty}^{+\infty} \varphi(\nu) d\nu = 1$, and ν_0 is the spectral line center.

2.7.1 Saturation broadening

The absorption saturation due to high laser power is determined for a homogeneous line profile by the saturation parameter [159]:

$$\begin{aligned} \Delta\nu_{sat} &= \Delta\nu_{hom}\sqrt{1+S_0}, \\ S_0 &= \frac{2}{\pi\Delta\nu_{hom}}\frac{B_{12}\rho_\nu}{R}, \\ R &= \frac{R_1 R_2}{R_1+R_2}. \end{aligned} \tag{2.12}$$

Here, the homogeneous line width $\Delta\nu_{hom} \approx 10\,\mathrm{MHz}$ (see subsection 2.6.2), R_1 and R_2 are the relaxation rates determined by the processes which depopulate these levels.

Here, we suppose that the density of metastable atoms with the velocities outside the laser-induced hole in the velocity distribution (Bennett hole) is not disturbed by the laser. We designate the relaxation rate of the Bennett hole as R_{hole}. The relaxation rate R_1 for the metastable level is determined by diffusion through the beam volume and inelastic collisions. Taking the beam radius $r_b = 1\,\mathrm{mm}$, we get $R_{1D} = D^*/r_b^2 = 2\cdot 10^4\,\mathrm{s}^{-1}$, which is much larger than the the relaxation rate due to inelastic collisions ($\sim 10^2\,\mathrm{s}^{-1}$, see table 2.1). Taking into account broad velocity distribution, the populations inside the Bennett hole relaxes also with elastic collisions of the atoms (see section 2.6.2), which gives $R_1 = \nu^*_{col} \approx 2.7\cdot 10^6\,\mathrm{s}^{-1}$. The relaxation of the upper level is determined mostly by the spontaneous emission, $R_2 = 3.4\cdot 10^7\,\mathrm{s}^{-1}$. Since $R_1 \ll R_2$, we obtain $R_{hole} \approx 2.5\cdot 10^6\,\mathrm{s}^{-1} \approx R_1$.

The energy density in the laser beam is determined by the laser power P_{las}:

$$\rho_\nu = \frac{P_{las}}{\pi r_b^2 c}. \tag{2.13}$$

For the highest laser beam power of 50 mW, which was used in the experiments with the laser control of the heartbeat instability, $\rho_\nu = 5\cdot 10^{-5}\,\mathrm{J/m^3}$ and $S_0 \approx 1.1\cdot 10^2$ In the experiments with laser absorption spectroscopy, the beam power was reduced down to $1.5\,\mu\mathrm{W}$ resulting $\rho_\nu = 1.6\cdot 10^{-9}\,\mathrm{J/m^3}$ and $S_0 \approx 3.5\cdot 10^{-3}$.

2.7.2 Laser power and velocity-integrated metastable density.

The laser can disturb not only the shape of the velocity distribution function, but also the total density of metastable states. We will designate its relaxation rate as R_{vi}. Elastic collisions of the metastables do not lead to relaxation of the velocity-integrated population. Therefore, the relaxation rate is mainly determined by the diffusion of the metastable through the laser beam: $R_{vi} \sim 2\cdot 10^4\,\mathrm{s}^{-1}$, which is two orders of magnitude lower than R_{hole}. The wavelength scanning speed $\frac{d\nu}{dt} \approx 80\,\mathrm{GHz/s}$ is relatively low: $\frac{1}{\Delta\nu_{hom}}\frac{d\nu}{dt} \approx 8\cdot 10^3\,\mathrm{s}^{-1} \ll R_{hole}$ and $\frac{1}{\Delta\nu_D}\frac{d\nu}{dt} \approx 10^2\,\mathrm{s}^{-1} \ll R_{vi}$. Therefore, the wavelength may be assumed constant when estimating the effect of the laser. Since the laser line width is significantly smaller than the homogeneous profile width, we consider the laser as monochromatic.

For a constant laser frequency ν_{las}, we calculate the absorption coefficient, considering the unperturbed total density of metastable states. Then, we use it to modify the velocity-integrated metastable density and refine the absorption coefficient. After several iterations, this procedure converges to a solution.

Consider a group of atoms with such velocity along the laser beam that the centre of their homogeneous profile is ν'. Their absorption rate is

$$\begin{aligned} R'_{abs}(\nu' - \nu_{las}) &= \frac{(h\nu_{las}/c)\, B_{12}\varphi_L(\nu' - \nu_{las})}{1 + S_{hole}(\nu' - \nu_{las})} F_{las}, \\ S_{hole} &= \frac{B_{12}\rho_\nu}{R_{hole}}\varphi_L(\nu' - \nu_{las}). \end{aligned} \tag{2.14}$$

Here, S_{hole} is the saturation parameter for the Bennett hole. $F_{las} = \frac{c\rho}{h\nu_{las}}$ is the photon flow density in the laser beam. The total absorption rate can be estimated by the convolution of (2.14) with the Doppler profile (2.8) scaled to take into account the change of the velocity-integrated metastable density:

$$R_{abs}(\nu_{las}) = \int_{-\infty}^{+\infty} R'_{abs}(\nu' - \nu_{las}) \frac{\varphi_D(\nu_0 - \nu')}{1 + S_{vi}(\nu_{las} - \nu_0)}\, d\nu'. \tag{2.15}$$

Here, ν_0 is the centre of the spectral line, $S_{vi}(\nu_{las} - \nu_0) = R_{abs}(\nu_{las})/R_{vi}$ is the saturation parameter for the velocity-integrated density (it is similar to the parameter for homogeneous line profile in [159], since the equations for the populations are equivalent). We solve this integral equation iteratively taking $S_{vi} = 0$ as initial approximation. It determines the velocity-integrated metastables density

$$N^* = \frac{N_0^*}{1 + S_{vi}} \tag{2.16}$$

there N_0^* is the velocity-integrated metastables density without the laser. The absorption coefficient is

$$k(\nu_{las}) = \frac{R_{abs}(\nu_{las})}{F_{las}} N_0^*. \tag{2.17}$$

We calculated the dependencies of the absorption coefficient and the metastable depletion on the laser power with the laser tuned to the spectral line centre. The dependencies are calculated for $\Delta\nu_{hom} = 10\,\mathrm{MHz}$ (see section 2.6.2) as well as for $\Delta\nu_{hom} = 5\,\mathrm{MHz}$ and $\Delta\nu_{hom} = 20\,\mathrm{MHz}$ (see figure 2.9). Inaccuracy in the estimation of $\Delta\nu_{hom}$ does not cause a qualitative difference in the laser effect. We calculated the effect of the saturation on the spectral line profile measured with the laser power of $1.5\,\mu\mathrm{W}$ used in TDLAS experiments and the maximal laser power of 50 mW used in the experiments with the heartbeat stimulation. The results are presented in figure 2.10. The influence of the laser beam used in the TDLAS experiments is negligible, whereas the laser beam with maximal power causes strong depletion of the metastable density. The profile for the high laser power cannot be fitted by a Voigt profile (convolution of the Doppler and the Lorentz profiles) with the real temperature of the Doppler component.

These estimations are performed under the assumption that the rates of plasma processes are not modified by the laser (no optogalvanic effect). Moreover, the laser beam inhomogeneity and the spatial distribution of the metastable atoms also play a role.

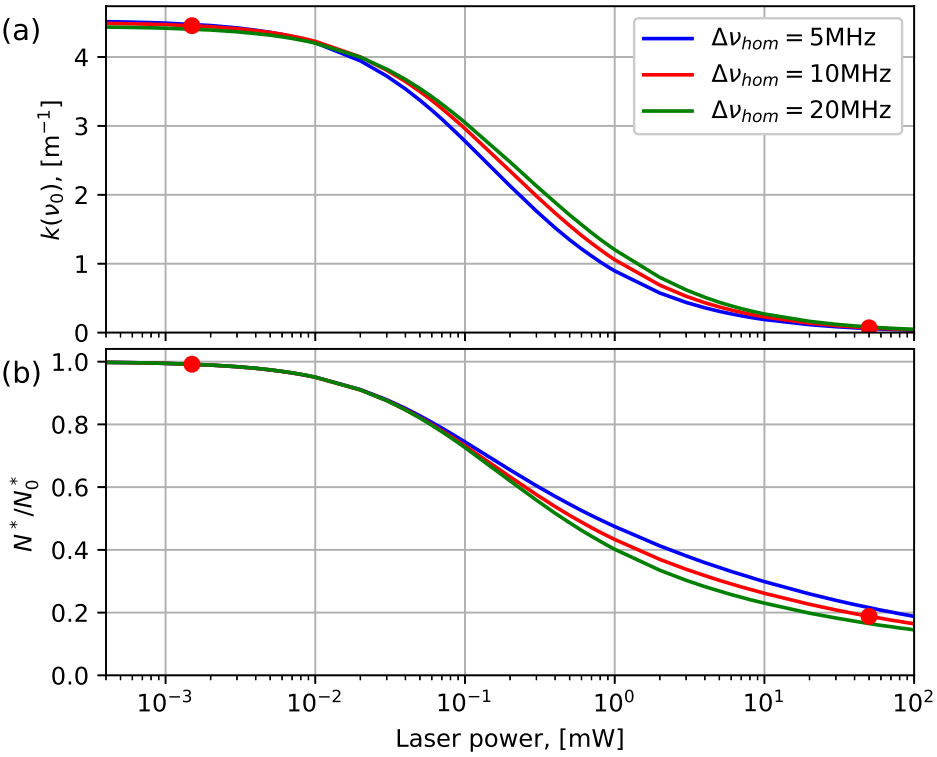

Figure 2.9: (a) The absorption coefficient (supposing $N_0^* = 5 \cdot 10^{16}\,\mathrm{m}^{-3}$) and (b) the ratio of the remaining to non-disturbed metastable density depending on the laser power, when the laser wavelength is adjusted to the spectral line centre. The red dots depict conditions for the full beam power (50 mW) and the beam power used in the TDLAS experiments (1.5 μW).

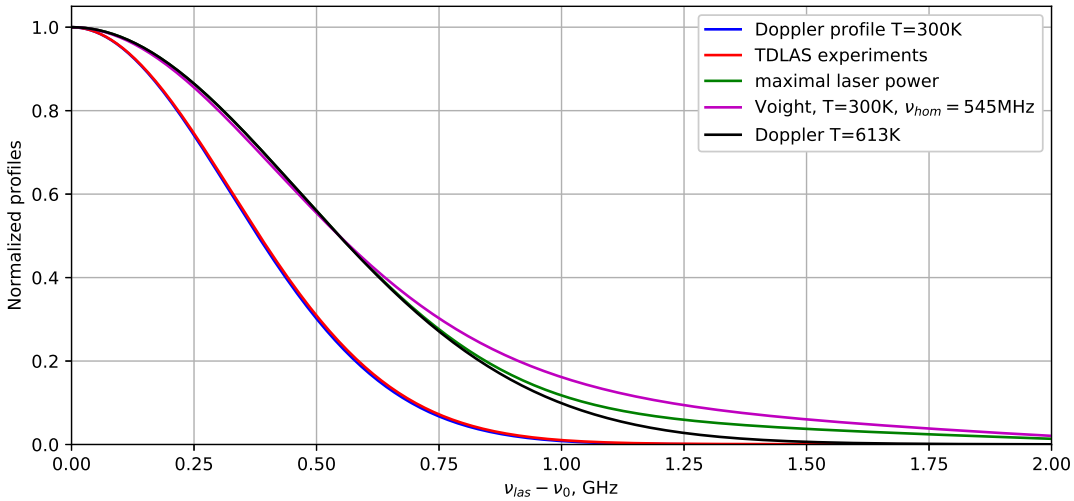

Figure 2.10: Spectral line profiles obtained with equation (2.15) for $\Delta\nu_{hom} = 10\,\mathrm{MHz}$ and the laser power of 50 mW (maximal laser power) and $1.5\,\mu\mathrm{W}$ used in the TDLAS experiments. Doppler profiles for $T = 300\,\mathrm{K}$ and $T = 613\,\mathrm{K}$ as well as a Voigt profile with $T = 300\,\mathrm{K}$ and $\Delta\nu_{hom} = 545\,\mathrm{MHz}$ are show for comparison.

2.7.3 Optogalvanic effect

The estimations above show that unattenuated beam of the used laser can strongly decrease the metastable density. It can lead to change of the discharge electrical properties causing the so-called "optogalvanic effect". The ionization energy of argon from the ground state is 15.76 eV [6], which is much higher than the electron temperature in our plasma. The bottom state of the transition pumped by the laser is the lowest metastable level, which lies only 4.21 eV below the ionization energy. Although, after additional excitation by the laser, the atom can be ionized even easier, it can spontaneously relax to the ground state (see Fig. 2.8). The optogalvanic effect is therefore determined by the interplay between the growth of the ionization rate due to the increase in the population of the upper level of the laser-pumped transition and the decrease of the ionization due to the decrease in the population of the lower level of the laser-pumped transition. The sign of the effect depends on the discharge conditions. For example, the measured effect for the 696.5 nm argon spectral line had different signs in [160] and [161].

In our case, the probability of the relaxation to $1s_2$ and $1s_4$ resonant states is one order of magnitude higher than the probability to relax to $1s_3$ metastable state [4]. According to [160], a laser pulse in 772.38 nm argon spectral line caused a positive pulse of DC discharge voltage (at constant discharge current), which implies the decrease of the ionization rate.

2.7.4 Laser influence on the emission spectrum

Although the fluorescence can be observed only in the spectral lines that have the same upper level as the transition pumped by the laser, the laser disturbs the discharge, which can be seen in its effect on other spectral lines. We measured this effect for the planar laser sheet configuration (see section 2.3.2) using Horiba iHR550 spectrometer. The laser was tuned to the center of 772.38 nm spectral line. The image of the central part of the discharge with the laser sheet was focused on the spectrometer slit. The spectra were captured by the ICCD camera. After subtraction of the dark signal, we calculated the intensity of each spectral line as a sum of pixel values that belonged to it.

In table 2.2, the relative effect of the laser on several spectral lines is presented. It was calculated as $\frac{I_{on}-I_{off}}{I_{off}}$, where I_{on} and I_{off} are the spectral line intensities with and without the laser.

Table 2.2: Relative effect of the laser on several spectral lines. The spectrometer slit width was 50 μm. The discharge power was 200 mW. The laser power was 50 mW.

Wavelength, nm	Relative effect of the laser
750.39	0.018 ± 0.002
751.47	0.021 ± 0.003
810.37	1.645 ± 0.005
811.53	-0.022 ± 0.001

The qualitative difference of the effect for 750.39 and 751.47 nm spectral lines and the effect for 811.53 nm spectral line can be explained taking into account that electron-impact excitation cross-section of the $1s_5$ metastable atoms to the $1s_9$ state is two orders of magnitude higher than to the $2p_1$ and $2p_5$ states [162,163]. $2p_9$ state is strongly populated by electron impact excitation from $1s_5$ state and therefore, its density decreases as the $1s_5$

state is depopulated by the laser. The increase of the 750.39 and 751.47 nm spectral lines intensities could be caused by a slight electron heating due to the optogalvanic effect.

Similar experiments with the two beams configuration used in the TDLAS experiments showed no local effects for 811.53 nm spectral line. It suggests that the population of $1s_5$ level decreased not only inside the beam, but in the entire discharge.

Chapter 3

Experimental results

3.1 Gas temperatures

3.1.1 Measurements with TDLAS

Results of the gas temperature measurements using TDLAS were published as [9]:

> A. Pikalev, M. Pustylnik, C. Räth, and H. Thomas, "Measurement of gas temperatures in dust-free and dusty argon discharges," *J. Phys. D: Appl. Phys.*, vol. 53, p. 075203, 2020.

We measured gas temperatures in the argon capacitively coupled RF discharge without and with the microparticles using TDLAS. The discharge power was 200 mW. The measurements were performed with two laser beams at different heights simultaneously (see section 2.2). Without external heating, the measured temperatures were $5.4 \pm 0.9\,\mathrm{K}$ higher than those of the flanges. If we heated the bottom electrode, the measured temperature difference between the beams was proportional to the temperature difference between the chamber flanges.

The experiment showed that the presence of microparticles induced growth of the gas temperature. Heating was observed on both beams and vanished with the reduction of the microparticle amount. The gas heating could be caused by non-local increase of the electron temperature as well as local gas interaction with the surfaces of the microparticles (see section 1.4). Since the observed effect was similar for both beams, the non-local mechanism seems to prevail.

3.1.2 Measurements with LIF

We tried to measure the radial temperature distribution using LIF from the same two beams that were used in the TDLAS experiments. The LIF averaged for several scanning periods is shown in figure 3.1. The experiments were conducted without microparticles. The discharge power was the same as in the TDLAS experiments. No external heating was used.

The results for the top and the bottom beams were similar, we will present here the data for the top beam. Due to lack of sensitivity, we measured the LIF with the beam power higher than it was in the TDLAS experiments. The LIF dependence on the beam power is shown in figure 3.2. The temperatures of the Doppler fit were calculated for

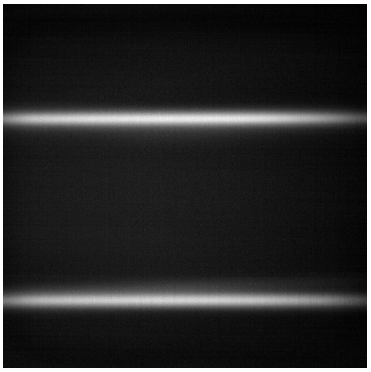

Figure 3.1: LIF signal time-averaged for several scanning periods. The plasma emission is subtracted. Power of each beam was about 107 μW. The beams entered the discharge from the right.

an area of 64x16 pixels (∼1.9x0.5 mm) in the center of the beam image. The saturation broadening is clearly visible for the beam powers higher than 20 μW. Although noise makes the results for lower powers inaccurate, the temperatures are significantly higher than the temperatures determined by the TDLAS method.

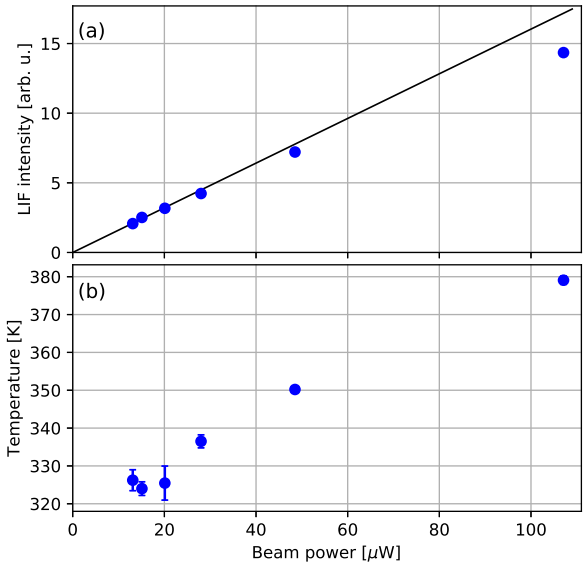

Figure 3.2: LIF dependence on the laser beam power. (a) LIF intensity averaged along the beam when the laser is tuned to the center of the spectral line. The straight line intercepts the zero point and fits the first three data points. (b) Temperatures determined by the Doppler fit of the LIF signal in the center of the beam image.

We found that the measured width of the spectral line profiles increased in the direction of the beam propagation. The effect is shown in figure 3.3. It can be explained taking into account the absorption of the laser light by the plasma. Considering linear LIF response and using Beer-Lambert law (2.1), the LIF signal spatial dependence can be written as follows

$$I_{lif}(\nu, x) \sim I_{las\,0}(\nu) \exp(-k(\nu)x)\varphi(\nu), \tag{3.1}$$

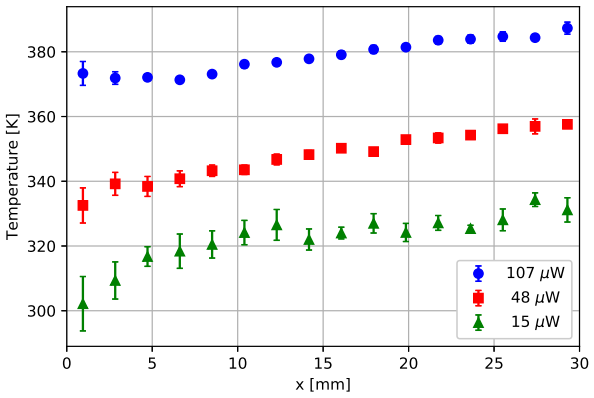

Figure 3.3: The dependence of the Doppler fit temperature on the position along the beam for different beam powers. The position 0 corresponds to the entrance of the beam into the observed area.

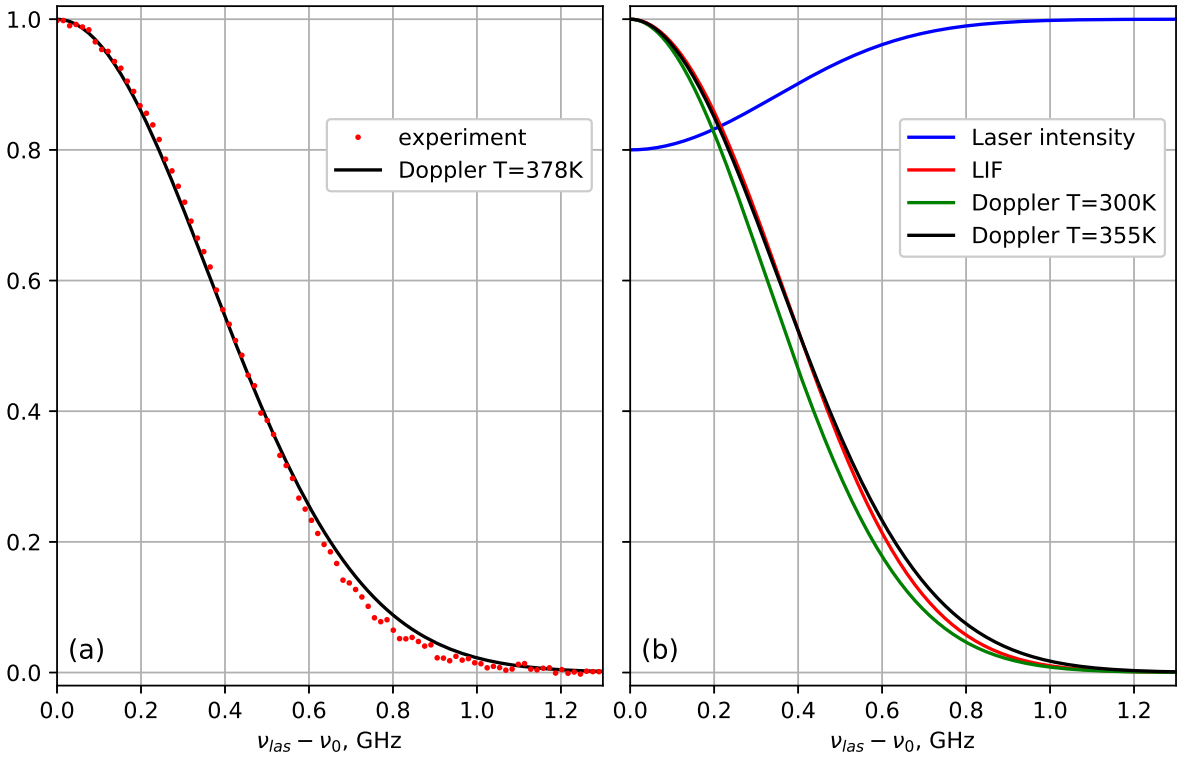

Figure 3.4: Shape of the LIF-measured spectral line profiles. (a) Experimental profile determined for the center of the beam image compared to the Doppler fit. The beam power was 107 μW. (b) Effect of the light absorption on its way to the point of LIF measurement (see equation (3.1)). The incident laser intensity is taken frequency-independent. The absorption before the considered point is taken 20% in the center of the spectral line. The real spectral line is taken with the Doppler shape ($T = 300\,\mathrm{K}$).

where $I_{las\,0}$ is the incident laser intensity before entering the plasma, ν is the laser frequency, $I_{las\,0}(\nu)\exp(-k(\nu)x)$ is the laser intensity at point x, which is disturbed by the absorption (see the blue line in figure 3.4(b)), and $\varphi(\nu)$ is the profile of the absorption spectral line. This problem was also discussed in [151].

In the case of high beam power, the absorption and LIF become non-linear. It makes the effect less pronounced and can correspond to the lower dependency slope for higher laser intensity in figure 3.3.

This effect can also be seen in the shape of the spectral line profile. The experimental profile (figure 3.4(a)) is qualitatively similar to the profile calculated using expression (3.1) (figure 3.4(b)). In comparison with the Doppler fit, the profiles are wider near their peak, but have thinner wings. It distinguishes them from both the Voigt profile and the saturation-broadened profile discussed in section 2.7.2.

3.2 Metastable density

3.2.1 Measurements with TDLAS

Results of the metastable density measurements using TDLAS were published as [9]:

> A. Pikalev, M. Pustylnik, C. Räth, and H. Thomas, "Measurement of gas temperatures in dust-free and dusty argon discharges," *J. Phys. D: Appl. Phys.*, vol. 53, p. 075203, 2020.

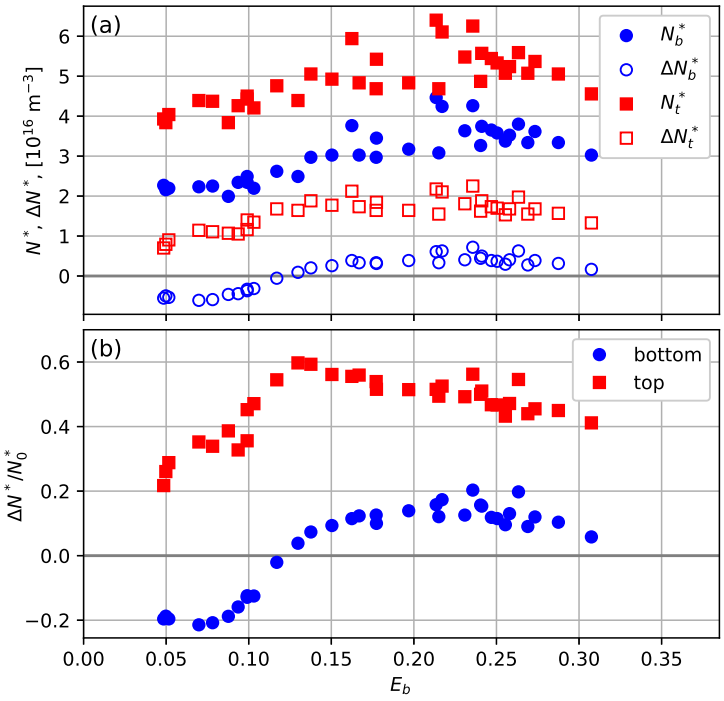

Figure 3.5: Effect of the microparticles on the metastable densities measured by the top (red symbols) and the bottom (blue symbols) beams. (a) Absolute values of the metastable densities (N^*) and their changes $\Delta N^* = N^* - N_0^*$ in comparison with the plasma without microparticles (N_0^*). (b) Relative changes of the metastable densities. The abscissa is the fraction of laser light extinguished by the microparticles, which characterizes their amount. See [9] for details.

Together with the temperature, TDLAS measurements (section 3.1.1) allowed us to determine the line-averaged densities of the metastables. The results are summarized in figure 3.5.

The effect depends on the amount of the microparticles. We used the fraction of laser light extinguished by the microparticles from the bottom beam E_b as a measure of their amount. The presence of the microparticles always caused growth of the absorption for the top beam. On the other hand, small suspensions caused a decrease of the absorption for the bottom beam, whereas large suspensions that filled the entire discharge volume induced the absorption growth for both beams.

3.2.2 Measurements with LIF

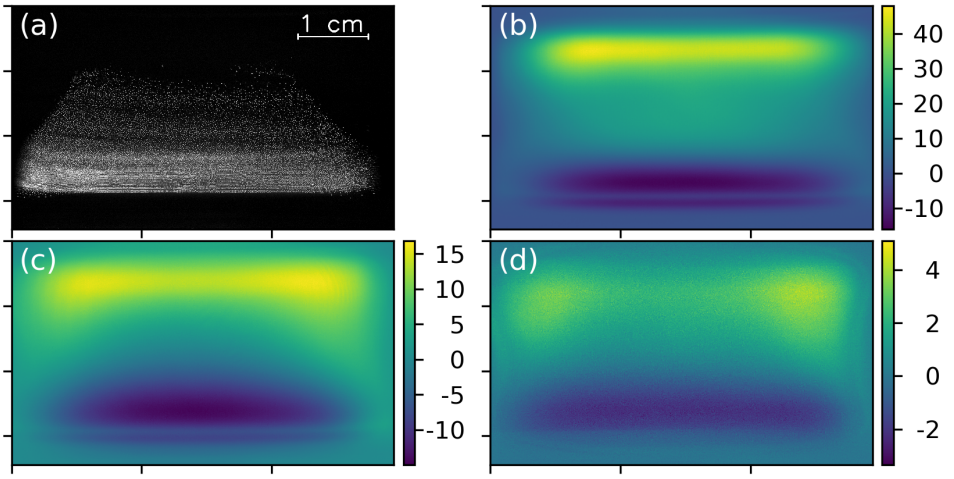

Figure 3.6: (a) Image of a microparticle suspension and the effect of the suspension on the plasma emission in (b) 750/751 nm and (c) 810/811 nm spectral lines as well as (d) on LIF. The plasma emission / LIF without the microparticles is subtracted from images (b)–(d). Images (a)–(c) were captured without the laser. No temperature gradient was applied. The discharge power was 200 mW. The intensities are in arbitrary units.

The effect of the microparticle suspension on the metastable density is measured using the TDLAS method only at two heights, and the results are averaged along the laser beams. We overcame this limitations using planar LIF (see section 2.3.2). Typical results are shown in figures 3.6–3.8. The measured effect of the microparticles on the LIF is accompanied by the effect on the plasma emission. The LIF and plasma emission of the discharge without the microparticles are subtracted. The laser intensity was attenuated by a neutral-density filter with the transmission of 12 %. The experiments were conducted with the gas pressure of 37 Pa.

The effect of a relatively small suspension without the thermophoretic gravity compensation is shown in figure 3.6. The results are in accord with the TDLAS measurements. The small suspension decreased the metastable density in the bottom and increased it in the top. The effect on the plasma emission looks similar. Locality of the LIF measurements allows to resolve that the area with the highest increase of the metastable density has a toroidal shape.

Using the planar LIF technique, we investigated the void. In [65], no void-related emission feature was found. Such a feature could be hidden due to averaging along the line of sight. Therefore, the local measurements are required. We reproduced the void formation with the same discharge power as in [65]. The results are presented in figure

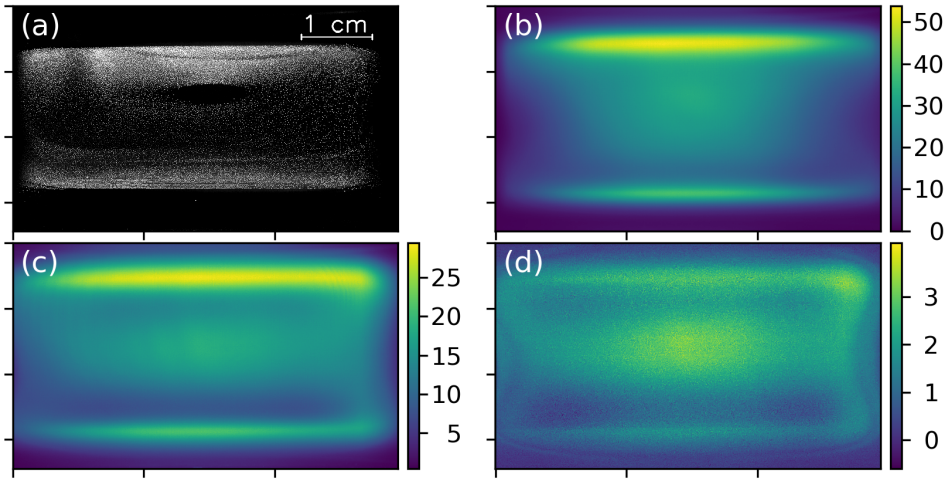

Figure 3.7: (a) Image of a microparticle suspension and the effect of the suspension on the plasma emission in (b) 750/751 nm and (c) 810/811 nm spectral lines as well as (d) on LIF. The plasma emission / LIF without the microparticles is subtracted from images (b)–(d). Images (a)–(c) were captured without the laser. Gravity was compensated by the thermophoresis. The discharge power was 200 mW. The intensities are in arbitrary units.

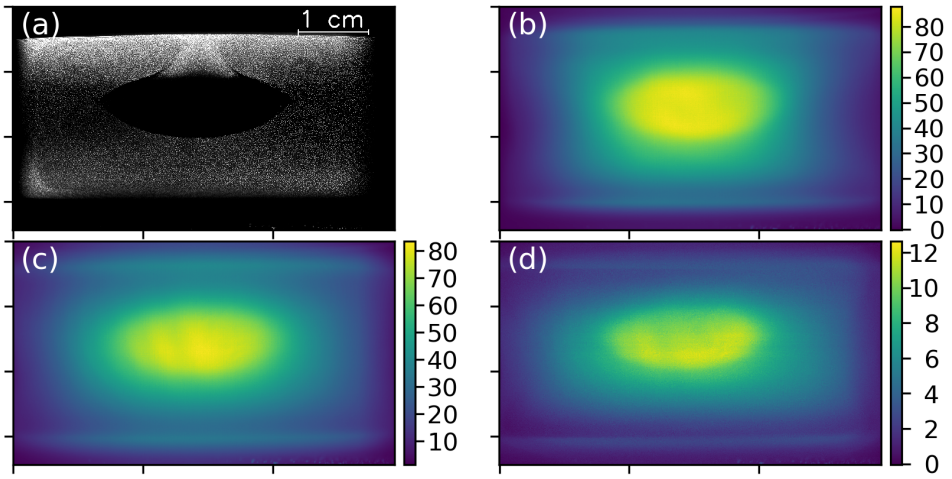

Figure 3.8: (a) Image of a microparticle suspension and the effect of the suspension on the plasma emission in (b) 750/751 nm and (c) 810/811 nm spectral lines as well as (d) on LIF. The plasma emission / LIF without the microparticles is subtracted from images (b)–(d). Images (a)–(c) were captured without the laser. Gravity was compensated by the thermophoresis. The discharge power was 1 W. The intensities are in arbitrary units.

3.7. The increase of the metastable density in the discharge center is diffuse, and no coupling with the void can be seen.

We repeated the experiment with the discharge power of 1 W (see figure 3.8). In this case, both the plasma emission and the metastable density increased drastically inside the void.

3.3 Dim and bright void regimes

The dim and bright void regimes are described in [1]:

> A. Pikalev, I. Semenov, M. Pustylnik, C. Räth, and H. Thomas, "Dim and bright void regimes in capacitively-coupled RF complex plasmas," *Plasma Sources Sci. Technol.*, vol. 30, p. 035014, 2021.

The contribution of the doctoral candidate to this paper includes conducting the experiments, analyzing data, discussing the results and writing the text. Below we summarize the main published results. Additionally, we show here transient processes in the complex plasma induced by a discharge power increase.

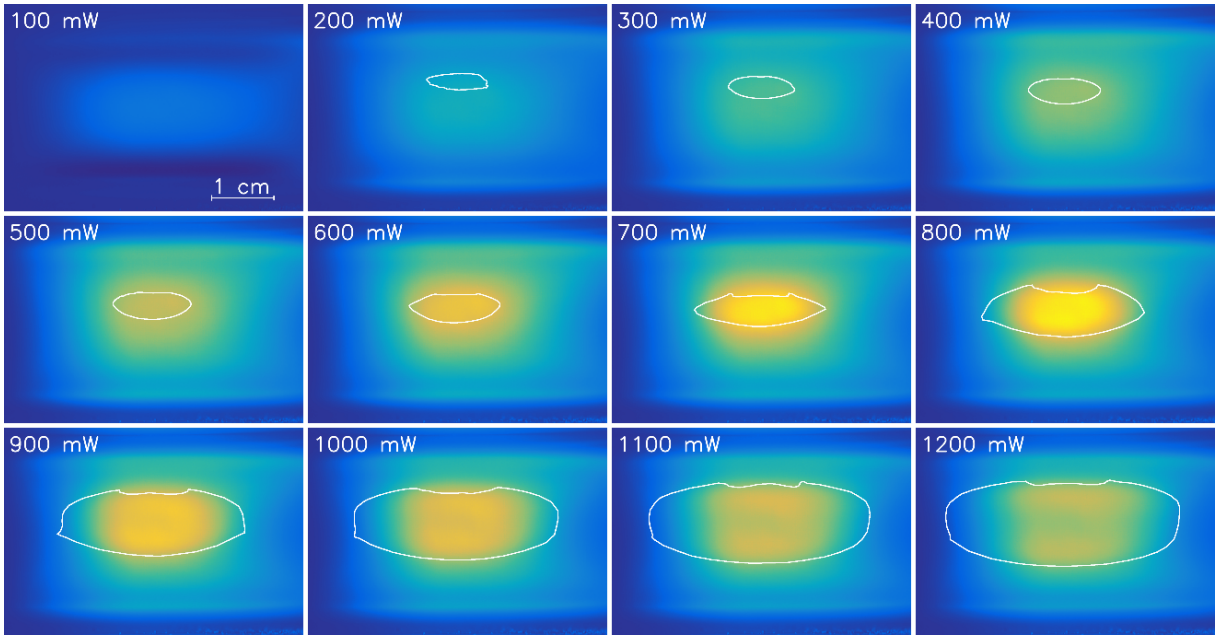

Figure 3.9: The colour-coded effect of the microparticles on the plasma emission with the filter for 750 nm. The plasma emission without the microparticles is subtracted. The discharge power was increased from 100 mW to 1200 mW in steps of 100 mW. The pressure was 37 Pa. The white lines depict the void boundaries.

We performed a systematic investigation of the plasma emission coming from the void area. We have experimentally shown that the void can exist in two regimes, which we termed "dim" and "bright". An example of a transition between the regimes is shown in figure 3.9. The dim void forms at relatively low discharge powers (200–500 mW in figure 3.9) and exhibits no emission feature associated with it. With the increase of the discharge power ($>$ 600 mW in figure 3.9), the bright emission from the void appears, i.e. the void experiences a transition from dim to bright regime. With further discharge power increase, the plasma emission concentrates near the top and bottom void boundaries, especially at higher gas pressure (1000–1200 mW in figure 3.9).

The transition between the regimes has a discontinuous character. The threshold is manifested by a kink in the void size power dependencies. Also, the microparticle density peak at the void boundary disappears with the power growth.

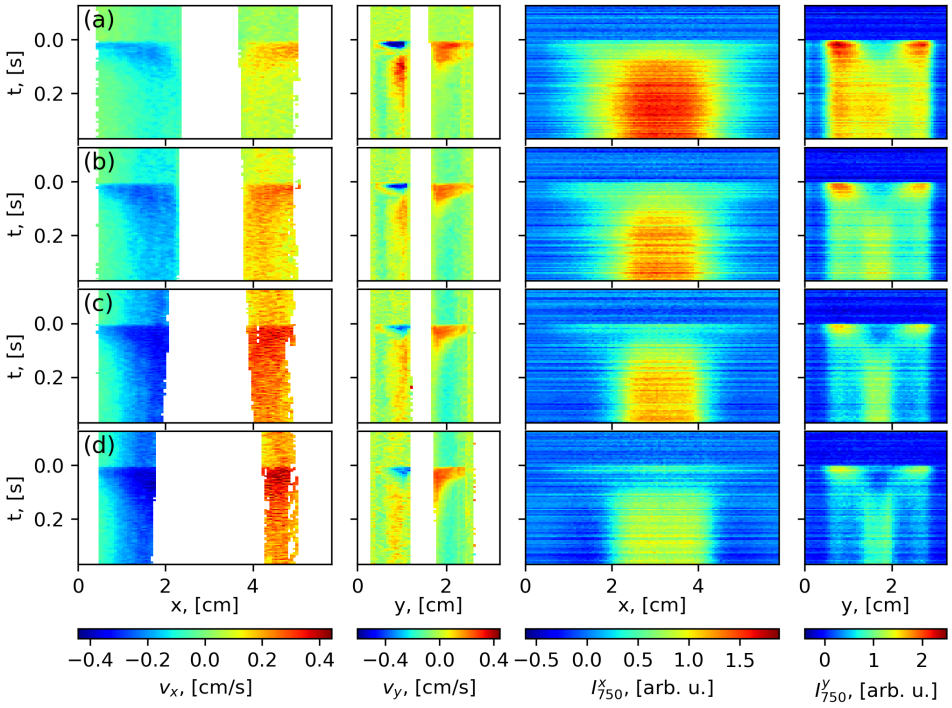

Figure 3.10: Effect of the power increase during the transition from the dim to the bright void regime. The discharge power was increased by 50 mW from (a) 450, (b) 550, (c) 650 and (d) 750 mW. Spatiotemporal distributions represent (from the left to the right) the velocity (v_x, v_y) and the plasma emission variations I^x_{750} and I^y_{750}. White color in the v_x and v_y plots depicts the areas in which no microparticles are present. The microparticle diameter was 2.15 μm. The time-averaged intensities for lower discharge power were subtracted from I^x_{750} and I^y_{750} in each line. The spatiotemporal distributions are calculated in the same way as in [10].

The plasma reaction on the power increase of 50 mW is shown in figure 3.10 for different discharge powers around the transition. In all cases, the plasma emission shortly increased near the sheaths just after the power increase and then the emission increase redistributed in the bulk. In the dim void regime, the emission increase became diffuse after the transient processes, but after the transition to the bright regime, the emission increased primary in the void area. Even a decrease of the emission around the void could be seen in the horizontal emission distribution for the highest power (figure 3.10 (d)).

RF-period-resolved optical emission spectroscopy revealed that the presence of the microparticles increases the emission in the entire axial extension of the discharge every half of the period in the case of the dim void, whereas for the bright void, the emission increase appears only between the expanding sheath and the opposite void boundary.

The void formation was analyzed by means of a simplified 1D fluid model [1]. The model could reproduce the bright void. The bright emission in the void is caused by the strong time-averaged electric field at the void boundary. In this case, the balance between ion drag and electrostatic forces can only be satisfied at the elevated ion density (see figure 1.1), that is why the bright void needs higher discharge power.

On the contrary, the dim void could not be obtained within the framework of the same 1D model: the bright void was closing with the decrease of the ionization rate

as soon as the ion drag force was unable to balance the electrostatic force. Dim void could be, however, obtained by artificially including a radial diffusion term into the ion flux continuity equation. Electric field at the void boundary was in this case two orders of magnitude lower than that in the bright void regime. Therefore, it did not lead to the appearance of the emission on the void boundary. The modified model was able to qualitatively explain the experimentally observed dim void formation including its RF-period-resolved spatiotemporal emission profile. At the same time, inclusion of the radial diffusion for the conditions of the bright void did not lead to qualitative changes.

We could therefore, demonstrate that the void in dim and bright void regimes forms due to two different mechanisms. These mechanisms correspond to the two principles of self-organization discussed in section 1.3.2. Complete understanding of the dark void formation requires a self-consistent 2D model of a dusty CCRF discharge and local measurements of the electric field or ion velocity distribution.

3.4 Heartbeat instability

3.4.1 Published results: Experimental observations and the heartbeat cycle

Our results of the research of the heartbeat instability are published as [10]:

> A. Pikalev, M. Pustylnik, C. Räth, and H. Thomas, "Heartbeat instability as auto-oscillation between dim and bright void regimes", *Phys. Rev. E*, vol. 104, p. 045212, 2021.

In this section, we summarize the main results from the paper. In further sections, we present some additional experimental results.

The transition of the void from the dim to the bright regime has some similarities with the heartbeat instability, which is accompanied by a bright flash inside the void just before its contraction (see section 1.6). We investigated the heartbeat instability using the system of three cameras shown in figure 2.3. We paid special attention to the optogalvanic control of the instability. The optical scheme for it was similar to that of the planar LIF experiments. We, however, substituted a cylindrical lens, which converted a cylindrical laser beam into a sheet, by a mechanical chopper that modulated the cylindrical beam.

We reproduced earlier reported behaviour of the plasma emission during the heartbeat instability, small breathing oscillations that appear in the suspension between the void contractions, and resonant optogalvanic stimulation of the instability (see section 1.6 and references therein). It was demonstrated that the resonance is observed when the laser modulation frequency coincides with the frequency of the breathing oscillations. The experiments with high laser power revealed that individual laser switching can cause the void contraction transiently. The void contracts after closing of the laser beam if it passes through the void center, and after opening of the laser beam if it was shifted horizontally to the void periphery. However, continuous laser beam stabilizes the microparticle suspension.

The experimental results allow us to describe the cycle of the heartbeat instability. It starts from a microparticle suspension with a dim void. In the case of self-excitation, the breathing oscillations start to develop inside this suspension. After the breathing oscillations reach a certain amplitude, the dim void undergoes a critical transformation to the

bright regime. In the case of transient laser excitation, the transition to the bright regime occurs due to the laser-induced transient process in the plasma. In the case of resonant laser excitation, the laser excites the breathing oscillations, which, in their turn, trigger the transition from the dim void regime to the bright void regime. In the bright regime, the void boundary becomes mechanically unstable and the void collapses due to large electrostatic forces on its boundaries. After the collapse, when the unstable void boundary is destroyed, the microparticles start to move back and restore the dim-void configuration.

3.4.2 Properties of the heartbeat instability for different discharge powers

Properties of the heartbeat instability are strongly dependent on the discharge power. This effect is demonstrated in figure 3.11. In this experiment, the discharge power was increased from 450 mW to 800 mW in steps of 50 mW. The frames used to calculate the spatiotemporal patterns were captured 0.5–1.5 s after power switching.

For the lowest presented discharge power (figure 3.11 (a)), the heartbeat did not occur, only small oscillations of the microparticle motion and the plasma emission can be seen with the frequency of 32–40 Hz. After the discharge power was increased to 500 mW, the small oscillations became stable and their amplitude increased. Their frequency was 40 ± 2 Hz. At a certain moment, the void started contracting irregularly (figure 3.11 (b)) with 1–3 small oscillations between the contractions. With further discharge power increase, the number of the small oscillations between the void contractions was decreasing, and when the power reached 700 mW, all oscillations had similar amplitude (figure 3.11 (f)). Their frequency continued growing with the power increase. It was 25 ± 1 Hz for 700 mW, 26.5 ± 1 Hz for 750 mW and 34 ± 1 Hz for 800 mW. The amplitudes of the horizontal velocities during the contraction, the flashes inside the void and the void size variations were decreasing with the discharge power increase after onset of the heartbeat instability.

3.4.3 Effect of the laser on small breathing oscillations

The experiments clearly show that the laser beam passing through the void can prevent the heartbeat instability. The self-excited heartbeat is observed together with the small breathing oscillations, which are supposed to be a precursor to the void contraction. In the experiment shown in figure 4 in [10], the oscillations are visible when the laser was open and the void contractions were suppressed in the case of modulated laser, however, no oscillations were detected in the case of the continuous laser beam. Investigation of the laser influence on these oscillations could help to understand their coupling with the void contractions.

We investigated the dependency of the frequency and the damping rate of the oscillations on the laser power. The chopper was equipped with neutral density filters with different transmission. An example of the spatiotemporal distributions for this experiment is shown in figure 6 in [10]. The oscillations were excited by the laser opening. A laser opening caused the outward microparticle motion with respect to the void (see figure 3.12(a)). We analyzed the oscillations of the spatially averaged horizontal velocities. The oscillations (excluding the first one) propagated from the edge of the suspension to the center causing a slope of the velocity pattern in the spatiotemporal distributions, which we had to take into account for averaging. Similar slop can be seen for the small oscillations in figure 3.11 (b).

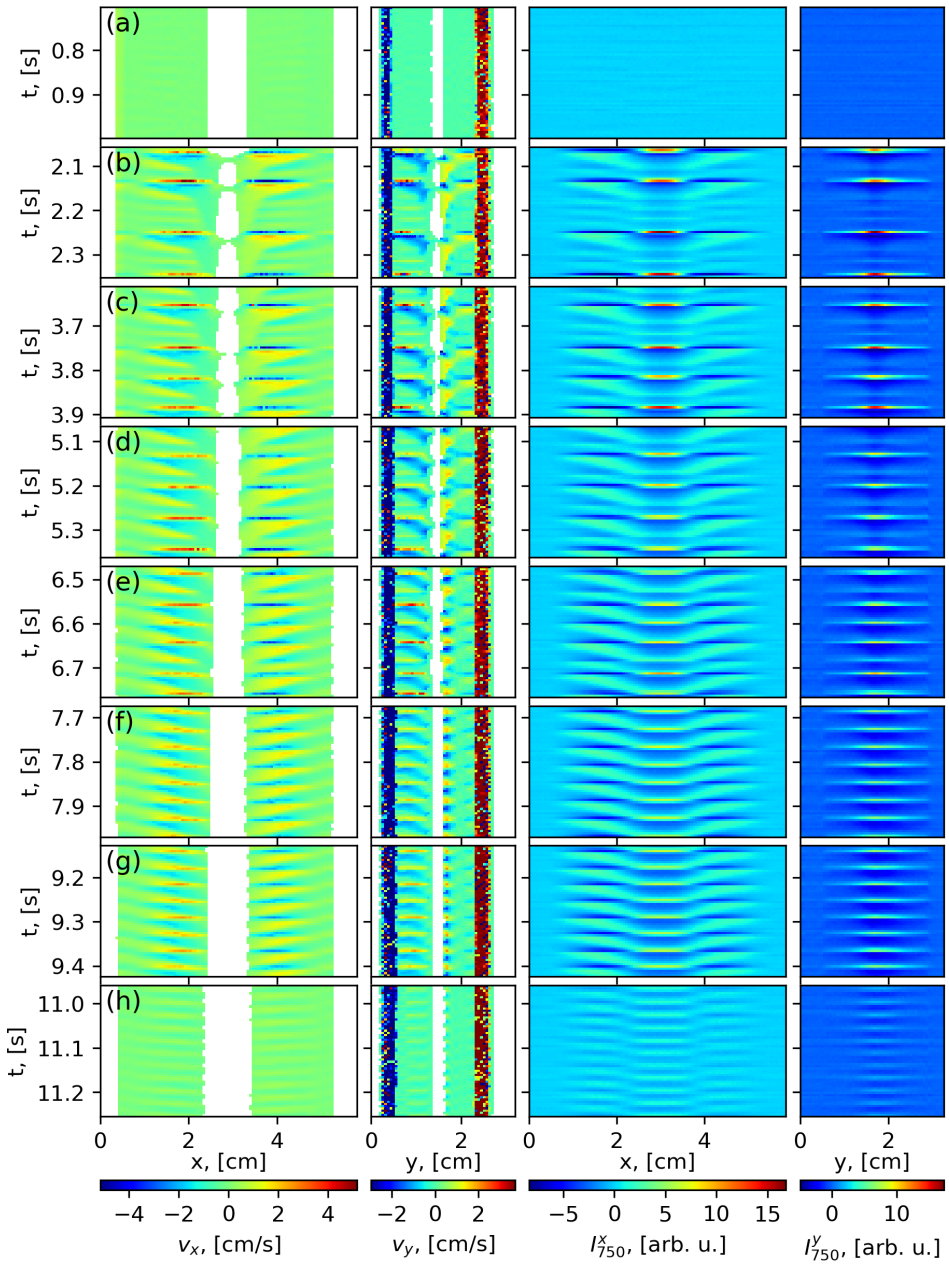

Figure 3.11: The heartbeat instability with the discharge power of (a) 450, (b) 500, (c) 550, (d) 600, (e) 650, (f) 700, (g) 750, (h) 800 mW. Spatiotemporal distributions represent (from the left to the right) the velocity (v_x, v_y) and the plasma emission variations (I^x_{750}, I^y_{750}). White color in the v_x and v_y plots depicts the areas in which no microparticles are present. The microparticle diameter was 2.15 μm. The preparation of the spatiotemporal distributions was described in [10].

We fit the data with expression:

$$v_x = v_{xa}\, e^{-\gamma t} \cos(2\pi f t + \varphi_0) + v_{x0} + v'_{x0} t. \tag{3.2}$$

The fitting parameters are the initial amplitude v_{xa}, the damping rate γ, the frequency f, the phase shift φ_0, the continuous drift of the microparticles v_{x0} and its change due to slow processes v'_{x0}.

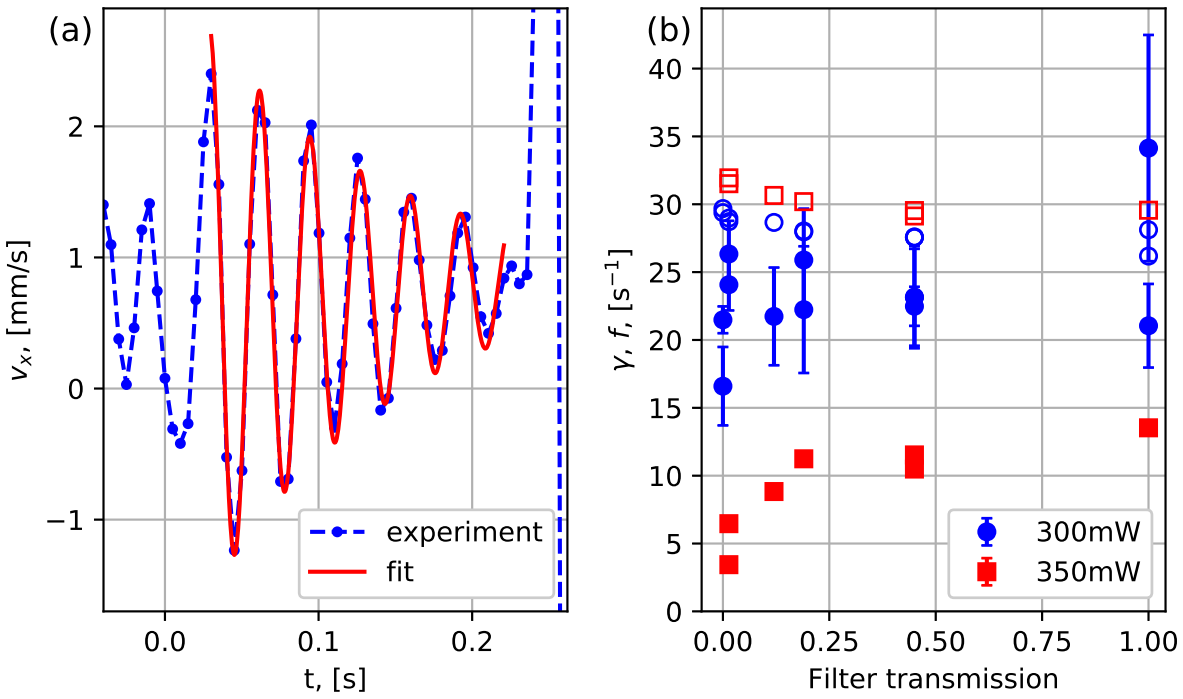

Figure 3.12: (a) An example of the v_x oscillations. The discharge power was 350 mW and the filter transmission was 0.12. The laser was opened at $t = 0$ and closed at $t = 0.23$ s. Positive values mean the motion in the direction to the void. (b) The damping rates (filled symbols) and frequencies (empty symbols) of the oscillations. The error bars for the damping rates depict the standard deviation of the fitting results with small variation of the used point interval. The standard deviations for the frequencies are less than the symbol size. The points with the filter transmission of 0 were obtained for the oscillations after the laser closing when it did not cause the void collapse.

The first data point for the fit was chosen after the first maximum of the signal, and the last point was before the laser closing or when the oscillations became invisible (see figure 3.12(a)). The damping rates and the frequencies for the discharge powers of 300 and 350 mW are presented in figure 3.12(b). In the case with the discharge power of 300 mW, the damping rates were so high that the fits are based on 2–4 oscillation periods. It makes the determined damping rates very inaccurate. It can be seen in large standard deviations which were obtained by excluding 1–2 points from the beginning or the end of the fitted signals.

In the experiments with the discharge power of 200 and 250 mW, a short microparticle motion without oscillations was observed just after the laser opening/closing. The small oscillations were self-excited with the discharge power of 500 mW without the laser and were not visible with the continuous laser.

The obtained damping rates are significantly lower than the damping due the gas friction (see equation 2.4). It means that there is an excitation mechanism that supplies energy to this mode. The experimental results suggest that the laser could diminish this mechanism increasing the damping rates.

3.4.4 Effect of the laser for stable dim and bright void

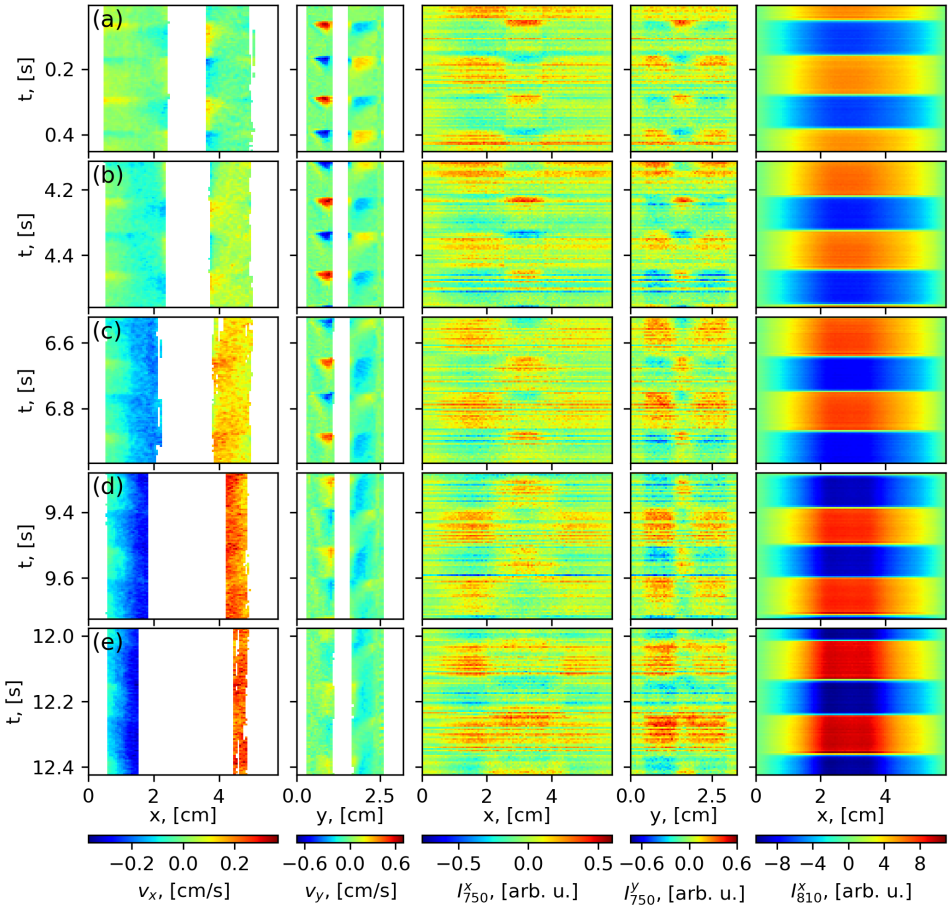

Figure 3.13: Effect of the modulated laser beam passing through the void with increasing discharge power. The discharge power was (a) 400, (b) 500, (c) 600, (d) 700 and (e) 800 mW. Spatiotemporal distributions represent (from the left to the right) the velocity (v_x, v_y) and the plasma emission variations I^x_{750}, I^y_{750} and I^x_{810}. White color in the v_x and v_y plots depicts the areas in which no microparticles are present. The microparticle diameter was 2.15 μm. The intensity in I^x_{750} patterns out of the void area varies due to the laser light scattered by the microparticles, which is not completely stopped the the 750 nm filter. The time-averaged intensities inside the void area captured by the camera with 750 nm filter are (a) 25, (b) 28, (c) 31, (d) 33 and (e) 36 arb. u.

We investigated the effect of the laser with different discharge powers. The amount of the microparticles was so low that neither self-excited nor transient stimulated heartbeat instability occurred. The laser beam passed through the void and was modulated with the frequency of 4.5 Hz. We increased the discharge power from 400 to 800 mW in steps of 100 mW. The results are presented in figure 3.13. The frames used to build the spatiotemporal patterns were captured 1.5–2 s after power switching.

For the lowest discharge powers (400 and 500 mW), a flash appeared in the void just after the laser closing, and the plasma emission became dimmer for a shot time after its opening. Although this effect is weak, it is qualitatively similar to our observations of the transient heartbeat stimulation. For higher discharge power (700 mW, figure 3.13(d)), the plasma in the void became brighter during the entire time when the laser was closed.

For the discharge power of 800 mW (figure 3.13(e)), the void became brighter after the laser opening and dimmer after its closing. This difference for the discharge powers of 700 and 800 mW could be attributed to crossing the maximum of the emission intensity in the void center after the transition to the bright regime (see figure 3.9).

The variation of the emission distribution along the discharge axes looks different in this experiment in comparison with the transient heartbeat stimulation. In the experiments with the heartbeat instability, the plasma emission increased along the entire discharge axes during the flash. In this experiment, we see that the plasma emission became dimmer above and under the void during the flash. Also, we see in figure 3.13 clearly that the plasma emission above and under the void became brighter when the laser is open. This effect is also detectable in the experiments with the transient heartbeat stimulation. We cannot make a conclusion about the horizontal distribution of plasma emission due to the tunable laser light scattered on the microparticles. This light is partially transmitted by the 750 nm filter causing the intensity increase when the laser was open.

3.4.5 Void contraction induced by a rapid increase of the discharge power

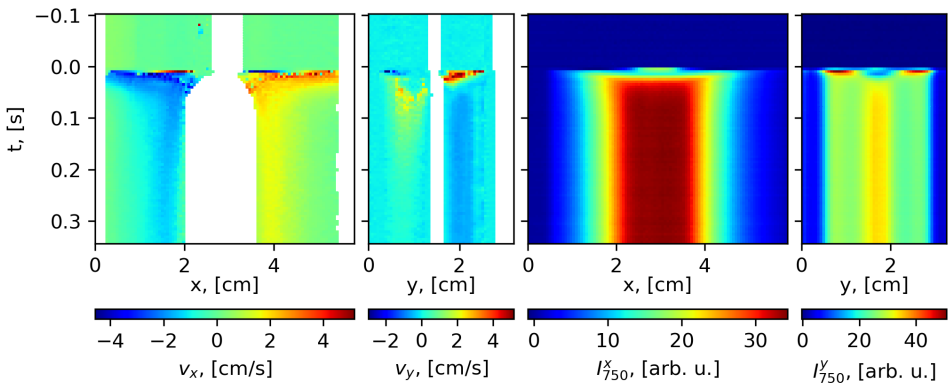

Figure 3.14: The void contraction induced by a rapid change of the discharge power from 500 to 1000 mW. Spatiotemporal distributions represent (from the left to the right) the velocity (v_x, v_y) and the plasma emission variations I^x_{750} and I^y_{750}. The average plasma emission for the lower discharge power is subtracted.

The void contraction can be also induced by a rapid increase of the discharge power. In the experiment presented in figure 3.14, the amount of the microparticles was relatively high, but less than needed for the heartbeat self-excitation at any discharge power. At the beginning, the discharge power was 500 mW and the void was dim. Then, we increased the power to 1000 mW in a single step. Just after the power increase, a short flash can be seen in the void and the void contracts. The flash in the void is not detectable in the experiment with smaller power steps presented in figure 3.10. Another flash appeared near the sheath after the flash in the void. Then the void expanded to a new size, drifted to a new position and became bright.

Chapter 4

Conclusion

Microparticle-plasma interactions are crucial for many phenomena in complex plasmas. Their understanding is still incomplete and published results sometimes look contradictory. In this work, we characterized these interactions in capacitively-coupled RF discharge using optical emission spectroscopy (OES), tunable diode laser absorption spectroscopy (TDLAS) and laser induced fluorescence (LIF). In these experiments, we discovered several new effects advancing the understanding of the void formation and the heartbeat instability.

The gas temperature distribution determines the thermophoretic force. This force can be used to compensate gravity in ground experiments, whereas it is a disturbing factor in microgravity. We measured the temperature using TDLAS. Accurate experiments and developed technique of data analysis allowed to detect the microparticle induced gas heating by 1–2 K. Although this effect is negligible in terms of the neutral gas dynamics, it suggests that the microparticles can induce gas temperature gradients and thermophoretic forces significant for the microparticle dynamics. The experiment also allowed us to determine the metastable density and the effect of the microparticles on it. The metastables, as it was demonstrated in our experiments with the optogalvanic effect, play a significant role in the ionization balance.

The TDLAS measurements were performed at two heights, and their results were averaged along the beams. To overcome these limitations and obtain two-dimensional (2D) distributions, we established LIF diagnostics. Although the accuracy of the LIF temperature measurements was too low, the planar LIF measurements gave qualitative 2D distributions of the metastable atoms. The measurements showed that the effect of the microparticles on the metastable density is qualitatively similar to their effect on the plasma emission.

The void in complex plasmas has been investigated for decades. However, some aspects of its physics are still unclear. Attempts to simulate the void formation using particle-in-cell codes [61, 65] were unsuccessful. The reported spectroscopic observations of complex plasmas with the void looked contradictory: In some cases, the plasma emission was diffuse [65, 112], whereas a bright emission from the void area was observed in other experiments [61, 130, 131]. Our experiments with OES and RF-period-resolved OES revealed that the void can exist in two qualitatively different regimes: “dim” and “bright”. The dim void appears at lower discharge powers and discontinuously transits to the bright regime with the power being increased.

The simplified one-dimensional (1D) fluid model explained the difference in the plasma emission between the regimes by the difference in time-averaged electric field. In the bright

regime, the time-averaged electric field at the void boundary heats the electrons causing bright plasma emission inside the void. The dim void has much lower electric field at the boundary and exhibits therefore no emission feature associated with it. The model reproduced the dim void formation only when radial ion losses were artificially introduced to the continuity equation. According to the model, the void regime is determined by the ionization rate. Complete understanding of the void formation in different regimes requires a self-consistent 2D model and local measurements of the electric field or ion velocity distribution.

Our experiments demonstrated that the laser tuned to an atomic transition can significantly change the discharge conditions. According to our estimations, the unattenuated laser beam reduces the metastable density by a factor of five causing a decrease of the ionization rate. We used this effect to control the heartbeat instability and found out that the continuous laser beam can stabilize the microparticle suspension whereas the modulated laser can induce the void contractions either transiently or resonantly. The resonance was observed when the modulation frequency coincided with the frequency of the small breathing oscillations, which are supposed to be a precursor for the heartbeat instability.

The experiments and the theory of dim and bright void regimes suggested that the void contraction occurs due to an abrupt transition of the dim void to the bright regime. Decreasing the ionization rate, the laser shifts the conditions to the dim void regime, whereas transient processes induced by the laser switching can cause a transition to the bright regime with an unstable void configuration. Hence, the optogalvanic control allows to experimentally separate the void collapse from the breathing oscillations. A full understanding of the instability is still unavailable. Complexity and multi-timescale nature of the heartbeat instability make its simulation quite a difficult task. We managed to decompose the instability cycle into individual stages, which can be investigated separately.

The presented results could advance both fundamental science and applications of complex plasmas. The understanding of the void formation is required for experiments with complex plasma in microgravity conditions, such as the next-generation facility COMPACT (formerly, EKoPlasma) [108], where the void is the most common disturbance of the plasma homogeneity. It could also be useful for plasma chemistry since the nanoparticle generation cycle is determined by the void, and different instabilities, including the heartbeat instability, can appear at different stages of the nanoparticle growth [140].

The improvements of the experimental methods, such as the precise gas temperature measurements, could be applied to other low temperature plasmas. The optogalvanic method is supposed to be useful for investigation of the oscillatory properties of the microparticle suspensions as well as other instabilities in complex plasmas. In principle, it could also be adopted for other areas of low temperature plasma research, for example, to control instabilities in electronegative plasmas or stratification of the positive column.

Bibliography

[1] A. Pikalev, I. Semenov, M. Pustylnik, C. Räth, and H. Thomas, "Dim and bright void regimes in capacitively-coupled RF complex plasmas," *Plasma Sources Sci. Technol.*, vol. 30, p. 035014, mar 2021.

[2] A. M. Lipaev, S. A. Khrapak, V. I. Molotkov, G. E. Morfill, V. E. Fortov, A. V. Ivlev, H. M. Thomas, A. G. Khrapak, V. N. Naumkin, A. I. Ivanov, S. E. Tretschev, and G. I. Padalka, "Void closure in complex plasmas under microgravity conditions," *Phys. Rev. Lett.*, vol. 98, p. 265006, Jun 2007.

[3] M. Y. Pustylnik, A. A. Pikalev, A. V. Zobnin, I. L. Semenov, H. M. Thomas, and O. F. Petrov, "Physical aspects of dust–plasma interactions," *Contrib. Plasma Phys.*, vol. 61, no. 10, p. e202100126, 2021.

[4] W. L. Wiese, J. W. Brault, K. Danzmann, V. Helbig, and M. Kock, "Unified set of atomic transition probabilities for neutral argon," *Phys. Rev. A*, vol. 39, pp. 2461–2471, Mar 1989.

[5] G. Norlén, "Wavelengths and energy levels of ar i and ar II based on new interferometric measurements in the region 3 400-9 800 Å," *Phys. Scr.*, vol. 8, pp. 249–268, dec 1973.

[6] L. Minnhagen, "Spectrum and the energy levels of neutral argon, Ar I," *J. Opt. Soc. Am.*, vol. 63, pp. 1185–1198, Oct 1973.

[7] A. Kramida, Yu. Ralchenko, J. Reader, and and NIST ASD Team. NIST Atomic Spectra Database (ver. 5.8), [Online]. Available: `https://physics.nist.gov/asd` [2021, April 23]. National Institute of Standards and Technology, Gaithersburg, MD., 2020.

[8] W. Whaling, W. H. C. Anderson, M. T. Carle, J. W. Brault, and H. A. Zarem, "Argon I lines produced in a hollow cathode source, 332 nm to 5865 nm," *J. Res. Nat. Inst. Stand. Technol.*, vol. 107, p. 149, mar 2002.

[9] A. Pikalev, M. Pustylnik, C. Räth, and H. Thomas, "Measurement of gas temperatures in dust-free and dusty argon discharges," *J. Phys. D: Appl. Phys.*, vol. 53, p. 075203, dec 2020.

[10] A. Pikalev, M. Pustylnik, C. Räth, and H. M. Thomas, "Heartbeat instability as auto-oscillation between dim and bright void regimes," *Phys. Rev. E*, vol. 104, p. 045212, Oct 2021.

[11] D. P. Lymberopoulos and D. J. Economou, "Fluid simulations of glow discharges: Effect of metastable atoms in argon," *J. Appl. Phys.*, vol. 73, no. 8, pp. 3668–3679, 1993.

[12] V. N. Tsytovich, "Dust plasma crystals, drops, and clouds," *Phys. Usp.*, vol. 40, no. 1, pp. 53–94, 1997.

[13] P. Shukla and A. Mamun, *Introduction to Dusty Plasma Physics*. CRC Press, May 2001.

[14] V. E. Fortov, A. G. Khrapak, S. A. Khrapak, V. I. Molotkov, and O. F. Petrov, "Dusty plasmas," *Phys. Usp.*, vol. 47, pp. 447–492, May 2004.

[15] S. Vladimirov, A. Samarian, and K. Ostrikov, *Physics And Applications Of Complex Plasmas*. World Scientific Publishing Company, 2005.

[16] V. E. Fortov and G. E. Morfill, eds., *Complex and Dusty Plasmas*. Boca Raton: CRC Press, Dec. 2009.

[17] G. E. Morfill and A. V. Ivlev, "Complex plasmas: An interdisciplinary research field," *Rev. Mod. Phys.*, vol. 81, pp. 1353–1404, Oct 2009.

[18] A. Ivlev, H. Löwen, G. Morfill, and C. P. Royall, *Complex Plasmas and Colloidal Dispersions: Particle-Resolved Studies of Classical Liquids and Solids*, vol. 5 of *Series in Soft Condensed Matter*. World Scientific Publishing Co. Pte. Ltd., 2012.

[19] U. R. Kortshagen, R. M. Sankaran, R. N. Pereira, S. L. Girshick, J. J. Wu, and E. S. Aydil, "Nonthermal plasma synthesis of nanocrystals: Fundamental principles, materials, and applications," *Chem. Rev.*, vol. 116, pp. 11061–11127, Aug. 2016.

[20] C. R. Vandenabeele and S. Lucas, "Technological challenges and progress in nanomaterials plasma surface modification – a review," *Materials Science and Engineering: R: Reports*, vol. 139, p. 100521, Jan. 2020.

[21] A. V. Ivlev, G. E. Morfill, H. M. Thomas, C. Räth, G. Joyce, P. Huber, R. Kompaneets, V. E. Fortov, A. M. Lipaev, V. I. Molotkov, T. Reiter, M. Turin, and P. Vinogradov, "First observation of electrorheological plasmas," *Phys. Rev. Lett.*, vol. 100, p. 095003, 2008.

[22] S. Zhdanov, M. Schwabe, C. Räth, H. M. Thomas, and G. E. Morfill, "Wave turbulence observed in an auto-oscillating complex (dusty) plasma," *EPL (Europhysics Letters)*, vol. 110, p. 35001, may 2015.

[23] H. Rothermel, T. Hagl, G. E. Morfill, M. H. Thoma, and H. M. Thomas, "Gravity compensation in complex plasmas by application of a temperature gradient," *Phys. Rev. Lett.*, vol. 89, p. 175001, Oct. 2002.

[24] A. P. Nefedov, G. E. Morfill, V. E. Fortov, H. M. Thomas, H. Rothermel, T. Hagl, A. V. Ivlev, M. Zuzic, B. A. Klumov, A. M. Lipaev, V. I. Molotkov, O. F. Petrov, Y. P. Gidzenko, S. K. Krikalev, W. Shepherd, A. I. Ivanov, M. Roth, H. Binnenbruck, J. A. Goree, and Y. P. Semenov, "PKE-Nefedov: plasma crystal experiments on the International Space Station," *New J. Phys.*, vol. 5, pp. 33–33, apr 2003.

[25] H. M. Thomas, G. E. Morfill, V. E. Fortov, A. V. Ivlev, V. I. Molotkov, A. M. Lipaev, T. Hagl, H. Rothermel, S. A. Khrapak, R. K. Suetterlin, M. Rubin-Zuzic, O. F. Petrov, V. I. Tokarev, and S. K. Krikalev, "Complex plasma laboratory PK-3 Plus on the International Space Station," *New J. Phys.*, vol. 10, p. 033036, mar 2008.

[26] M. Y. Pustylnik, M. A. Fink, V. Nosenko, T. Antonova, T. Hagl, H. M. Thomas, A. V. Zobnin, A. M. Lipaev, A. D. Usachev, V. I. Molotkov, O. F. Petrov, V. E. Fortov, C. Rau, C. Deysenroth, S. Albrecht, M. Kretschmer, M. H. Thoma, G. E. Morfill, R. Seurig, A. Stettner, V. A. Alyamovskaya, A. Orr, E. Kufner, E. G. Lavrenko, G. I. Padalka, E. O. Serova, A. M. Samokutyayev, and S. Christoforetti, "Plasmakristall-4: New complex (dusty) plasma laboratory on board the International Space Station," *Rev. Sci. Instrum.*, vol. 87, no. 9, p. 093505, 2016.

[27] R. J. Heidemann, L. Couëdel, S. K. Zhdanov, K. R. Sütterlin, M. Schwabe, H. M. Thomas, A. V. Ivlev, T. Hagl, G. E. Morfill, V. E. Fortov, V. I. Molotkov, O. F. Petrov, A. I. Lipaev, V. Tokarev, T. Reiter, and P. Vinogradov, "Comprehensive experimental study of heartbeat oscillations observed under microgravity conditions in the PK-3 Plus laboratory on board the International Space Station," *Phys. Plasmas*, vol. 18, no. 5, p. 053701, 2011.

[28] A. V. Zobnin, A. D. Usachev, A. M. Lipaev, O. F. Petrov, V. E. Fortov, M. Y. Pustylnik, H. M. Thomas, M. A. Fink, M. H. Thoma, and G. I. Padalka, "Transverse ionization instability of the elongated dust cloud in the gas discharge uniform positive column under microgravity conditions," *J. Phys. Conf. Ser.*, vol. 774, p. 012174, nov 2016. XXXI International Conference on Equations of State for Matter (ELBRUS 2016) 1–6 March 2016, Elbrus, Russia.

[29] J. E. Allen, "Probe theory - the orbital motion approach," *Phys. Scr.*, vol. 45, no. 5, p. 497, 1992.

[30] J. E. Allen, B. M. Annaratone, and U. de Angelis, "On the orbital motion limited theory for a small body at floating potential in a maxwellian plasma," *J. Plasma Phys.*, vol. 63, pp. 299–309, May 2000.

[31] S. A. Khrapak, S. V. Ratynskaia, A. V. Zobnin, A. D. Usachev, V. V. Yaroshenko, M. H. Thoma, M. Kretschmer, H. Höfner, G. E. Morfill, O. F. Petrov, and V. E. Fortov, "Particle charge in the bulk of gas discharges," *Phys. Rev. E*, vol. 72, p. 016406, July 2005.

[32] L. G. D'yachkov, A. G. Khrapak, S. A. Khrapak, and G. E. Morfill, "Model of grain charging in collisional plasmas accounting for collisionless layer," *Phys. Plasmas*, vol. 14, p. 042102, Apr. 2007.

[33] A. V. Zobnin, A. D. Usachev, O. F. Petrov, and V. E. Fortov, "Ion current on a small spherical attractive probe in a weakly ionized plasma with ion-neutral collisions (kinetic approach)," *Phys. Plasmas*, vol. 15, no. 4, p. 043705, 2008.

[34] S. A. Khrapak and G. E. Morfill, "An interpolation formula for the ion flux to a small particle in collisional plasmas," *Phys. Plasmas*, vol. 15, p. 114503, Nov. 2008.

[35] A. V. Zobnin, A. P. Nefedov, V. A. Sinel'shchikov, and V. E. Fortov, "On the charge of dust particles in a low-pressure gas discharge plasma," *J. Exp. Theor. Phys.*, vol. 91, pp. 483–487, Sept. 2000.

[36] M. Lampe, R. Goswami, Z. Sternovsky, S. Robertson, V. Gavrishchaka, G. Ganguli, and G. Joyce, "Trapped ion effect on shielding, current flow, and charging of a small object in a plasma," *Phys. Plasmas*, vol. 10, pp. 1500–1513, May 2003.

[37] I. H. Hutchinson and L. Patacchini, "Computation of the effect of neutral collisions on ion current to a floating sphere in a stationary plasma," *Phys. Plasmas*, vol. 14, p. 013505, Jan. 2007.

[38] I. L. Semenov, A. G. Zagorodny, and I. V. Krivtsun, "A study of dust grain screening in a weakly ionized plasma based on the numerical solution of the Vlasov-Bhatnagar-Gross-Krook kinetic equations," *Phys. Plasmas*, vol. 18, p. 103707, Oct. 2011.

[39] I. L. Semenov, A. G. Zagorodny, and I. V. Krivtsun, "On the effect of ion-neutral collisions on dust grain screening in a low-pressure gas discharge plasma," *Phys. Plasmas*, vol. 19, p. 043703, Apr. 2012.

[40] P. S. Epstein, "On the resistance experienced by spheres in their motion through gases," *Phys. Rev.*, vol. 23, pp. 710–733, Jun 1924.

[41] L. Talbot, R. K. Cheng, R. W. Schefer, and D. R. Willis, "Thermophoresis of particles in a heated boundary layer," *J. Fluid Mech.*, vol. 101, no. 4, pp. 737–758, 1980.

[42] S. A. Khrapak, A. V. Ivlev, G. E. Morfill, and H. M. Thomas, "Ion drag force in complex plasmas," *Phys. Rev. E*, vol. 66, p. 046414, Oct 2002.

[43] S. A. Khrapak, A. V. Ivlev, G. E. Morfill, and S. K. Zhdanov, "Scattering in the attractive Yukawa potential in the limit of strong interaction," *Phys. Rev. Lett.*, vol. 90, p. 225002, June 2003.

[44] S. A. Khrapak, A. V. Ivlev, S. K. Zhdanov, and G. E. Morfill, "Hybrid approach to the ion drag force," *Phys. Plasmas*, vol. 12, p. 042308, Apr. 2005.

[45] I. L. Semenov, S. A. Khrapak, and H. M. Thomas, "Momentum transfer cross-section for ion scattering on dust particles," *Phys. Plasmas*, vol. 24, no. 3, p. 033710, 2017.

[46] S. A. Khrapak, "Accurate momentum transfer cross section for the attractive Yukawa potential," *Phys. Plasmas*, vol. 21, p. 044506, Apr. 2014.

[47] L. Patacchini and I. H. Hutchinson, "Fully self-consistent ion-drag-force calculations for dust in collisional plasmas with an external electric field," *Phys. Rev. Lett.*, vol. 101, p. 025001, July 2008.

[48] I. H. Hutchinson and C. B. Haakonsen, "Collisional effects on nonlinear ion drag force for small grains," *Phys. Plasmas*, vol. 20, p. 083701, Aug. 2013.

[49] I. L. Semenov, A. G. Zagorodny, and I. V. Krivtsun, "Ion drag force on a dust grain in a weakly ionized collisional plasma," *Phys. Plasmas*, vol. 20, p. 013701, Jan. 2013.

[50] K. Dimoff and P. R. Smy, "Dust induced quenching of an afterglow plasma," *Phys. Lett. A*, vol. 32, no. 1, pp. 13–14, 1970.

[51] A. Bouchoule and L. Boufendi, "Particulate formation and dusty plasma behaviour in argon-silane rf discharge," *Plasma Sources Sci. Technol.*, vol. 2, p. 204, 1993.

[52] K. Tachibana, Y. Hayashi, T. Okuno, and T. Tatsuta, "Spectroscopic and probe measurements of structures in a parallel-plates RF discharge with particles," *Plasma Sources Sci. Technol.*, vol. 3, pp. 314–319, Aug. 1994.

[53] Y. P. Raizer, M. N. Shneider, and N. A. Yatsenko, *Radio-Frequency Capacitive Discharges*. CRC Press, 1995.

[54] A. A. Fridman, L. Boufendi, T. Hbid, B. V. Potapkin, and A. Bouchoule, "Dusty plasma formation: Physics and critical phenomena. Theoretical approach," *J. Appl. Phys.*, vol. 79, p. 1303, 1996.

[55] Z. Shen and U. Kortshagen, "Experimental study of the influence of nanoparticle generation on the electrical characteristics of argon–silane capacitive radio-frequency plasmas," *Journal of Vacuum Science & Technology A: Vacuum, Surfaces, and Films*, vol. 20, pp. 153–159, Jan. 2002.

[56] S. Hong, J. Berndt, and J. Winter, "Growth precursors and dynamics of dust particle formation in the Ar/CH_4 and Ar/C_2H_2 plasmas," *Plasma Sources Sci. Technol.*, vol. 12, pp. 46–52, Dec. 2002.

[57] M. Sorokin, *Dust particle formation in silane plasmas*. phdthesis, Technische Universiteit Eindhoven, Eindhoven, 2005.

[58] I. Denysenko, J. Berndt, E. Kovacevic, I. Stefanovic, V. Selenin, and J. Winter, "The response of a capacitively coupled discharge to the formation of dust particles: Experiments and modeling," *Phys. Plasmas*, vol. 13, p. 073507, July 2006.

[59] I. Stefanovic, E. Kovacevic, J. Berndt, and J. Winter, "H_α emission in the presence of dust in an Ar-C_2H_2 radio-frequency discharge," *New J. Phys.*, vol. 5, no. 1, p. 39, 2003.

[60] I. V. Schweigert, A. L. Alexandrov, D. A. Ariskin, F. M. Peeters, I. Stefanović, E. Kovačević, J. Berndt, and J. Winter, "Effect of transport of growing nanoparticles on capacitively coupled rf discharge dynamics," *Phys. Rev. E*, vol. 78, p. 026410, Aug 2008.

[61] C. Killer, G. Bandelow, K. Matyash, R. Schneider, and A. Melzer, "Observation of Ω mode electron heating in dusty argon radio frequency discharges," *Phys. Plasmas*, vol. 20, no. 8, p. 083704, 2013.

[62] E. Schüngel, S. Mohr, S. Iwashita, J. Schulze, and U. Czarnetzki, "The effect of dust on electron heating and dc self-bias in hydrogen diluted silane discharges," *J. Phys. D: Appl. Phys.*, vol. 46, no. 17, p. 175205, 2013.

[63] L. Boufendi, J. Gaudin, S. Huet, G. Viera, and M. Dudemaine, "Detection of particles of less than 5 nm in diameter formed in an argon–silane capacitively coupled radio-frequency discharge," *Appl. Phys. Lett.*, vol. 79, pp. 4301–4303, Dec. 2001.

[64] G. Wattieaux, A. Mezeghrane, and L. Boufendi, "Electrical time resolved metrology of dust particles growing in low pressure cold plasmas," *Phys. Plasmas*, vol. 18, p. 093701, Sept. 2011.

[65] M. Y. Pustylnik, I. L. Semenov, E. Zähringer, and H. M. Thomas, "Capacitively coupled rf discharge with a large amount of microparticles: Spatiotemporal emission pattern and microparticle arrangement," *Phys. Rev. E*, vol. 96, p. 033203, 2017.

[66] S. Hübner and A. Melzer, "Dust-induced modulation of the atomic emission in a dusty argon discharge," *Phys. Rev. Lett.*, vol. 102, p. 215001, May 2009.

[67] A. Melzer, S. Hübner, L. Lewerentz, K. Matyash, R. Schneider, and R. Ikkurthi, "Phase-resolved optical emission of dusty rf discharges: Experiment and simulation," *Phys. Rev. E*, vol. 83, Mar. 2011.

[68] C. Killer, T. Wegner, A. Melzer, and J. Meichsner, "Influence of dust particles on the bulk electron density in radio frequency plasmas measured by microwave interferometry," *Phys. Plasmas*, vol. 22, p. 123702, Dec. 2015.

[69] I. Stefanović, N. Sadeghi, and J. Winter, "The influence of C_2H_2 and dust formation on the time dependence of metastable argon density in pulsed plasmas," *J. Phys. D: Appl. Phys.*, vol. 43, p. 152003, Mar. 2010.

[70] H. T. Do, H. Kersten, and R. Hippler, "Interaction of injected dust particles with metastable neon atoms in a radio frequency plasma," *New J. Phys.*, vol. 10, p. 053010, May 2008.

[71] S. Mitic, M. Y. Pustylnik, and G. E. Morfill, "Spectroscopic evaluation of the effect of the microparticles on radiofrequency argon plasma," *New J. Phys.*, vol. 11, no. 8, p. 083020, 2009.

[72] D. N. Polyakov, V. V. Shumova, L. M. Vasilyak, and V. E. Fortov, "Study of glow discharge positive column with cloud of disperse particles," *Phys. Lett. A*, vol. 375, pp. 3300–3305, Aug. 2011.

[73] A. D. Usachev, A. V. Zobnin, A. V. Shonenkov, A. M. Lipaev, V. I. Molotkov, O. F. Petrov, V. E. Fortov, M. Y. Pustyl'nik, M. A. Fink, M. A. Thoma, H. M. Thomas, and G. I. Padalka, "Influence of dust particles on the neon spectral line intensities at the uniform positive column of dc discharge at the space apparatus "Plasma Kristall-4"," *J. Phys. Conf. Ser.*, vol. 946, p. 012143, Jan. 2018.

[74] A. D. Usachev, A. V. Zobnin, O. F. Petrov, V. E. Fortov, M. H. Thoma, M. Y. Pustylnik, M. A. Fink, and G. E. Morfill, "Elongated dust clouds in a uniform DC positive column of low pressure gas discharge," *Plasma Sources Sci. Technol.*, vol. 25, p. 035009, Apr. 2016.

[75] A. V. Zobnin, A. D. Usachev, O. F. Petrov, V. E. Fortov, M. H. Thoma, and M. A. Fink, "Two-dimensional positive column structure with dust cloud: Experiment and nonlocal kinetic simulation," *Phys. Plasmas*, vol. 25, p. 033702, Mar. 2018.

[76] A. Pikalev, V. Kobylin, and A. Semenov, "Spectral study of glow discharge with dusty structures," *IEEE Trans. Plasma Sci.*, vol. 46, no. 4, pp. 698–700, 2018.

[77] Y. P. Raizer, *Gas Discharge Physics*. Springer-Verlag Berlin Heidelberg, 1991.

[78] M. A. Lieberman and A. J. Lichtenberg, *Principles of Plasma Discharges and Materials Processing*. John Wiley & Sons, Inc., Jan. 2005.

[79] G. I. Sukhinin, A. V. Fedoseev, S. N. Antipov, O. F. Petrov, and V. E. Fortov, "Dust particle radial confinement in a dc glow discharge," *Phys. Rev. E*, vol. 87, p. 013101, Jan. 2013.

[80] G. I. Sukhinin, A. V. Fedoseev, M. V. Salnikov, S. N. Antipov, O. F. Petrov, and V. E. Fortov, "Influence of ion drag force on radial distribution of dust particles and void formation in a DC glow discharge," *EPL (Europhysics Letters)*, vol. 103, p. 35001, Aug. 2013.

[81] A. V. Fedoseev, G. I. Sukhinin, M. K. Dosbolayev, and T. S. Ramazanov, "Dust-void formation in a dc glow discharge," *Phys. Rev. E*, vol. 92, p. 023106, Aug. 2015.

[82] J. Schulze, A. Derzsi, K. Dittmann, T. Hemke, J. Meichsner, and Z. Donkó, "Ionization by drift and ambipolar electric fields in electronegative capacitive radio frequency plasmas," *Phys. Rev. Lett.*, vol. 107, p. 275001, Dec. 2011.

[83] T. Hemke, D. Eremin, T. Mussenbrock, A. Derzsi, Z. Donkó, K. Dittmann, J. Meichsner, and J. Schulze, "Ionization by bulk heating of electrons in capacitive radio frequency atmospheric pressure microplasmas," *Plasma Sources Sci. Technol.*, vol. 22, p. 015012, Dec. 2012.

[84] P. Belenguer, J. P. Blondeau, L. Boufendi, M. Toogood, A. Plain, A. Bouchoule, C. Laure, and J. P. Boeuf, "Numerical and experimental diagnostics of rf discharges in pure and dusty argon," *Phys. Rev. A*, vol. 46, pp. 7923–7933, Dec. 1992.

[85] J. P. Boeuf, "Characteristics of a dusty nonthermal plasma from a particle-in-cell Monte Carlo simulation," *Phys. Rev. A*, vol. 46, pp. 7910–7922, Dec 1992.

[86] G. I. Sukhinin and A. V. Fedoseev, "Influence of dust-particle concentration on gas-discharge plasma," *Phys. Rev. E*, vol. 81, p. 016402, Jan. 2010.

[87] D. N. Polyakov, V. V. Shumova, and L. M. Vasilyak, "Positive column of glow discharge with dust particles," *Surf. Eng. Appl. Electrochem.*, vol. 49, pp. 114–124, Mar. 2013.

[88] G. H. P. M. Swinkels, H. Kersten, H. Deutsch, and G. M. W. Kroesen, "Microcalorimetry of dust particles in a radio-frequency plasma," *J. Appl. Phys.*, vol. 88, pp. 1747–1755, Aug. 2000.

[89] F. Liu, K. J. Daun, D. R. Snelling, and G. J. Smallwood, "Heat conduction from a spherical nano-particle: status of modeling heat conduction in laser-induced incandescence," *Appl. Phys. B*, vol. 83, pp. 355–382, Apr. 2006.

[90] B. M. Smirnov, "Processes in plasma and gases involving clusters," *Physics-Uspekhi*, vol. 40, pp. 1117–1147, nov 1997.

[91] S. A. Khrapak and G. E. Morfill, "Grain surface temperature in noble gas discharges: Refined analytical model," *Phys. Plasmas*, vol. 13, p. 104506, Oct. 2006.

[92] J. Perrin, P. Molinas-Mata, and P. Belenguer, "Ion drag and plasma-induced thermophoresis on particles in radiofrequency glow discharges," *J. Phys. D: Appl. Phys.*, vol. 27, pp. 2499–2507, Dec. 1994.

[93] M. R. Akdim and W. J. Goedheer, "Modeling the effect of dust on the plasma parameters in a dusty argon discharge under microgravity," *Phys. Rev. E*, vol. 67, p. 066407, Jun 2003.

[94] M. R. Akdim and W. J. Goedheer, "Modeling of self-excited dust vortices in complex plasmas under microgravity," *Phys. Rev. E*, vol. 67, p. 056405, May 2003.

[95] V. Land and W. J. Goedheer, "The plasma inside a dust free void: hotter, denser, or both?," *New J. Phys.*, vol. 9, pp. 246–246, Aug. 2007.

[96] W. J. Goedheer and V. Land, "Simulation of dust voids in complex plasmas," *Plasma Phys. Controlled Fusion*, vol. 50, p. 124022, nov 2008.

[97] V. Land and W. J. Goedheer, "How to make large, void-free dust clusters in dusty plasma under micro-gravity," *New J. Phys.*, vol. 10, p. 123028, dec 2008.

[98] W. J. Goedheer, V. Land, and J. Venema, "Hydrodynamic and kinetic modelling of complex radio-frequency plasmas," *J. Phys. D: Appl. Phys.*, vol. 42, p. 194015, Sept. 2009.

[99] L. M. Vasilyak, D. N. Polyakov, and V. V. Shumova, "Glow discharge positive column with dust particles in neon," *Contrib. Plasma Phys.*, vol. 53, pp. 432–435, May 2013.

[100] D. N. Polyakov, V. V. Shumova, and L. M. Vasilyak, "On the mechanism of radial void sustenance of dense dusty plasmas," *Digest Journal of Nanomaterials and Biostructures*, vol. 9, no. 12, p. 1249, 2014.

[101] V. Sushkov, A.-P. Herrendorf, and R. Hippler, "Metastable argon atom density in complex argon/acetylene plasmas determined by means of optical absorption and emission spectroscopy," *J. Phys. D: Appl. Phys.*, vol. 49, p. 425201, sep 2016.

[102] J. L. Dorier, C. Hollenstein, and A. A. Howling, "Spatiotemporal powder formation and trapping in radio frequency silane plasmas using two-dimensional polarization-sensitive laser scattering," *Journal of Vacuum Science & Technology A*, vol. 13, no. 3, pp. 918–926, 1995.

[103] G. Praburam and J. Goree, "Experimental observation of very low-frequency macroscopic modes in a dusty plasma," *Phys. Plasmas*, vol. 3, no. 4, pp. 1212–1219, 1996.

[104] G. E. Morfill, H. M. Thomas, U. Konopka, H. Rothermel, M. Zuzic, A. Ivlev, and J. Goree, "Condensed plasmas under microgravity," *Phys. Rev. Lett.*, vol. 83, pp. 1598–1601, Aug 1999.

[105] V. V. Balabanov, L. M. Vasilyak, S. P. Vetchinin, A. P. Nefedov, D. N. Polyakov, and V. E. Fortov, "The effect of the gas temperature gradient on dust structures in a glow-discharge plasma," *J. Exp. Theor. Phys.*, vol. 92, pp. 86–92, Jan 2001.

[106] V. V. Shumova, D. N. Polyakov, and L. M. Vasilyak, "Boundary of the transition to hollow dust structures in a DC discharge in neon with microparticles," *Plasma Phys. Rep.*, vol. 45, pp. 285–288, mar 2019.

[107] C. Schmidt, O. Arp, and A. Piel, "Spatially extended void-free dusty plasmas in a laboratory radio-frequency discharge," *Phys. Plasmas*, vol. 18, no. 1, p. 013704, 2011.

[108] C. A. Knapek, U. Konopka, D. P. Mohr, P. Huber, A. M. Lipaev, and H. M. Thomas, ""Zyflex": Next generation plasma chamber for complex plasma research in space," *Review of Scientific Instruments*, vol. 92, no. 10, p. 103505, 2021.

[109] W. J. Goedheer, V. Land, and J. Venema, "Modelling of voids in complex radio frequency plasmas," *Contrib. Plasma Phys.*, vol. 49, no. 4-5, pp. 199–214, 2009.

[110] V. Land, L. S. Matthews, T. W. Hyde, and D. Bolser, "Fluid modeling of void closure in microgravity noble gas complex plasmas," *Phys. Rev. E*, vol. 81, no. 5, p. 056402, 2010.

[111] F. M. J. H. Van de Wetering, R. J. C. Brooimans, S. Nijdam, J. Beckers, and G. M. W. Kroesen, "Fast and interrupted expansion in cyclic void growth in dusty plasma," *J. Phys. D: Appl. Phys.*, vol. 48, no. 3, p. 035204, 2015.

[112] I. Stefanović, N. Sadeghi, J. Winter, and B. Sikimic, "Influence of nanoparticle formation on the time and the space resolved metastable density in argon-acetylene plasmas," *Plasma Sources Sci. Technol.*, vol. 26, no. 6, p. 065014, 2017.

[113] I. Pilch and F. Greiner, "Diagnostics of void expansion during cyclic growth and formation of layered nanoparticle clouds," *J. Appl. Phys.*, vol. 121, no. 11, p. 113302, 2017.

[114] M. Wolter, A. Melzer, O. Arp, M. Klindworth, and A. Piel, "Force measurements in dusty plasmas under microgravity by means of laser manipulation," *Phys. Plasmas*, vol. 14, no. 12, p. 123707, 2007.

[115] M. Kretschmer, S. A. Khrapak, S. K. Zhdanov, H. M. Thomas, G. E. Morfill, V. E. Fortov, A. M. Lipaev, V. I. Molotkov, A. I. Ivanov, and M. V. Turin, "Force field inside the void in complex plasmas under microgravity conditions," *Phys. Rev. E*, vol. 71, p. 056401, May 2005.

[116] E. Thomas, B. M. Annaratone, G. E. Morfill, and H. Rothermel, "Measurements of forces acting on suspended microparticles in the void region of a complex plasma," *Phys. Rev. E*, vol. 66, p. 016405, Jul 2002.

[117] B. Buttenschön, M. Himpel, and A. Melzer, "Spatially resolved three-dimensional particle dynamics in the void of dusty plasmas under microgravity using stereoscopy," *New J. Phys.*, vol. 13, p. 023042, feb 2011.

[118] M. Kretschmer, U. Konopka, S. K. Zhdanov, H. M. Thomas, G. E. Morfill, V. E. Fortov, V. I. Molotkov, A. M. Lipaev, and O. F. Petrov, "Particles inside the void of a complex plasma," *IEEE Trans. Plasma Sci.*, vol. 39, no. 11, pp. 2758–2759, 2011.

[119] J. Goree, G. E. Morfill, V. N. Tsytovich, and S. V. Vladimirov, "Theory of dust voids in plasmas," *Phys. Rev. E*, vol. 59, pp. 7055–7067, Jun 1999.

[120] V. N. Tsytovich, S. V. Vladimirov, G. E. Morfill, and J. Goree, "Theory of collision-dominated dust voids in plasmas," *Phys. Rev. E*, vol. 63, p. 056609, Apr 2001.

[121] V. N. Tsytovich, S. V. Vladimirov, and G. E. Morfill, "Theory of dust and dust-void structures in the presence of the ion diffusion," *Phys. Rev. E*, vol. 70, p. 066408, Dec 2004.

[122] G. Morfill and V. N. Tsytovich, "Ionization instability and dusty plasma structurization," *Plasma Phys. Rep.*, vol. 26, pp. 682–690, aug 2000.

[123] K. Avinash, A. Bhattacharjee, and S. Hu, "Nonlinear theory of void formation in colloidal plasmas," *Phys. Rev. Lett.*, vol. 90, p. 075001, Feb 2003.

[124] G. Gozadinos, A. V. Ivlev, and J. P. Boeuf, "A fluid model for colloidal plasmas under microgravity conditions," *New J. Phys.*, vol. 5, p. 32, Apr. 2003.

[125] D. Samsonov and J. Goree, "Instabilities in a dusty plasma with ion drag and ionization," *Phys. Rev. E*, vol. 59, no. 1, p. 1047, 1999.

[126] D. Samsonov and J. Goree, "Line ratio imaging of a gas discharge," *IEEE Trans. Plasma Sci.*, vol. 27, no. 1, pp. 76–77, 1999.

[127] M. Mikikian, S. Labidi, E. von Wahl, J.-F. Lagrange, T. Lecas, V. Massereau-Guilbaud, I. Géraud-Grenier, E. Kovacevic, J. Berndt, H. Kersten, and T. Gibert, "Plasma response to nanoparticle growth," *AIP Conference Proceedings*, vol. 1925, no. 1, p. 020019, 2018.

[128] M. Schulze, A. von Keudell, and P. Awakowicz, "Characterization of a rotating nanoparticle cloud in an inductively coupled plasma," *Plasma Sources Sci. Technol.*, vol. 15, pp. 556–563, June 2006.

[129] M. Klindworth, O. Arp, and A. Piel, "Langmuir probe system for dusty plasmas under microgravity," *Rev. Sci. Instrum.*, vol. 78, p. 033502, Mar. 2007.

[130] H. Tawidian, H. El Hainouni, T. Gibert, M. Mikikian, T. Lecas, and L. Boufendi, "Void investigations using laser diagnostics," *AIP Conference Proceedings*, vol. 1397, no. 1, pp. 371–372, 2011. DUSTY/COMPLEX PLASMAS: BASIC AND INTERDISCIPLINARY RESEARCH: Sixth International Conference on the Physics of Dusty Plasmas. 16–20 May 2011, Garmisch-Partenkirchen (Germany).

[131] H. Tawidian, F. Diop, T. Lecas, T. Gibert, and M. Mikikian, "Void behavior and profile using laser induced fluorescence," in *40th EPS Conference on Plasma Physics*, (Espoo, Finland), p. P1.304, 2013.

[132] J. Goree, R. Quinn, G. Morfill, H. Thomas, T. Hagl, U. Konopka, H. Rothermel, , and M. Zuzic, "Plasma dust crystallization," in *Proceedings of the 4th Microgravity Fluid Physics and Transport Phenomena Conference*, (Cleveland), pp. 105–106, 1998.

[133] S. K. Zhdanov, M. Schwabe, R. Heidemann, R. Sütterlin, H. M. Thomas, M. Rubin-Zuzic, H. Rothermel, T. Hagl, A. V. Ivlev, G. E. Morfill, V. I. Molotkov, A. M. Lipaev, O. F. Petrov, V. E. Fortov, and T. Reiter, "Auto-oscillations in complex plasmas," *New J. Phys.*, vol. 12, p. 043006, apr 2010.

[134] M. Mikikian and L. Boufendi, "Experimental investigations of void dynamics in a dusty discharge," *Phys. Plasmas*, vol. 11, no. 8, pp. 3733–3737, 2004.

[135] M. Mikikian, L. Couëdel, M. Cavarroc, Y. Tessier, and L. Boufendi, "Self-excited void instability in dusty plasmas: plasma and dust cloud dynamics during the heartbeat instability," *New J. Phys.*, vol. 9, no. 8, p. 268, 2007.

[136] M. Mikikian, M. Cavarroc, L. Couëdel, Y. Tessier, and L. Boufendi, "Mixed-mode oscillations in complex-plasma instabilities," *Phys. Rev. Lett.*, vol. 100, p. 225005, Jun 2008.

[137] M. Mikikian, L. Couëdel, M. Cavarroc, Y. Tessier, and L. Boufendi, "Threshold phenomena in a throbbing complex plasma," *Phys. Rev. Lett.*, vol. 105, p. 075002, Aug 2010.

[138] M. Y. Pustylnik, A. V. Ivlev, N. Sadeghi, R. Heidemann, S. Mitic, H. M. Thomas, and G. E. Morfill, "On the heterogeneous character of the heartbeat instability in complex (dusty) plasmas," *Phys. Plasmas*, vol. 19, no. 10, p. 103701, 2012.

[139] R. L. Merlino, "25 years of dust acoustic waves," *J. Plasma Phys.*, vol. 80, pp. 773–786, June 2014.

[140] M. Mikikian, M. Cavarroc, L. Couëdel, and L. Boufendi, "Low frequency instabilities during dust particle growth in a radio-frequency plasma," *Phys. Plasmas*, vol. 13, no. 9, p. 092103, 2006.

[141] M. Mikikian, H. Tawidian, and T. Lecas, "Merging and splitting of plasma spheroids in a dusty plasma," *Phys. Rev. Lett.*, vol. 109, p. 245007, Dec 2012.

[142] M. Mikikian, L. Couedel, Y. Tessier, and L. Boufendi, "Carousel instability in a capacitively coupled rf dusty plasma," *IEEE Trans. Plasma Sci.*, vol. 39, no. 11, pp. 2748–2749, 2011.

[143] M. Mikikian, M. Cavarroc, N. Chaumeix, and L. Boufendi, "Instabilities in a dense cloud of grown dust particles," in *31st EPS Conference on Plasma Physics London, 28 June - 2 July 2004*, vol. 28G of *ECA*, (London), pp. O–2.13, 2004.

[144] M. Schwabe, S. Zhdanov, and C. Räth, "Turbulence in an auto-oscillating complex plasma," *IEEE Trans. Plasma Sci.*, vol. 46, no. 4, pp. 684–687, 2018.

[145] S. V. Vladimirov, V. N. Tsytovich, and G. E. Morfill, "Stability of dust voids," *Phys. Plasmas*, vol. 12, no. 5, p. 052117, 2005.

[146] M. Schwabe, L.-J. Hou, S. Zhdanov, A. V. Ivlev, H. M. Thomas, and G. E. Morfill, "Convection in a dusty radio-frequency plasma under the influence of a thermal gradient," *New J. Phys.*, vol. 13, p. 083034, aug 2011.

[147] V. Ochkin, *Spectroscopy of Low Temperature Plasma*. WILEY-VCH Verlag GmbH & Co. KGaA, 2009.

[148] S. Hübner, N. Sadeghi, E. A. D. Carbone, and J. J. A. M. van der Mullen, "Density of atoms in Ar*($3p^5 4s$) states and gas temperatures in an argon surfatron plasma measured by tunable laser spectroscopy," *J. Appl. Phys.*, vol. 113, no. 14, p. 143306, 2013.

[149] J. Kaupe, D. Coenen, and S. Mitic, "Phase-resolved optical emission spectroscopy of a transient plasma created by a low-pressure dielectric barrier discharge jet," *Plasma Sources Sci. Technol.*, vol. 27, p. 105003, oct 2018.

[150] A. D. Khakhaev, V. I. Kobylin, L. A. Luizova, and A. I. Scherbina, "Measuring the metastable atom density in plasma crystal by the method of selective optical exitation," in *Proceedings of the XVI International Conference on Gas Discharges and their Applications*, vol. 2, (Xi'an, China), pp. 645–648, September 11–15 2006.

[151] R. S. Marshall and P. M. Bellan, "Laser-induced fluorescence measurement of very slow neutral flows in a dusty plasma experiment," *Rev. Sci. Instrum.*, vol. 91, no. 6, p. 063504, 2020.

[152] C. Arnas, M. Mikikian, G. Bachet, and F. Doveil, "Sheath modification in the presence of dust particles," *Phys. Plasmas*, vol. 7, no. 11, pp. 4418–4422, 2000.

[153] K. Wood, R. Fisher, and E. Thomas, "Laser-induced fluorescence measurements of ion densities and flows near a dusty plasma," in *54th Annual Meeting of the APS Division of Plasma Physics, October 29-November 2, 2012*, (Providence, USA), p. NP8.016, American Physical Society, 2012.

[154] Z. J. Taylor, R. Gurka, G. A. Kopp, and A. Liberzon, "Long-duration time-resolved PIV to study unsteady aerodynamics," *IEEE Trans. Instrum. Meas.*, vol. 59, pp. 3262–3269, dec 2010.

[155] "OpenPIV C++ with Qt frontend." Source code: https://github.com/OpenPIV/openpiv-c--qt. Last modification: 24 May 2020, git hash: 73792ce4d31ba82b917c58532932c74f4c95f940.

[156] B. Liu, J. Goree, V. Nosenko, and L. Boufendi, "Radiation pressure and gas drag forces on a melamine-formaldehyde microsphere in a dusty plasma," *Phys. Plasmas*, vol. 10, no. 1, pp. 9–20, 2003.

[157] O. P. Bochkova and E. A. Sukiasyan, "Population of resonant levels in argon by ine lastic collision between slow electrons and metastable atoms," *J. Appl. Spectrosc.*, vol. 23, pp. 1317–1321, oct 1975.

[158] I. I. Sobel'man, *Introduction to the Theory of Atomic Spectra*. Pergamon, 1972.

[159] W. Demtröder, *Laser Spectroscopy: Basic Concepts and Instrumentation*. Berlin, Heidelberg, New York: Springer-Verlag, 1982.

[160] J. R. Nestor, "Optogalvanic spectra of neon and argon in glow discharge lamps," *Appl. Opt.*, vol. 21, pp. 4154–4157, Nov 1982.

[161] D. E. Murnick, R. B. Robinson, D. Stoneback, M. J. Colgan, and F. A. Moscatelli, "Optogalvanic signals from argon metastables in a rf glow discharge," *Appl. Phys. Lett.*, vol. 54, no. 9, pp. 792–794, 1989.

[162] J. B. Boffard, G. A. Piech, M. F. Gehrke, L. W. Anderson, and C. C. Lin, "Measurement of electron-impact excitation cross sections out of metastable levels of argon and comparison with ground-state excitation," *Phys. Rev. A*, vol. 59, no. 4, pp. 2749–2763, 1999.

[163] A. A. Mityureva and V. V. Smirnov, "Electronic excitation of Ar atoms to metastable states and from metastable to higher states," *Opt. Spectrosc.*, vol. 97, pp. 508–521, oct 2004.

Acknowledgments

I thank my colleagues from the Complex Plasma group for useful discussions and support in so many things. They do their best to keep the working atmosphere comfortable and motivating, against all the odds. First of all, I am especially grateful to my supervisor Mikhail Pustylnik for his enthusiasm, involvement in the project and availability. I also thank Christoph Räth, my supervisor from LMU and Hubertus M. Thomas, the leader of the Complex Plasma group. The experiments would not be possible without engineers: Tanja Hagl, Paul Jauffrion, Sebastian Möst and, of course, Claudius George.

I would like to thank Igor Semenov for the model of dim and bright void and useful discussions. The collaboration with him was really fruitful.

The final version of the dissertation was improved thanks to comments of Alexei Ivlev, the second referee. His careful review helped to present the results more clearly.

I also thank my teachers and colleagues from Petrozavodsk State University, where I started my academic live. Especially, I would like to acknowledge people with whom together I began the research of complex plasmas: Lidia Luizova, Aleksandr Scherbina, Vladimir Kobylin, Aleksandr Semenov, Aleksandr Pergament, Valeri Sysun and Anatoly Khakhaev.

Finally, I acknowledge the financial support from Deutscher Akademischer Austauschdienst e.V. (DAAD) with funds from Deutsches Zentrum für Luft- und Raumfahrt e.V. (DLR). The PK-3 Plus chamber was funded by the space agency of DLR with funds from the federal ministry for economy and technology according to a resolution of the Deutscher Bundestag under grants No. 50WP0203, 50WM1203.

Related publications

The results presented in this cumulative thesis were published in following papers, which are enclosed in the thesis:

1. A. Pikalev, M. Pustylnik, C. Räth, and H. Thomas, "Measurement of gas temperatures in dust-free and dusty argon discharges," *J. Phys. D: Appl. Phys.*, vol. 53, p. 075203, 2020.
   The enclosed version is the Accepted Manuscript version of the article. The Version of Record is available online at https://doi.org/10.1088/1361-6463/ab59aa .

2. A. Pikalev, I. Semenov, M. Pustylnik, C. Räth, and H. Thomas, "Dim and bright void regimes in capacitively-coupled RF complex plasmas," *Plasma Sources Sci. Technol.*, vol. 30, p. 035014, 2021.
   The enclosed version is the Accepted Manuscript version of the article. The Version of Record is available online at https://doi.org/10.1088/1361-6595/abe0a2 .

3. A. Pikalev, M. Pustylnik, C. Räth and H. Thomas, "Heartbeat instability as auto-oscillation between dim and bright void regimes", *Phys. Rev. E*, vol. 104, p. 045212, 2021. DOI: https://doi.org/10.1103/PhysRevE.104.045212 .

These results are also included into a broader review of microparticle-plasma interactions (not enclosed in the thesis), which we use partially for the introduction:

4. M. Y. Pustylnik, A. A. Pikalev, A. V. Zobnin, I. L. Semenov, H. M. Thomas, O. F. Petrov "Physical aspects of dust-plasma interactions", *Contributions to Plasma Physics*, vol. 61, p. e202100126, 2021. DOI: https://doi.org/10.1002/ctpp.202100126

Measurement of gas temperatures in dust-free and dusty argon discharges

Measurement of gas temperatures in dust-free and dusty argon discharges

A Pikalev, M Pustylnik, C Räth and H Thomas

Deutsches Zentrum für Luft- und Raumfahrt e. V., Institut für Materialphysik im Weltraum, 82234 Weßling, Germany

E-mail: Aleksandr.Pikalev@dlr.de

Abstract.

Gas temperatures in an argon low-power capacitively-coupled rf discharge were measured by means of tunable diode laser absorption spectroscopy on $1s_5$ metastable states. It was shown that the uncertainty of the measurements in dust-free plasma could be minimized to ± 1 K. In the presence of dust, due to instabilities in the dust subsystem (e.g. dust density waves), the uncertainty of the temperature measurements increased several times. Nevertheless, an evidence of the gas temperature increase in the presence of dust was detected. This result suggests that the microparticle suspensions, immersed in the low-pressure plasmas, significantly modify the temperature fields of the neutral gas.

Keywords: dusty plasma, laser absorption spectroscopy, atomic temperature, rf discharge

Submitted to: *J. Phys. D: Appl. Phys.*

1. Introduction

Complex or dusty plasma is a medium containing ionized gas and micron-sized solid particles. It is used in basic research as a model system for the particle-resolved studies of generic condensed matter phenomena [1, 2]. On ground, 3D complex plasmas are disturbed by gravity. That is why, microgravity experiments are so valued.

However, in microgravity other disturbing effects become important. For example, if there is a temperature gradient in a background gas, a microparticle experiences the thermophoretic force. This force is proportional to and directed opposite to the temperature gradient. For example, temperature gradients ~ 1 K/cm cause the thermophoretic force comparable with an axial electric force in a dc glow discharge positive column, which is used for the manipulation of microparticles in PK-4 setup [3]. Also, the force can play a role in a void (a dust-free region inside a dust cloud [4]) formation [5], and can be used to compensate gravity in ground experiments [6].

A related effect caused by the temperature gradient is the thermal creep — the gas flow appearing near a nonuniformly heated surface. The creep is induced in the direction of the temperature gradient along the surface. This phenomenon can produce vortices in microparticle suspensions [7].

It is well known that microparticle suspensions can locally and non-locally modify plasma parameters (densities of electrons, ions and excited atoms, electron temperature and electric fields [8–13]), whose spatial distributions determine the distribution of heat sources in a discharge. In addition to that, the microparticles themselves represent the local heat sources since their surfaces absorb the electron and ion flows [14]. The microparticles can, therefore, modify the gas temperature distribution and thermophoretic forces. This issue is rarely taken into account in planning and interpretation of microgravity complex plasma experiments.

In the work by Rothermel et al. [6] the thermophoresis could compensate gravity for a relatively small amount of particles, but with the increase of the amount of microparticles, the suspension started loosing symmetry with respect to the midplane of the discharge chamber. The authors suggested that the microparticles modified the temperature gradient in the plasma. The effect could also be explained by a modification of the thermophoretic force in a dense microparticle suspension in comparison with the force for a single particle [15].

Calculations for a dc glow discharge in neon with pressure of 0.9 torr and a current of 3 mA showed that microparticle suspensions increase the gas temperature in the tube center by ≈ 2 K [16]. This estimation was conducted for the microparticle suspensions with radius of 8.25 mm (half of the tube radius) and densities of $1 \cdot 10^{11} - 4 \cdot 10^{11}\,\mathrm{m}^{-3}$. The grain radius was $2.55\,\mu$m. The effect was explained by a growth of the axial electric field in the presence of the microparticles. An attempt to detect this phenomenon by means of Fabry-Perrot interferometry of the discharge emission [17] was not successful due to insufficient accuracy of the method.

Gas heating in a rf discharge was discussed in [18]. It was suggested that the

microparticles increase the gas heating, which could lead to significant thermophoretic forces. The gas temperature distribution in a rf discharge was simulated in [19]. According to the simulation the microparticles increased the gas temperature, but the effect was quite small.

Experiments [12] showed that the growth of dust particles in an argon-acetylene mixture was accompanied by a drastic (about 50 K) drop of the argon gas temperature. Reference [10] reported the dust-induced growth of the gas temperature in the discharge center in argon and argon-acetylene mixtures. The achieved temperature gradient should have led to the thermophoretic forces comparable to electrostatic forces.

All this shows that the issue of the microparticle-induced modification of the temperature field in discharges is controversial, potentially important for the complex plasmas, and, therefore, requires careful investigation. In the present work, we propose and discuss a rigorous approach to the tunable diode laser absorption spectroscopy (TDLAS) measurements of gas temperatures in argon discharges. Since small ($\sim$ 0.1 K/cm) temperature gradients may play a role in complex plasmas, we took great care of characterizing the uncertainties. Uncertainties of the temperature measurements are rarely reported in literature although TDLAS is a common method of temperature measurement [20]. The most accurate measurements were in [8] (inaccuracy 2-5 K) and [10, 21] (inaccuracy about 10 K). After minimizing the uncertainties, we compared the measurements in dust-free and dusty discharges.

2. Experimental setup

The experiments were conducted in the ground-based PK-3 Plus chamber [22], which was supplemented with a TDLAS system (see figure 1). The plasma was produced by means of a capacitively-coupled rf discharge. Two electrodes were driven in a push-pull mode by a sinusoidal signal with the frequency of 13.56 MHz and the discharge power of 0.2 W. Argon fed to the chamber with 3 sccm gas flow was used as a working gas. The pressure was about 37 Pa. We used melamine formaldehyde spheres with the diameter of $1.95 \pm 0.05\,\mu$m as microparticles.

The PK-3 Plus setup allowed us to control the temperature gradient between the electrodes. The bottom electrode could be heated by an electric heater and the top electrode was cooled by a fan. We measured temperatures on the outer surfaces of the two chamber flanges with Tinytag Explorer data logger. Without heating, the temperature difference between the flanges was < 0.5 K.

To measure temperatures at different heights, the beam from the Toptica DL Pro laser was divided into two beams which passed through the rf discharge. The width of the laser spectral line was less than 1 MHz, which is much smaller than the width of the Doppler-broadened absorption profile. The laser scanned the wavelength over a range around the 772.38 nm argon spectral line with the frequency of 10 Hz. A small fraction of the laser light passed though a Fabry-Perot interferometer to control the wavelength scanning speed. Two absorption profiles as well as the interferometer

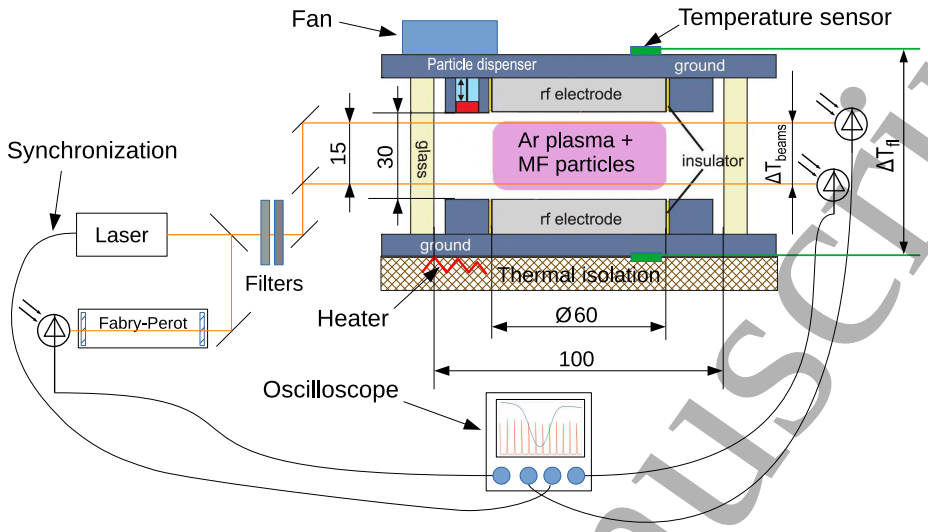

Figure 1. Scheme of the experimental setup. The heart of the experiment is the PK-3 Plus chamber [22]. The bottom flange of the chamber can be heated to control a temperature gradient between the electrodes. The laser light is divided into two beams to measure the temperatures at two different heights. A fraction of the laser light passes through a Fabry-Perrot interferometer to control the wavelength scanning speed.

fringes were detected with photodiodes. Signals from all photosensors were recorded with the LeCroy wavePro 725Zi oscilloscope.

To prevent the saturation broadening, the laser beams were attenuated with neutral density filters to the level about 1.5 μW. At these laser light powers, the measured absorption line width exhibited no power dependence. For comparison, the optogalvanic excitation of the heartbeat instability was observed with laser powers higher than 1 mW [23].

In principle, the absorption of the laser light by the microparticles could heat up their surfaces. If a microparticle absorbed the entire incident laser light, it would receive $4.5 \cdot 10^{-6}\,\mu$W. Thermal flow density from the microparticle surface due to the heat exchange with the gas can be calculated as $J_{gas} = \frac{1}{4} N_0 \langle v \rangle \alpha k_B \Delta T_{sg}$ [14], where N_0 — the gas number density, $\langle v \rangle$ — the average speed of the Ar atoms, $\alpha = 0.86$ — the accommodation coefficient, k_B — the Boltzmann constant, ΔT_{sg} — the difference between the surface and the gas temperatures. If we consider thermalization of the gas atoms on the surface as the only cooling mechanism, the heating by the laser will increase the microparticle surface temperature by less than 0.1 K.

Therefore, we can assume that the temperature measurements we performed were practically non-invasive.

3. Theory

The TDLAS method is based on the Beer-Lambert law [24]:

$$I(\nu) = I_0(\nu)\exp(-k(\nu)l). \tag{1}$$

Here, $I_0(\nu)$ is the incoming laser intensity, $I(\nu)$ — the intensity after the absorption, l is the length of absorbing medium and $k(\nu)$ — the absorption coefficient averaged along l. In our conditions, the absorption line had a Doppler shape:

$$k(\nu) \sim \exp\left(-\frac{Mc^2}{2k_BT}\frac{(\nu-\nu_0)^2}{\nu_0^2}\right). \tag{2}$$

Here, M is the atomic mass, c — the speed of light, k_B — the Boltzmann constant, T — the gas temperature, and ν_0 — the spectral line center. It is assumed that the absorbing species have homogeneous temperature along the laser beam.

The absorption strength characterizes the metastable density:

$$\int_0^\infty k(\nu)\,d\nu = h\nu_0 B_{ik}\langle N_i\rangle. \tag{3}$$

Here, h is the Plank constant, B_{ik} — the Einstein coefficient, $\langle N_i\rangle$ — averaged density of the absorbing atoms.

In every experiment, we measured two frequency-dependent intensities $I_{abs}(\nu)$ and $I_{laser}(\nu)$ and two constant intensities I_{plasma} and I_{dark}. By $I_{abs}(\nu)$, we mean the intensity of the laser light passed through the plasma. This intensity contains the absorption profile. By $I_{laser}(\nu)$, we mean the laser intensity passed through the discharge chamber without plasma. I_{plasma} is the plasma emission seen by the photodiode and I_{dark} is its dark current. Since $I(\nu) = I_{abs}(\nu) - I_{plasma}$ and $I_0(\nu) = I_{laser}(\nu) - I_{dark}$, from equation (1), we obtain [21, 25]:

$$k(\nu)l = \ln\left(\frac{I_{laser}(\nu) - I_{dark}}{I_{abs}(\nu) - I_{plasma}}\right). \tag{4}$$

4. Data processing

4.1. Numerical procedures

We aimed at measuring the temperature by fitting the experimentally measured profile from equation (4) with a Doppler profile from equation (2).

We have encountered two difficulties. First, the $I_{laser}(\nu)$ and $I_{abs}(\nu)$ exhibited a small random phase shift with respect to each other (most likely) due to the weak interference of the laser light on the chamber walls. Second, in the presence of microparticles, the laser light experienced broadband extinction resulting in the reduction of $I_{abs}(\nu)$ at unchanged $I_{laser}(\nu)$. Both effects are illustrated in figure 2.

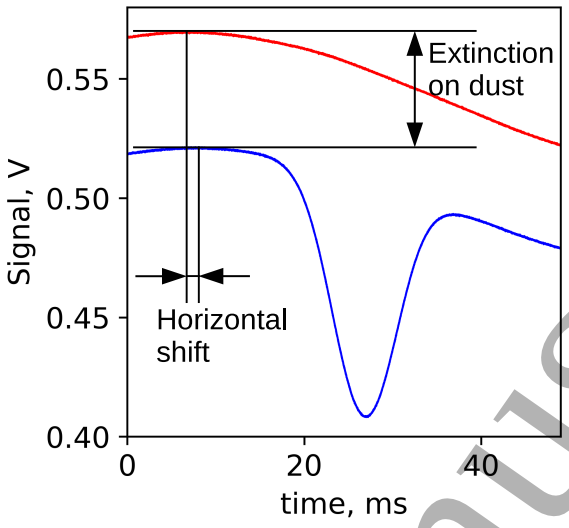

Figure 2. An example of absorption and laser intensity curves. The plasma emission and the dark signal are subtracted. The horizontal shift is 94.8 MHz. The microparticles extinguished 8.5 % of the laser radiation.

To address both issues, we worked out a numerical procedure which matched $I(\nu)$ and $I_0(\nu)$ by minimizing the discrepancy $\Delta(\delta\nu, s)$ between points at the frequencies far from the spectral line center ν_0. The function $\Delta(\delta\nu, s)$ was defined as

$$\Delta(\delta\nu) = \left\langle \left(I(\nu) - sI_0(\nu - \delta\nu)\right)^2 + w|\delta\nu| \right\rangle_{|\nu-\nu_0|\gg\Delta\nu}, \tag{5}$$

where $I(\nu) = I_{abs}(\nu) - I_{plasma}$, $I_0(\nu) = I_{laser}(\nu) - I_{dark}$, s characterizes the laser light extinction by the microparticles, $\delta\nu$ — the phase shift between $I_{laser}(\nu)$ and $I_{abs}(\nu)$, w — arbitrary constant, $\Delta\nu$ is the spectral line width. We minimized this function using the golden-section method [26] calculating $s = \langle I(\nu)/I_0(\nu - \delta\nu)\rangle_{|\nu-\nu_0|\gg\Delta\nu}$ at every iteration. We introduced the term $w|\delta\nu|$ to prevent unphysically large $\delta\nu$ in case of a very flat dependence of $I(\nu) - sI_0(\nu - \delta\nu)$ on $\delta\nu$, We took $w = 5 \cdot 10^{-16}\,\mathrm{V}^2/\mathrm{Hz}$ to make the term $w|\delta\nu|$ comparable with the noise for large shifts ($\sim 10^8$ Hz).

An example of the absorption fitted using the matching procedure described above is presented in figure 3. Discrepancy between the measurement and the fit is $< 1\%$.

Alternatively, the temperature could be found using the polynomial representation of $I_0(\nu)$ so that:

$$I(\nu) = (a_0 + a_1\nu + \ldots + a_n\nu^n) \times \\ \times \exp\left(-A \cdot \exp\left(-b(\nu - \nu_0)^2\right)\right), \tag{6}$$

where A defines the absorption strength. The temperature can be found from the coefficient b (see equation (2)).

This method, in principle, allows to avoid the above mentioned issues. To use this fit, we have to choose a proper n. Linear representation of $I_0(\nu)$ was used in [12], $n = 2$

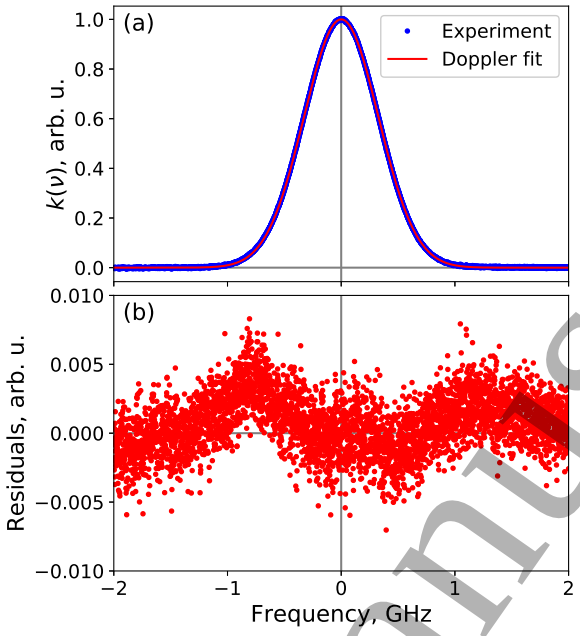

Figure 3. A normalized profile obtained from the curves shown in figure 2 by the matching procedure. (a) — the experimental points with the Doppler fit. (b) — the fit residuals.

was used in [8], but in our case the laser intensity curves had more complicated shapes. Hence, we had to use a higher polynomial degree.

4.2. Tests on artificial data

We tested the data processing methods on artificially generated data. For the test, we used $T = 305$ K and absorption strength $A = 0.1$ in the spectral line center. We generated $I_{abs}(\nu)$ based on $I_{laser}(\nu)$ curves taken from real experiments using the following model:

$$I_{abs}(\nu) = s \cdot (I_{laser}(\nu - \delta\nu) - I_{dark}) \times \\ \times \exp\left(-A \cdot \exp\left(-\frac{Mc^2}{2k_B T}\frac{(\nu-\nu_0)^2}{\nu_0^2}\right)\right) + I_{plasma}. \quad (7)$$

Phase shift $\delta\nu$ was randomly varied between -10 and 120 MHz. We generated random $I_{dark} = 7 \pm 0.4$ mV and $I_{plasma} = 20 \pm 1$ mV. The random values were uniformly distributed within these ranges. After that, we added Gaussian noise to the $I(\nu)$, I_{plasma} and I_{dark}. All parameters were chosen to be similar to the real experimental values. We performed the tests with 20 different $I_{laser}(\nu)$ curves taken from real experiments, and for every curve, we generated 100 tests.

The results of the comparison are presented in figure 4(a). We tested the fit (6) with n from 2 to 6. This fit with the polynomial degrees $n \leq 3$ gave very inaccurate

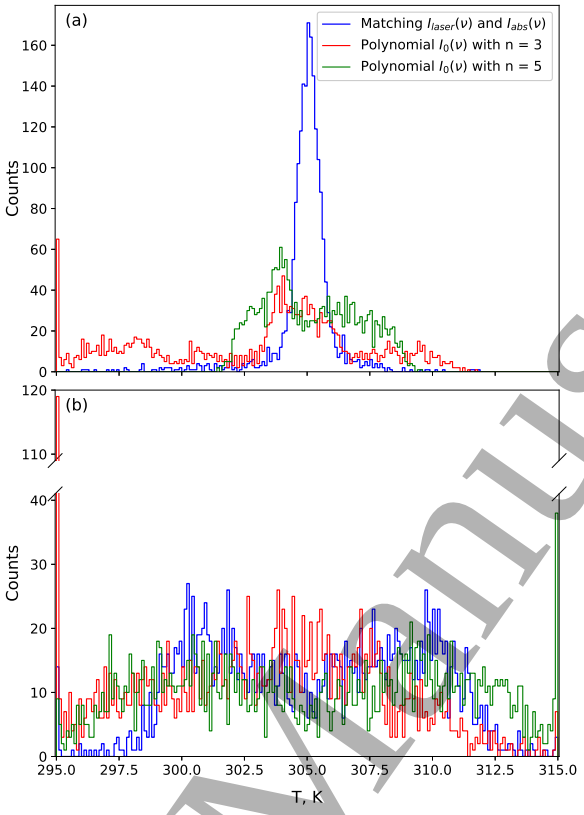

Figure 4. Distributions of temperatures determined from the artificially generated data by different methods (a) without and (b) with the disturbance caused by the self-excited dust-acoustic waves. The bins at the edges of abscissa accumulate also the results lying outside of the shown range. In both cases the matching $I_{laser}(\nu)$ and $I_{abs}(\nu)$ brings best results.

results. Higher polynomial degrees gave uncertainties of about ±3 K. We also tested if the extinction of the laser light on the dust can affect the calculated temperatures. Introducing the factor s of 0.8–0.99 changed the calculated temperatures by less than 0.01 K. The matching method showed an obvious advantage over the fits resulting in the uncertainty of about ±1 K.

In some cases, the measurements were conducted in the microparticle suspensions disturbed by the self-excited dust density waves (DDW) [27]. This led to small modulations of the signals detected by the photodiodes. The frequency of DDW was of the order of the scanning frequency. We included the effect of the waves into the model as sinusoidal signals with random frequencies, amplitudes and phases where the frequencies and the amplitudes were similar to those of the low-frequency noise we saw in the experimental signal. The results are presented in figure 4(b). Both data processing techniques resulted in a broad temperature distribution. Nevertheless, the matching technique produced less outlying results. For comparison, the matching technique gave errors more than 10 K only in 0.85 percent of the tests, while the polynomial fitting caused such spikes in 6.3 and 2.35 percent of the tests for $n = 3$ and $n = 5$ respectively.

Therefore, the matching technique showed a clear advantage under calm as well as under the DDW-disturbed conditions and was therefore used in the following analysis of experimental data.

5. Results and discussion

5.1. Experiments without microparticles

Temperatures measured using the top (T_t) and the bottom (T_b) beams are presented in figure 5. The data were obtained for different temperature of the chamber flanges (T_{fl}), which was caused by the difference in the room temperature on different days. The measured temperatures increased with the the room temperature and were systematically higher than T_{fl} by 5.4 ± 0.9 K.

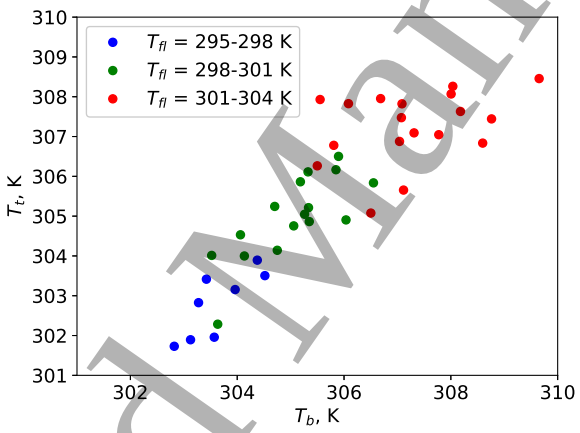

Figure 5. TDLAS-measured temperatures in a dust-free plasma at different temperatures of the chamber flanges. Different intervals of the temperature of the flanges T_{fl} are colour coded. Since the temperature difference control was not used, the temperatures of the top and the bottom flanges differed less than by 0.5 K. T_{fl} varied due to the natural variation of the room temperature.

For additional testing, we conducted experiments with controlled temperature difference (ΔT_{fl}) between the flanges. The measured temperature difference (ΔT_{beams}) could be calculated in two ways: T_b and T_t could be determined independently and subtracted one from another and, alternatively, a ratio of the top and bottom absorption profiles ($k_t(\nu)$ and $k_b(\nu)$, respectively) could be used. In the latter case, ΔT_{beams} was obtained by fitting

$$\ln\left(\frac{k_b(\nu)}{k_t(\nu)}\right) = \frac{Mc^2}{2k_B\nu_0^2}\frac{\Delta T_{beams}}{T_b T_t}(\nu-\nu_0)^2 + \text{const.} \quad (8)$$

T_b and T_t in the denominator have to be obtained from the individual profiles ($k_b(\nu)$, $k_t(\nu)$).

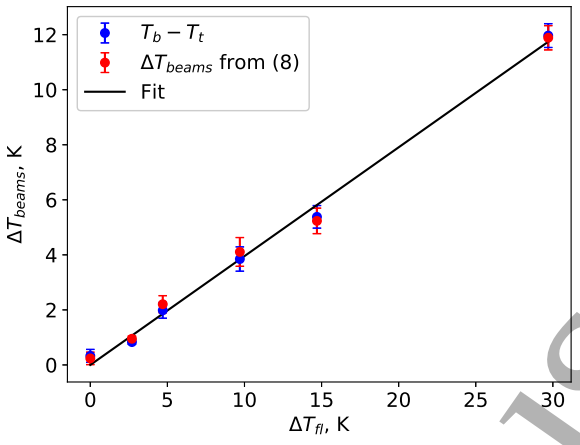

Figure 6. Dependence of the measured temperature difference ΔT_{beams} between the top and the bottom laser beams on the controlled temperature difference between the bottom and the top flanges. The values were obtained by averaging results from 3 to 13 experiments. The error bars show standard errors of the mean. The data are fitted by $\Delta T_{beams} = 0.40 \cdot \Delta T_{fl}$

.

Both methods gave very similar results (see figure 6). ΔT_{beams} exhibited linear growth with ΔT_{fl}, and could be fitted by $\Delta T_{beams} = 0.40 \cdot \Delta T_{fl}$. The slope of the line was somewhat smaller than the ratio of the interbeam and interelectrode distances.

5.2. Effect of microparticles on the temperature

We performed the experiments with the variable amount of the microparticles. In these experiments we did not use the control of the temperature difference between the chamber flanges. Small microparticle suspensions levitated in the bottom part of the chamber, whereas larger suspensions extended almost into the entire discharge volume (see figure 7). The microparticle number density was $\sim 10^{11}\,\mathrm{m}^{-3}$. In some cases (e.g. as in figure 7(b)), the microparticle suspensions were disturbed by the DDW. Typical relative amplitude of the intensity oscillation due to the DDW was $\sim 10^{-4}$ after averaging over 100 oscillograms.

We used the fraction of laser light extinguished by the microparticles as a measure of their amount:

$$E = 1 - \left\langle \frac{I_{abs}(\nu) - I_{plasma}}{I_{laser}(\nu) - I_{dark}} \right\rangle_{|\nu-\nu_0| \gg \Delta\nu}. \qquad (9)$$

Averaging was performed over the points far from the spectral line center for which the absorption is negligible. These quantities (E_b and E_t for the bottom and the top beam, respectively) determined in different experiments are shown in figure 8. In case of small suspensions, the top beam passed above the suspension (as in figure 7(a)). Larger suspensions extinguished also the upper beam, but to a lesser extent than the lower one.

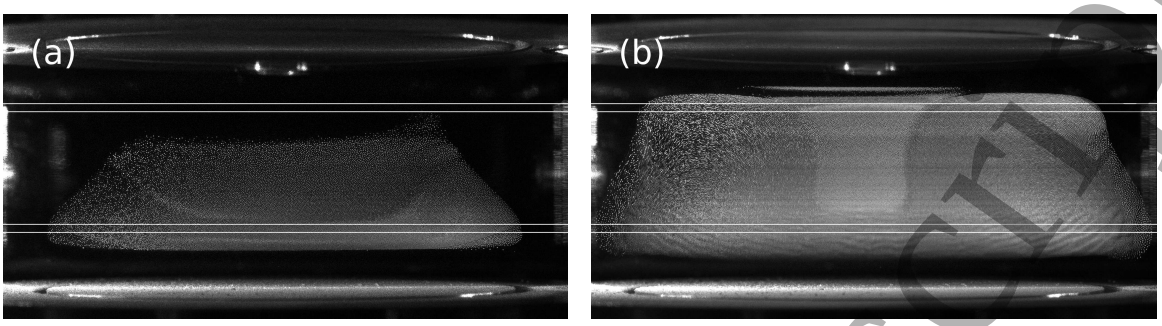

Figure 7. Images of (a) a small and (b) a large microparticle suspension used in the temperature measurement experiments. The horizontal lines denote the positions of the laser beams. In case (a), the laser beam passed the chamber above the suspension without crossing it. In case (b) the central part of the suspension is calm, whereas vortices are visible in the outer part of the suspension and DDW propagate in its bottom part.

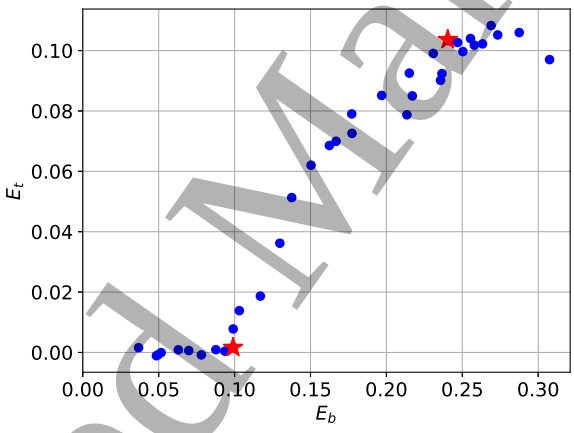

Figure 8. Fractions of laser light extinguished by dust in different experiments. The asterisks correspond to the suspensions in figure 7.

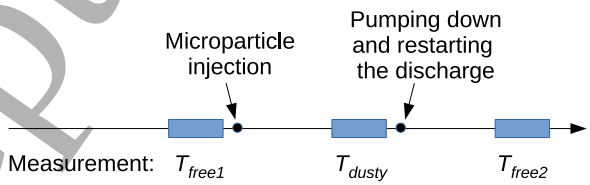

Figure 9. Experimental procedure for the determination of ΔT in equation (10). To reduce the effect of the discharge condition instability, three gas temperature measurements were performed: two measurement in a dust-free discharge and, between them, one measurement in a dusty discharge.

To reduce the effect of the uncontrolled environment variations, we applied the measurement procedure schematically shown in figure 9. After stabilization of the laser and the discharge (several hours after switching on), we measured the absorption

without the microparticles to determine T_{free1}. Then we injected the microparticles, waited 5–10 minutes to avoid the measurement during the initial redistribution of the suspension and measured T_{dusty}. During the measurement of I_{laser} and I_{dark}, the discharge was switched off and the suspension was pumped out. After switching the discharge on again and waiting 5–10 minutes for its stabilization, we measured the absorption without the microparticles to obtain T_{free2}. We repeated the procedure to obtain further data points using previous value of T_{free2} as next value of T_{free1}. Each absorption measurement included the recording of all the signals from equation (4) and took 7–8 minutes. All absorption measurements were accompanied by measurements of the respective temperatures of the flanges $T_{fl\,free1}$, $T_{fl\,dusty}$, $T_{fl\,free2}$.

Dust-induced temperature variation was calculated by

$$\Delta T = \delta T_{dusty} - \frac{\delta T_{free1} + \delta T_{free2}}{2}, \tag{10}$$

where

$$\begin{aligned} \delta T_{free1} &= T_{free1} - T_{fl\,free1}, \\ \delta T_{dusty} &= T_{dusty} - T_{fl\,dusty}, \\ \delta T_{free2} &= T_{free2} - T_{fl\,free2}. \end{aligned} \tag{11}$$

The results are presented in figure 10. The scatter in the resulting ΔT increased with the amount of microparticles and reached about 4 K at E_b of about 0.25. Nevertheless, figure 10 shows the evidence of the gas temperature increase in the presence of microparticles. This effect was predicted in [16] for the dc discharge in neon and explained by the increase of the longitudinal electric field in presence of dust. In our case, in a rf discharge, a similar mechanism could also be at work. In the presence of microparticles, the electrons are immobilized, which allows for the deeper penetration of rf electric field into the plasma [13, 28].

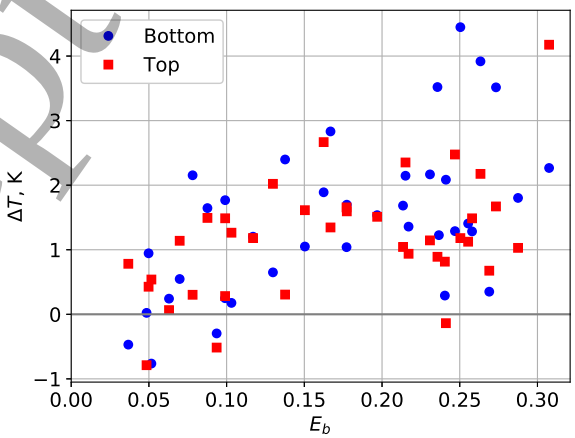

Figure 10. Dust-induced growth of the gas temperature. E_b is used as a measure of the levitated dust amount.

The microparticle-induced modification of the spectral line absorption strength was calculated as

$$R = \frac{2(k(\nu_0)l)_{dusty}}{((k(\nu_0)l)_{free1} + ((k(\nu_0)l)_{free2}}. \quad (12)$$

The results are presented in figure 11. The presence of the microparticles always caused growth of the absorption for the top beam. On the other hand, small suspensions caused a decrease of the absorption for the bottom beam, whereas large suspensions induced the absorption growth.

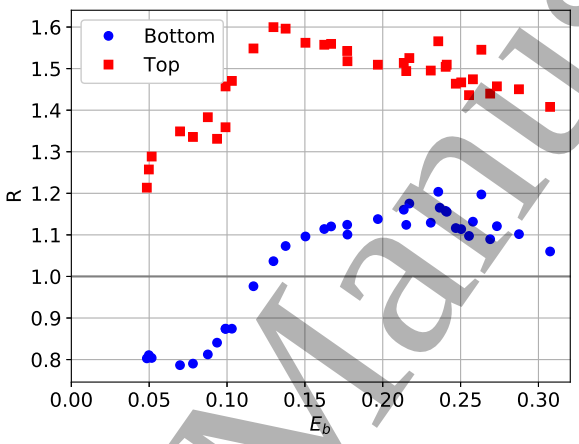

Figure 11. Relative microparticle-induced change of the absorption strength.

Supposing no variation of the absorption length l between dusty and dust-free cases, the results can be explained by a competition of such effects as electron depletion [12], metastable quenching [8] and electron temperature increase [10] in the presence of microparticles. Among those effects, the first two are of local nature, leading to the decrease of the metastable atom density, whereas the third one is non-local and therefore affects also the region where no microparticles are present.

In contrast to the metastable density, for the gas temperature, the effect of the microparticle cloud is always of the same sign for the top and the bottom beams. This suggests that the role of a local effect (absorption of electron and ion fluxes by the microparticles [14]) on the gas heating is negligible. The observed heating might be attributed to the global redistribution of the heat sources in the discharge [16].

6. Conclusion

We performed tunable diode laser absorption spectroscopy measurements of gas temperatures in an argon capacitively coupled rf discharge without and with microparticles at low power.

The measurements were performed with two laser beams at different heights simultaneously. Without external heating, the measured temperatures were several K higher than those of the flanges. If we heated the bottom electrode, the measured

temperature difference between the beams was proportional to the temperature difference between the chamber flanges.

The experiment showed that the presence of microparticles induced growth of the gas temperature. Heating was observed on both beams and vanished with the reduction of the microparticle amount. The metastable density exhibited different dust-induced modification: small suspensions caused reduction on the bottom beam and increase on the top beam, whereas, for larger suspensions, the increase was observed for both beams.

Spatial difference in the dust-induced modification of the gas temperature and metastable density allows to conclude about the underlying physical mechanisms. For the metastable density, the dust-induced modification is the result of the interplay between the local absorption of the metastable atoms and electrons by the microparticles and non-local increase of the electron temperature. For the gas temperature, it seems like the non-local redistribution of heat sources always dominates, whereas the local heat deposition due to absorption of electrons, ions and excited atoms on the microparticles seems to be negligible.

For further understanding, space resolved measurement techniques like laser-induced fluorescence or TDLAS with a laser sheet are required.

Acknowledgments

This work was supported by Deutscher Akademischer Austauschdienst (DAAD), scholarship No. 57424731.

The PK-3 Plus chamber was funded by the space agency of the Deutsches Zentrum für Luft- und Raumfahrt e. V. with funds from the federal ministry for economy and technology according to a resolution of the Deutscher Bundestag under grant No. 50WP0203, 50WM1203.

We would like to thank Dr. V. Yaroshenko for careful reading of our manuscript and valuable suggestions.

[1] Morfill G E and Ivlev A V 2009 *Rev. Mod. Phys.* **81**(4) 1353–1404

[2] Ivlev A, Löwen H, Morfill G and Royall C P 2012 *Complex Plasmas and Colloidal Dispersions: Particle-Resolved Studies of Classical Liquids and Solids* (*Series in Soft Condensed Matter* vol 5) (World Scientific Publishing Co. Pte. Ltd.)

[3] Pustylnik M Y, Fink M A, Nosenko V, Antonova T, Hagl T, Thomas H M, Zobnin A V, Lipaev A M, Usachev A D, Molotkov V I, Petrov O F, Fortov V E, Rau C, Deysenroth C, Albrecht S, Kretschmer M, Thoma M H, Morfill G E, Seurig R, Stettner A, Alyamovskaya V A, Orr A, Kufner E, Lavrenko E G, Padalka G I, Serova E O, Samokutyayev A M and Christoforetti S 2016 *Rev. Sci. Instrum.* **87** 093505

[4] Goree J, Morfill G E, Tsytovich V N and Vladimirov S V 1999 *Phys. Rev. E* **59**(6) 7055–7067

[5] Balabanov V V, Vasilyak L M, Vetchinin S P, Nefedov A P, Polyakov D N and Fortov V E 2001 *J. Exp. Theor. Phys.* **92** 86–92

[6] Rothermel H, Hagl T, Morfill G E, Thoma M H and Thomas H M 2002 *Phys. Rev. Lett.* **89**(17) 175001

[7] Mitic S, Sütterlin R, Höfner A V I H, Thoma M H, Zhdanov S and Morfill G E 2008 *Phys. Rev. Lett.* **101**(23) 235001

[8] Do H T, Kersten H and Hippler R 2008 *New J. Phys.* **10** 053010
[9] Do H T, Sushkov V and Hippler R 2009 *New J. Phys.* **11** 033020
[10] Stefanović I, Sadeghi N and Winter J 2010 *J. Phys. D: Appl. Phys.* **43** 152003
[11] Sukhinin G I, Fedoseev A V, Antipov S N, Petrov O F and Fortov V E 2013 *Phys. Rev. E* **87** 013101
[12] Sushkov V, Herrendorf A P and Hippler R 2016 *J. Phys. D: Appl. Phys.* **49** 425201
[13] Pustylnik M Y, Semenov I L, Zähringer E and Thomas H M 2017 *Phys. Rev. E* **96**(3) 033203
[14] Maurer H R and Kersten H 2011 *J. Phys. D: Appl. Phys.* **44** 174029
[15] Shumova V V, Polyakov D N, Mataybaeva E K and Vasilyak L M 2019 *Phys. Lett. A* 125853
[16] Polyakov D N, Shumova V V and Vasilyak I M 2014 *Dig. J. Nanomater. Bios.* **9** 1249–1254
[17] Pikalev A A and Luizova L A 2014 *Ukr. J. Phys.* **59** 375–378
[18] Klumov B A, Ivlev A V and Morfill G 2003 *JETP Lett.* **78** 300–304 ISSN 1090-6487
[19] Akdim M R and Goedheer W J 2003 *Phys. Rev. E* **67**(6) 066407
[20] Makabe T 2019 *J. Phys. D: Appl. Phys.* **52** 213002
[21] Hübner S, Sadeghi N, Carbone E A D and van der Mullen J J A M 2013 *J. Appl. Phys.* **113** 143306
[22] Thomas H M, Morfill G E, Fortov V E, Ivlev A V, Molotkov V I, Lipaev A M, Hagl T, Rothermel H, Khrapak S A, Suetterlin R K, Rubin-Zuzic M, Petrov O F, Tokarev V I and Krikalev S K 2008 *New J. Phys.* **10** 033036
[23] Pustylnik M Y, Ivlev A V, Sadeghi N, Heidemann R, Mitic S, Thomas H M and Morfill G E 2012 *Phys. Plasmas* **19** 103701
[24] Ochkin V 2009 *Spectroscopy of Low Temperature Plasma* (WILEY-VCH Verlag GmbH & Co. KGaA)
[25] Kaupe J, Coenen D and Mitic S 2018 *Plasma Sources Sci. Technol.* **27** 105003
[26] Press W H, Teukolsky S A, Vetterling W T and Flannery B P 2007 *Numerical Recipes: The Art of Scientific Computing* (Cambridge, New York, Melbourne, Madrid, Cape Town, Singapore, São Paulo: Cambridge University Press)
[27] Schwabe M, Rubin-Zuzic M, Zhdanov S, Thomas H M and Morfill G E 2007 *Phys. Rev. Lett.* **99**(9) 095002
[28] Killer C, Bandelow G, Matyash K, Schneider R and Melzer A 2013 *Phys. Plasmas* **20** 083704

Plasma Sources Science and Technology

Dim and bright void regimes in capacitively-coupled RF complex plasmas

To cite this article before publication: Aleksandr Pikalev *et al* 2021 *Plasma Sources Sci. Technol.* in press https://doi.org/10.1088/1361-6595/abe0a2

Dim and bright void regimes in capacitively-coupled RF complex plasmas

A Pikalev[1], I Semenov[2], M Pustylnik[1], C Räth[1] and H Thomas[1]

[1] Institut für Materialphysik im Weltraum, Deutsches Zentrum für Luft- und Raumfahrt e. V. (DLR), 82234 Weßling, Germany

[2] Leibniz Institute for Plasma Science and Technology, 17489 Greifswald, Germany

E-mail: Aleksandr.Pikalev@dlr.de

Abstract.

We demonstrate experimentally that the void in capacitively-coupled RF complex plasmas can exist in two qualitatively different regimes. The "bright" void is characterized by bright plasma emission associated with the void, whereas the "dim" void possesses no detectable emission feature. The transition from the dim to the bright regime occurs with an increase of the discharge power and has a discontinuous character. The discontinuity is manifested by a kink in the void size power dependencies. We reproduce the bright void (mechanically stabilized due to the balance of ion drag and electrostatic forces) by a simplified time-averaged 1D fluid model. To reproduce the dim void, we artificially include the radial ion diffusion into the continuity equation for ions, which allows to mechanically stabilize the void boundary due to very weak electrostatic forces. The electric field at the void boundary occurs to be so small that it, in accordance with the experimental observation, causes no void-related emission feature.

Keywords: dusty plasma, RF discharge, RF-period-resolved optical emission spectroscopy, void, 1D fluid model.

1. Introduction

Complex or dusty plasma is a medium containing ionized gas and micron-sized solid particles. It is used in basic research as a model system for particle-resolved studies of generic condensed matter phenomena [1–3]. For such studies, homogenous microparticle suspensions are desirable. Therefore, many of the complex plasma experiments are performed in microgravity conditions [4–6]. However, microgravity does not guarantee homogeneous distribution of the microparticle component. The appearance of a void, i. e. a microparticle-free area, is one of most common disturbances of the complex plasma homogeneity under microgravity conditions [7, 8]. The void formation and growth also determine the nanoparticle generation cycle in plasma reactors [9]. Although the void formation has been studied for at least two decades, understanding of its behaviour is still incomplete.

One of the difficulties in studying the void (as well as complex plasmas in general) is that the microparticles immersed into the gas discharge plasma change its properties. It was noticed already at the beginning of complex plasma research [10–13]. This influence was confirmed and detailized in recent works [9, 14–16].

The results of void closure experiments in [17] were interpreted in terms of a single-particle approach, i.e., the force balance was treated for a single microparticle immersed in the simulated field of microparticle-free plasma parameters. According to [17], the void forms due to the balance of electrostatic and ion drag forces. This idea, even nowadays, remains the baseline in the understanding of the physics of the void.

In theoretical work [18], a double layer formation and time averaged flows of the electrons and ions in the vicinity of the void boundary were investigated. In works [19–22], a theory of a spherical void in an infinite microparticle suspension was developed. No RF electron dynamics was considered.

To get better insight into microparticle-plasma interaction, the entire discharge was simulated in [7, 15, 16, 23–28]. In [23], quite a comprehensive 1D fluid model was developed. It included two primary physical mechanisms of plasma-microparticle interaction, namely the absorption of plasma electrons and ions on the microparticles and the contribution of the microparticles to plasma quasineutrality. This model reproduced the appearance of the void with reducing the pressure and a peak of microparticle density at the void boundary often observed in the experiments.

2D fluid models were presented in [7, 24–26]. These models demonstrated the increase of the electron energy in the presence of the microparticles. If the void existed in the model, the electron density inside the void was much higher than inside the microparticle suspension. The simulated void size was compared in [7, 26] with the experiment [17]. Although the model qualitatively reproduced the void formation and growth with increasing RF voltage, it predicted higher RF voltage of the void formation than it was observed in the experiment. The "single-particle" void was shown to be larger and appear for lower powers than the void with the microparticle suspension effect considered.

Before [15], the researchers mostly aimed at comparing the dimensions and onset of void formation in the simulations and the experiment and did not attempt to treat the problem in its entire complexity which includes the background plasma along with the microparticle suspension. Even the development of particle-in-cell (PIC) codes [27, 28] with a more thorough treatment of the electron kinetics did not lead to an immediate breakthrough. The first attempt [15] to compare the outcome of the PIC simulations with the microparticle arrangement and RF-period-resolved emission patterns measured simultaneously in the experiment was unsuccessful in the sense of void problem since in the simulations, "the sharp dust density gradients at the void edges resulted in unwanted boundary effects". The PIC model of [16] was able to qualitatively reproduce the spatiotemporal emission pattern, but was unable to reproduce the formation of void. Imposing a fixed configuration of microparticles with a void in the simulation led to tremendous forces on the void boundaries and to the drastic distortion of the spatiotemporal emission pattern.

Spectroscopic properties of the stable void were studied in [9, 15, 16, 29]. According to [15], the period-resolved emission spectroscopy showed strong increase of the discharge emission in the center of the discharge, where the void was located. The void in that experiment was so large that it was not clear if the emission was coupled with the void. Similar experiments [16] with varying the void position showed no void-related feature in the spatio-temporal emission patterns.

In the discharge image published in [29], a bright emission from the void is clearly visible. Similar feature was also present in the distribution of the resonance atoms measured with laser-induced fluorescence. The plasma emission and the metastable density distribution were studied in [9] for the argon-acetylene mixture. The void appeared and grew in size with the growth of the nanoparticles. Although the plasma emission and the metastable density decreased during the void growth, no local effects could be seen.

In some conditions, the void becomes unstable for high discharge powers and rotates around the discharge axis. For such experiments, bright emission inside the void (so called "plasmoid") was reported in [30–32]. The bright emission from the void was also observed during the void-collapse phase of the heartbeat instability [33, 34].

The literature review given above shows that there are still lots of unsolved issues regarding the voids in complex plasmas. State-of-the-art theories explain neither the mechanisms controlling the plasma emission inside the void, nor the void stability. The inability to explain the void formation under certain condition implies that mechanisms other than simple balance between the electrostatic and ion drag forces may be responsible for the void formation.

In the present work, we tried to make the next step in the understanding of the void problem. We performed a systematic investigation of capacitively-coupled RF complex plasmas with the void. The investigation included measurements of the microparticle configurations, time-averaged emission profiles and RF-period-resolved spatiotemporal emission profiles. We interpret these data using a simplified and flexible 1D fluid

model of a microparticle-containing RF discharge with artificially added radial diffusion. Using the experimental data and the model, we were able to demonstrate the limits of applicability of the old void formation mechanism (due to a strong ion flow from the void to the suspension) and suggest a novel mechanism explaining the void formation outside those limits.

2. Experiment

The experiments were conducted in the ground-based PK-3 Plus chamber [5]. The plasma was produced by means of a capacitively-coupled rf discharge. Two electrodes were driven in a push-pull mode by a sinusoidal signal with the frequency of 13.56 MHz. Argon fed into the chamber with 3 sccm gas flow was used as a working gas. We conducted the experiments with the gas pressure of 20, 37 and 80 Pa. The gas residence time in the chamber was 1.6–6.4 s. Switching the gas flow off caused no visible change in the motion of the microparticles. We used melamine formaldehyde spheres with the diameter of $1.95 \pm 0.05\,\mu$m as microparticles. The microparticles were injected into the discharge by a electromagnet-driven dispenser through a sieve. We used the number of the injections as a measure of the microparticle amount in the plasma.

Under ground laboratory conditions, the microparticles concentrate themselves in the vicinity of the lower electrode. To obtain large volumetric microparticle suspensions, we compensated the gravitational force by means of themophoresis [35]. The temperature gradient between the electrodes was controlled by heating the bottom electrode with an electric heater and cooling the top electrode with fans. We measured temperatures on the outer surfaces of the two chamber flanges with Tinytag Explorer data logger. The temperature difference was 14–15 K during the experiments. According to [36], the horizontal temperature gradient on the bottom electrode induced by the external heating was 0.5 % of the vertical temperature gradient.

The microparticles were illuminated by a laser sheet with the wavelength of 532 nm. Two Ximea MQ042RG-CM video cameras with interference bandpass filters captured the microparticle motion and the plasma emission at the same discharge area. The filters had the central wavelength of 532 and 750 nm, respectively, and the width of the transmission band of filters was about 10 nm. Hence, the plasma glow observation camera captured the plasma radiation in 750.4 and 751.5 nm spectral lines. These lines correspond to the transitions $2p_1 \rightarrow 1s_2$ and $2p_5 \rightarrow 1s_4$ in the Paschen notation. The spatial resolution of the cameras was about 37 μm/pixel.

These diagnostics were supplemented with a RF-period-resolved optical emission spectroscopy, described in details in [16]. RF-period-resolved evolution of the plasma emission was observed by an ICCD camera equipped with a 750 nm central wavelength and 10 nm bandwidth filter. The 750.4 and 751.5 nm argon lines transmitted by it have the lifetimes of 22.5 ns and 24.9 ns, respectively [37]. The camera was synchronized with the rf signal through the frequency divider, which sent a synchronization pulse after every 512 RF cycles. The gate width of the ICCD camera was set to 10 ns. The

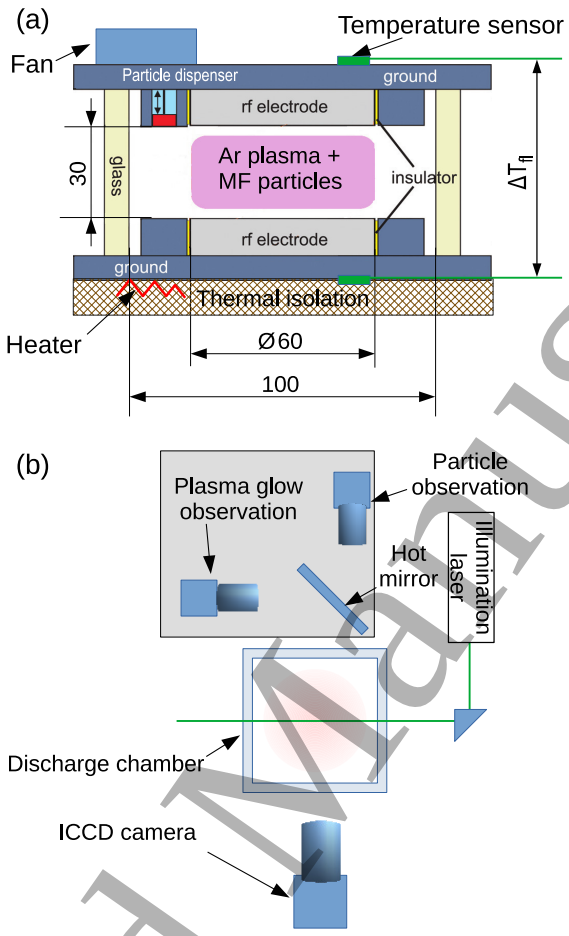

Figure 1. Scheme of the experimental setup, (a) — side view, (b) — top view. The heart of the experiment is the PK-3 Plus chamber [5]. The bottom flange of the chamber can be heated to control a temperature gradient between the electrodes. The two cameras on the one side observe the microparticle motion and period-averaged plasma emission. The ICCD camera on the other side performs RF-period-resolved emission registration.

signal was accumulated over the total exposure time of 1 s. The ICCD gate was moved over almost three rf periods with a step of 2 ns. The spatial resolution of the ICCD camera was about 92 μm/pixel.

All three cameras were focused on the central cross-section of the discharge chamber.

We injected the microparticles into a low-power (200–300 mW) discharge. For the suspension stabilization, we waited several minutes, increased the discharge power up to the maximal value used in the experiment ($\sim$ 1.2 W) and decreased it to the minimal value of 100 mW ($\sim$ 250 mW for the pressure of 80 Pa). After that, we observed the microparticle suspension and the plasma emission while increasing the discharge power in steps. The power step was slightly pressure dependent. For the pressure of 20 and 37 Pa it was about 100 mW. For the pressure of 80 Pa and low discharge power, the step was about 80 mW, but for the high discharge power, the power measurements were

inaccurate due to too high discharge current. The peak-to-peak voltages between the electrodes for the presented experimental conditions are shown in figure 2. The injection of the microparticles caused a drop of the discharge current, whereas the decrease of the voltage was insignificant. After every change of the power, we waited 2–3 seconds for the microparticle redistribution. The plasma emission images were obtained by averaging 20–60 frames after the suspension stabilization. After reaching the maximal power, we continued the measurements by decreasing the power in the same steps. The results for increasing and decreasing power were similar and no hysteresis was found, therefore we present only the results with the increasing power.

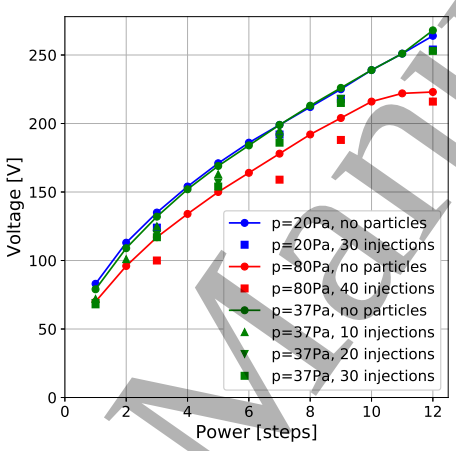

Figure 2. Power dependence of the peak-to-peak voltage. The values for the pristine plasma are reproducible with an accuracy of 5 V. The reproducibility of the values with the microparticles is limited by the reproducibility of the microparticle suspension configuration.

3. Experimental results

For low power, no void was present. The onset of the void formation was pressure dependent: step 1 for the pressure of 20 Pa, step 2 for 37 Pa and step 3 for 80 Pa. Within several power steps after the void formation, no void-related feature could be seen in the plasma emission. In the following, we will call this regime "dim void" (see figures 3(a–b)). After the power reached a certain threshold, bright emission associated with the void area could be observed. In the following, we will call this regime "bright void" (see figures 3(c–d)).

To make the effect of the microparticles more pronounced, we subtracted the emission of the pristine plasma from the images with the microparticles. The results are presented in figures 4–5.

The boundaries of the voids shown in figures 4–5 were found as the boundaries of the areas in the microparticle suspension images with the intensity less than a certain threshold. Using these boundaries, the void dimensions (height and width) were

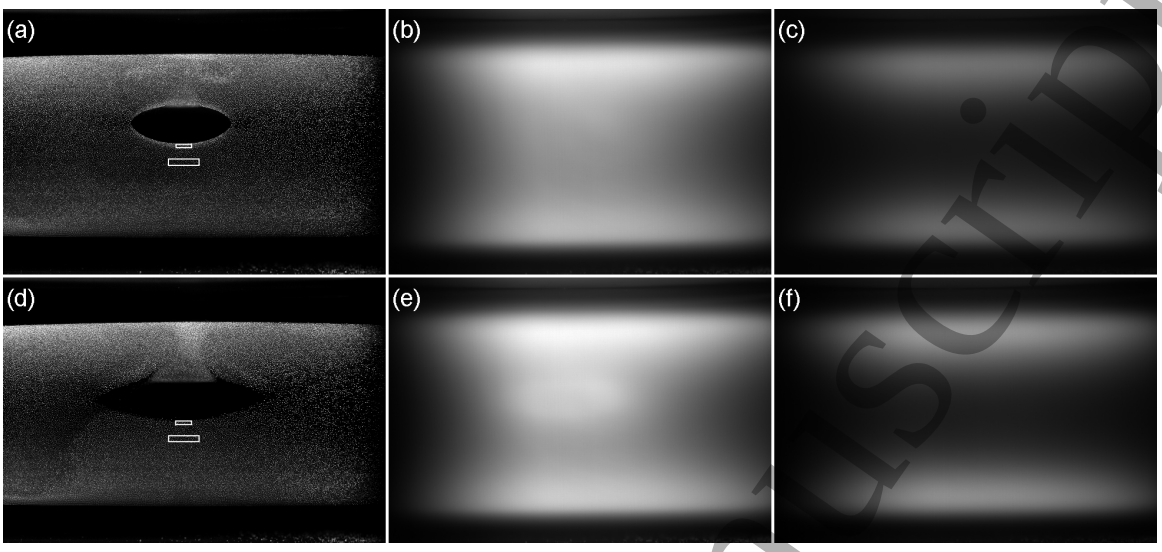

Figure 3. Images of the microparticle suspensions (a, d) and the plasma emission (b, e) with and (c, f) without the microparticles. The pressure was 37 Pa, the discharge power was 5 steps for plates (a–c), and 7 steps for plates (d–f) (see figure 2). The white rectangles depict the areas used for figure 6(c).

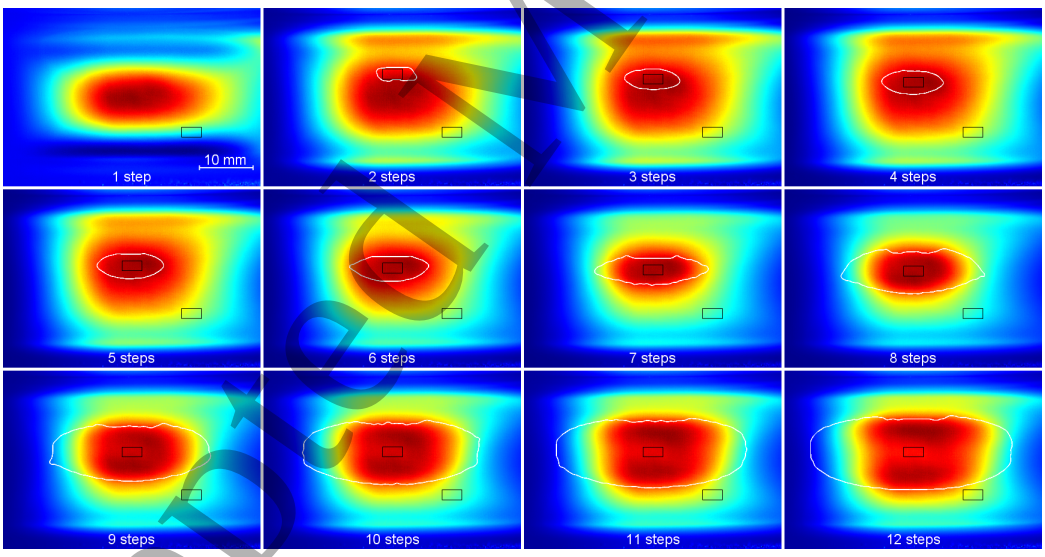

Figure 4. The colour-coded effect of the microparticles (30 injections) on the plasma emission with the filter for 750 nm. Pressure — 37 Pa, power — 1–12 steps (see figure 2). Every image has its own colour scale. The white lines depict the void boundaries. The black rectangles show the areas used for figure 7.

determined. To mitigate the influence of small-scale roughness of the boundaries on the void dimensions, the height and width of the void were determined as, repectively, the height and width of such a rectangle that each of its sides cuts off four percent of the total amount of the points belonging to the boundary. Also, we measured the effect of the microparticles on the plasma emission intensity inside the void area and outside the

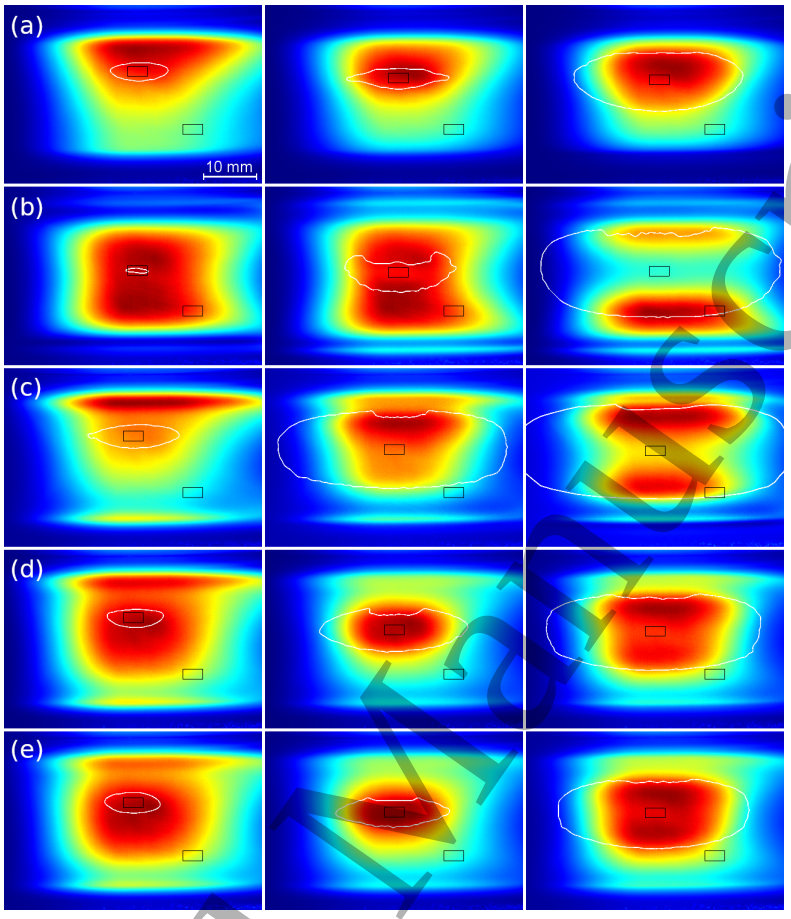

Figure 5. The same as figure 4 for the power of (from left to right) 3, 7 and 11 steps (see figure 2) and (a) pressure 20 Pa, 30 injections; (b) 80 Pa, 40 injections; (c) 37 Pa, 10 injections; (d) 37 Pa, 20 injections; (e) 37 Pa, 30 injections.

void.

The data are presented in figures 6–7. The areas of the images used to measure the plasma emission are depicted in figures 4–5 with the black rectangles. Due to imperfect gravity compensation, the void was located not in the center of the chamber, and its position was dependent on the discharge power. That is why we adjusted the position of the measurement area inside the void for every power step. The position of the area outside the void was fixed.

The experiments showed that, after the void formation, its size stabilized, and the void was growing only slightly with the power increase, similarly to [8,17,38]. However, after the power reached a certain value, the horizontal void size started increasing faster. After that, the bright plasma emission appeared inside the void and the void height started growing faster. The void, therefore, experienced the transition from dim to bright regime. For the large voids, the microparticles cause the plasma emission increase concentrated near the top and the bottom void boundaries. This effect is more pronounced for higher gas pressure.

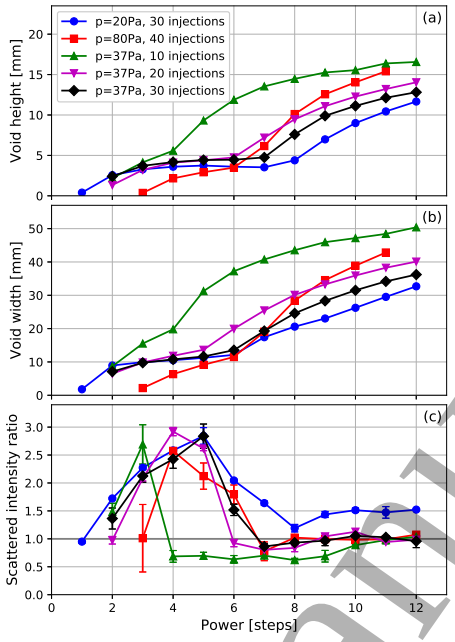

Figure 6. The parameters of the void for different discharge conditions. (a) — the void height; (b) — the void width; (c) — the ratio of the 532 nm light intensity scattered on the microparticles at the bottom void border and in the bulk suspension. Uncertainties of the void sizes are 0.7 mm. The error bars in (c) show 95% confidence intervals related to position ambiguity of the areas used to take the intensity.

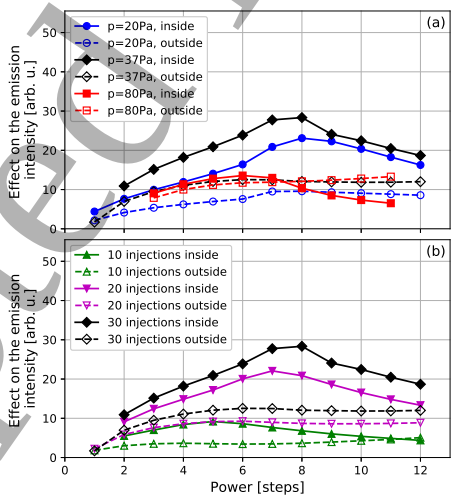

Figure 7. The microparticle effect on the plasma emission (in arbitrary units) inside and outside the void area. (a) — for different gas pressures; (b) — for the gas pressure of 37 Pa and different amounts of the microparticles. The uncertainties can be estimated comparing these values with the values obtained during decreasing the discharge power. The differences were less than 0.7 inside the void and 0.2 outside the void.

We also noticed a transformation of the microparticle arrangement on the void boundary during this transition. At the dim void boundary, the microparticle suspension was denser than in the bulk, whereas for the bright void boundary, no density peak was observed, similar to the measurements reported in [17]. The effect is qualitatively visible in figures 3 (a, c). To quantify it, we calculated the ratio of the averaged scattered light intensity (assuming it to be proportional to the microparticle number density) in a small rectangle at the bottom void boundary and in a rectangle in the microparticle suspension bulk (see figure 6 (c)). Examples of such rectangles are shown in figures 3. For every image, we measured these intensities 3 times slightly varying the position of the areas and averaged the results.

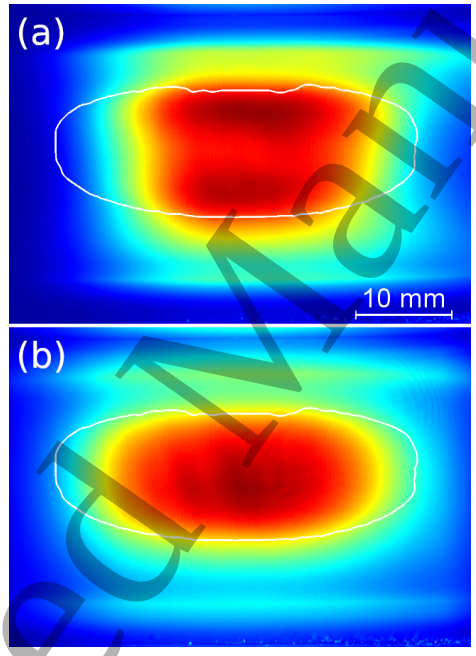

Figure 8. The colour-coded effect of the microparticles on the plasma emission with the filter for (a) 750 nm, (b) 810 nm. Pressure — 37 Pa, power — 12 steps (see figure 2), 30 injections of the microparticles.

We also observed the plasma emission through a narrow-band filter with 810 nm central wavelength, which transmitted 810.4 and 811.5 nm spectral lines. The effect of the microparticles on the plasma emission in these lines is similar, but no sheaths on the void boundaries were observed even for the largest power (see figure 8).

The results of the RF-period-resolved optical emission spectroscopy are presented in figure 9. Every pixel column for this spatiotemporal pattern was obtained by averaging the intensities along the horizontal dimension a central part of one frame. The width of the averaged area was about 6 mm. The images in figure 9 are the difference between the patterns with and without the microparticles for the respective conditions. Examples of such spatio-temporal patterns without the subtraction can be found in [16].

Every RF-period resolved measurement took several minutes. For this time, the

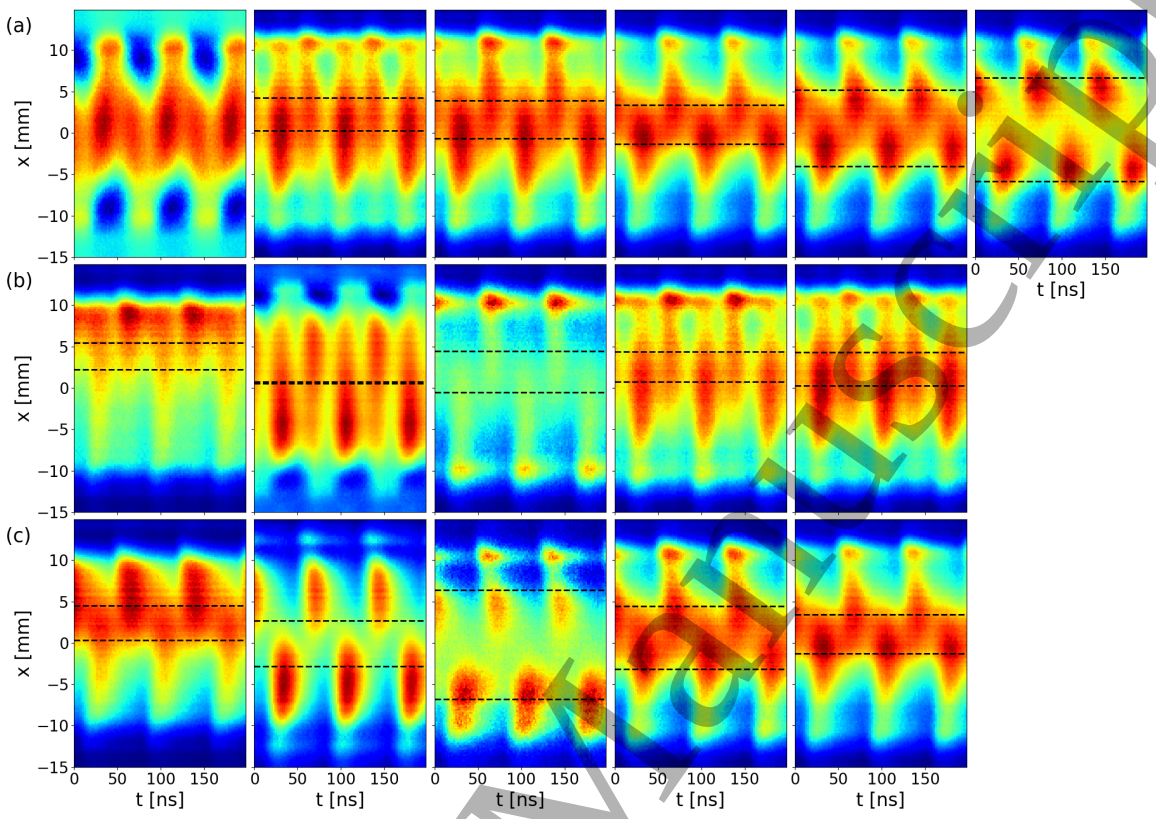

Figure 9. Spatiotemporal patterns of the microparticle effect on the plasma emission in the center of the discharge image for (a) pressure 37 Pa, 30 injections, power values (from left to right) of 1, 3, 5, 7, 9 and 12 steps; (b) power of 3 steps and (from left to right) pressure 20 Pa and 30 injections, 80 Pa and 40 injections, 37 Pa and 10 injections, 37 Pa and 20 injections, 37 Pa and 30 injections and (c) power 7 steps and same pressures and microparticle amounts as for plate (b). x is the coordinate along the discharge axis with $x = 0$ in the discharge center. Every image was colour-coded individually. The dashed lines depict the void boundaries. In plate (a), the microparticles caused decrease of the plasma emission near the expanding sheath for the lowest power. Correspondence of power steps and rf peak-to-peak voltage is shown in figure 2.

void drifted less than 1 mm downwards due to etching or separation of the microparticles. We measured the void position before and after the RF-period-resolved measurements and used the averaged values as the void boundaries in figure 9.

The results of the RF-period-resolved spectroscopy are in accord with the RF-period-averaged results. In the case of low-power discharge, the effect of the microparticles is significant for entire discharge height every half period. It leads to a more uniform spatial distribution of the emission intensity, similar to [16]. For the lowest power, the microparticles cause the emission increase near collapsing sheath, but smaller effect or even decrease of the emission near expanding sheath, as reported in [15].

With the increase of power, the effect appears only inside the void and between the void and the expanding sheath. With further increase of the power, the emission

increase concentrates near the void boundary that corresponds to the electrode with the expanding sheath.

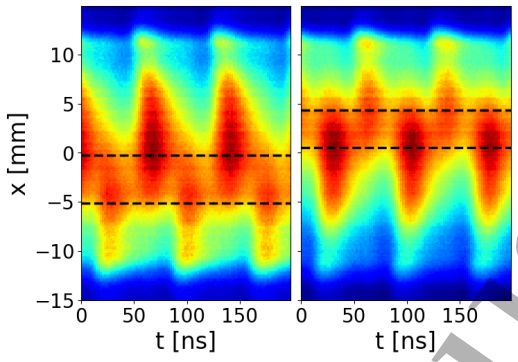

Figure 10. Spatiotemporal patterns of the microparticle effect on the plasma emission for different void position for the pressure of 37 Pa and the power of 7 steps (see figure 2).

We varied the vertical position of the bright void by changing the temperature difference between the electrodes while keeping the discharge power, gas pressure and microparticle amount constant. The results are shown in figure 10. We see that the emission pattern moves together with the void. Therefore, the emission profile observed in the bright void regime is really void-related.

4. Discussion

4.1. Time-averaged 1D fluid model

To provide a qualitative analysis of the experimental results, we consider a simple one-dimensional fluid model that describes time-averaged profiles of the electron, ion and dust number densities near the discharge axis. The model is applied to analyse possible configurations of microparticle suspensions and corresponding distributions of the electric field in the discharge. This information is then used to discuss the emission patterns observed experimentally.

Let x denote the discharge axis. We assume that $x \in [0, L]$, where $x = 0$ is the point in the middle of the discharge gap and $x = L$ is the point at the electrode surface ($L = 15\,\mathrm{mm}$). The distribution of the ion density, n_i, is governed by the continuity equation:

$$\frac{\partial}{\partial x}(n_i u_i) = G_{ion} - G_d, \tag{1}$$

where u_i is the ion velocity, G_{ion} is the ionization source term, G_d is the sink term due to absorption of ions by the microparticles. The ion flux in equation (1) is approximated as

$$n_i u_i = n_i \bar{u}_i - D_i \partial n_i / \partial x, \tag{2}$$

where $D_i = 0.012\,\mathrm{m^2 s^{-1}}$ is the ion diffusion coefficient and $\bar{u}_i$ is the ion drift velocity defined as a function of the local electric field, E. The ion drift velocity is obtained by solving the equation $eE = \omega_{ia}(\bar{u}_i) m_i \bar{u}_i$, where m_i is the ion mass and ω_{ia} is the effective ion-atom collision frequency defined as [39]: $\omega_{ia} = \sigma_0 n_g \sqrt{u_0^2 + \bar{u}_i^2}$, where n_g is the number density of gas atoms, $\sigma_0 = 10^{-18}\,\mathrm{m^2}$, $u_0 = 550\,\mathrm{m\,s^{-1}}$ (here $n_g = p_g/k_\mathrm{B}T_g$, where $T_g = 300\,\mathrm{K}$ and p_g is the gas pressure). This approximation agrees well with the Monte-Carlo simulation data for moderate drift velocities [40]. For simplicity, we neglect the effect of microparticles on the ion drift flow. The estimates show that this assumption is acceptable for the conditions of the present study.

The electron density, n_e, is assumed to obey the Boltzmann relation, which can be written in the following form:

$$\mu_e E n_e = -D_e \partial n_e / \partial x, \tag{3}$$

where μ_e, D_e are the electron mobility and diffusion coefficient, respectively.

The microparticle number density, n_d, is governed by the force balance:

$$-\frac{\partial p_d}{\partial x} + n_d \left(q_d E + F_{id} + F_{th}\right) = 0, \tag{4}$$

where q_d is the microparticle charge, p_d is the excess pressure of microparticles, F_{th} is the thermophoretic force associated with the internal heat sources of the plasma and F_{id} is the drag force exerted by ions on a single microparticle (the ion drag force). The gravity force is assumed to be compensated in the vertical direction (see Appendix A). The excess pressure in equation (4) can be calculated using the existing thermodynamic models [41–43]. In the present work the model of [43] was used. The expression for the excess pressure reads:

$$p_d = n_d k_\mathrm{B} T_g \left\{1 + \frac{\Gamma \kappa^4}{6[\kappa \cosh(\kappa) - \sinh(\kappa)]^3}\right\}, \tag{5}$$

where κ and Γ are the screening and coupling parameters, respectively. The screening and coupling parameters are given by $\kappa = a/\lambda_s$ and $\Gamma = q_d^2/\Delta k_\mathrm{B} T_g$, where $\Delta = (3/4\pi n_d)^{1/3}$ is the Wigner-Seitz radius and λ_s is the screening length of the interparticle interaction potential (we assume that particles interact via Yukawa potential). The microparticle density profile given by equation (4) is assumed to satisfy the integral constraint

$$\int_0^L n_d dx = \bar{n}_d L, \tag{6}$$

where $\bar{n}_d$ is the averaged microparticle density.

Equations (1), (3) and (4) are combined with the Poisson equation for the electric field:

$$\frac{\partial E}{\partial x} = \frac{e}{\varepsilon_0}\left(n_i - n_e - Z_d n_d\right), \tag{7}$$

where $Z_d = |q_d|/e$, with q_d being the microparticle charge. The microparticle charge is given by $q_d = 4\pi\varepsilon_0 a_d \varphi_d$, where a_d, φ_d are the particle radius and potential, respectively.

In order to close the model, it is necessary to define G_{ion}, G_d, F_{th} and F_{id} in

equations (1) and (4). The interaction of microparticles with the plasma components is relatively well studied and reliable expressions for G_d, F_{th}, F_{id} are available. The details on how these terms are calculated in the present work are given in Appendix A.

A self-consistent calculation of G_{ion} in equation (1) would require consideration of the electron energy balance and electron dynamics in the RF-discharge. This goes beyond the goal of the present analysis. Thus, we use G_{ion} as an input parameter of the model to study possible equilibrium configurations of the dust component. Particularly, we use the following model profile of the ionization source term:

$$G_{ion} = G_0 \left[\theta + (1-\theta)e^{-(x-x_0)^2/r_0^2}\right], \tag{8}$$

where $r_0 = 3\,\mathrm{mm}$, $x_0 = 10\,\mathrm{mm}$, G_0 and θ are adjustable parameters ($G_0 \sim 10^{20}\,\mathrm{m^{-3}s^{-1}}$, $\theta \lesssim 0.5$). The choice of the ionization source profile (8) was motivated by the results of particle-in-cell simulations performed for similar conditions [16].

The boundary conditions for equations (1)-(7) are as follows. We set $\partial n_s/\partial x = 0$ ($s = e, i, d$) and $E = 0$ at $x = 0$ and we use $\partial n_i/\partial x = 0$, $n_d = 0$, $n_e = \bar{n}_e$ at $x = L$. Here $\bar{n}_e$ is the averaged electron density at the electrode surface. According to the simulation results [16, 40], $\bar{n}_e$ lies in the range 10^{12} - $10^{13}\,\mathrm{m^{-3}}$ for the conditions of our study. For simplicity, we fixed $\bar{n}_e$ at $10^{13}\,\mathrm{m^{-3}}$. The computations showed that the variation of $\bar{n}_e$ does not affect the qualitative predictions of the model. Equations (1)-(7) with the boundary conditions were discretized using the finite-difference method and solved iteratively (the problem was reduced to a boundary-value problem for the governing equations).

The computations were performed for the following conditions: $a_d = 1\,\mu\mathrm{m}$, $\varphi_d = -4\,\mathrm{V}$, $p_g = 37\,\mathrm{Pa}$. The electron temperature, T_e, was assumed to be constant throughout the discharge and is set to 4 eV. This value was chosen based on the results of simulations performed in [16] for an rf-discharge with large amount of microparticles. Note that the electron temperature in this case is higher than that for a microparticle-free discharge (T_e is about 3 eV for an rf-discharge in pure argon). The normalized microparticle potential, $e|\varphi_d|/k_\mathrm{B}T_e$, is equal to one in this case (this is a typical value for the conditions of our study). The electron mobility and diffusion coefficient were calculated using Bolsig+ code [44] at a given electron temperature. The cross-sections from Biagi database were used [45]. The effect of the microparticles on the electron distribution function was neglected. The above conditions were chosen to match the experimental conditions. The other parameters of the model are specified separately for the results presented in subsection 4.3.

4.2. Plasma emission

In order to qualitatively assess the phase-resolved emission pattern in the bulk plasma, we consider the simplified electron energy equation:

$$\frac{\partial \varepsilon_e}{\partial t} = \mu_e(\varepsilon_e)\bar{E}(x,t)^2 - S_e(\varepsilon_e), \tag{9}$$

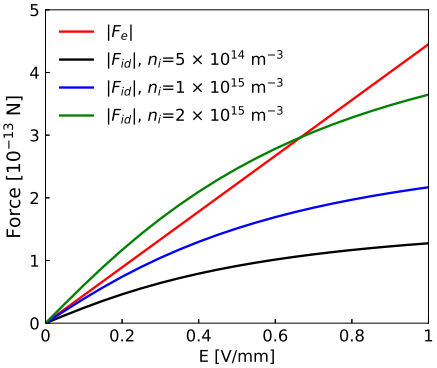

Figure 11. The electric force (F_e) and the ion drag force (F_{id}) acting on a single microparticle for the case of the ion drift flow. The ion drag force is shown for typical values of the ion density.

where t is time, $\varepsilon_e(x,t)$ is the mean electron energy and S_e is the energy losses due to elastic and inelastic processes (computed using Bolsig+ solver). The electric field in equation (9) is approximated as

$$\bar{E}(x,t) = E(x) + E_0 \sin(\omega t), \tag{10}$$

where $E(x)$ is the time-averaged field given by equation (7) and E_0 is the amplitude of the oscillating rf field (here, $\omega/2\pi = 13.56\,\mathrm{MHz}$). The amplitude of the oscillating field was set to $E_0 = 1\,\mathrm{V\,mm^{-1}}$ (characteristic value that is used in all computations). Certainly, equation (9) cannot be used close to the electrodes. Nevertheless, for the bulk plasma, this simplified model can be expected to provide a qualitatively correct description of the electron energy variation. Equation (9) was solved numerically using the second-order Runge-Kutta method.

Using the solution of equation (9), we estimate the time-space dependence of the total excitation rate for the $2p_1$ and $2p_5$ argon levels, which are the upper levels of the 750.4 and 751.5 nm transitions used in the experiment for the RF-period-resolved measurements. The excitation rate is given by $R_{ex} = k_{ex}(\varepsilon_e) n_g n_e$, where the rate coefficient k_{ex} is calculated using the Bolsig+ solver. The emission pattern was calculated by the convolution of the total excitation rate and the decay function $\exp(-t/\tau)$, with $\tau = 23\,\mathrm{ns}$ being the characteristic lifetime of the transition.

4.3. Modelling results

Before discussing the modelling results, it is helpful to consider the balance between the electric force ($F_e = q_d E$) and the ion drag force acting on a single microparticle. The balance between these two forces is supposed to play a major role in determining the microparticle suspension configuration. Since the ion velocity in the discharge is usually close to the local drift velocity for the considered conditions [40], both forces can be considered as functions of the uniform electric field causing the respective mobility-limited ion flow.

In figure 11, we show the electric force and the ion drag force computed as functions of the electric field, where the ion drag force is presented for typical values of the background ion density (under the assumption that $n_i = n_e$). As seen in figure 11, there are regimes where the equilibrium point ($|F_e| = |F_{id}|$) exists, and where $|F_e| > |F_{id}|$ for the entire considered range of electric fields. The existence of the equilibrium point is usually associated with the formation of a central void in the microparticle suspension. In the opposite regime (where $|F_e| > |F_{id}|$), the microparticles are expected to be uniformly distributed in the discharge [16].

Consider, first, the case when the condition $|F_{id}| > |F_e|$ is not satisfied in the bulk plasma. If the averaged dust density is set to $\bar{n}_d = 7 \times 10^{10}\,\mathrm{m}^{-3}$, this regime is reproduced by the model for $G_0 < 6.5 \times 10^{20}\,\mathrm{m}^{-3}\,\mathrm{s}^{-1}$ at $\theta = 0.2$ (these values are taken as an example). In figure 12(a), we present the results of computations for $G_0 = 5.2 \times 10^{20}\,\mathrm{m}^{-3}\mathrm{s}^{-1}$. As shown in figure 12(a), the microparticles are distributed almost uniformly. The suspension is confined by the electric field in the sheath region. In the central region, the production of ions due to ionization is balanced by the absorption of ions on the microparticles ($G_{ion} \approx G_d$). As a result, the ion velocity and averaged electric field are almost zero here. Qualitatively, this picture corresponds to the result of previous simulations obtained using one-dimensional models for similar conditions [16, 46].

Consider now the case when the condition $|F_{id}| > |F_e|$ is satisfied in the bulk plasma. In figure 12(b), we present the results obtained for $G_0 = 10 \times 10^{20}\,\mathrm{m}^{-3}\mathrm{s}^{-1}$. As it is seen in figure 12(b), the central void is reproduced by the model. The microparticle configuration is mainly determined by the balance between F_e and F_{id}. Here, $|F_{id}| > |F_e|$ in the void region and $|F_e| > |F_{id}|$ in the sheath region. These two regions provide the confinement of the microparticle suspension. The equilibrium condition, $|F_d| \approx |F_e|$, holds within the microparticle suspension.

The estimated emission patterns for the results shown in figure 12(a–b) are presented in figures 13(a), (d), respectively. In addition, in figure 13(c), we show the emission pattern for the intermediate case taken at $G_0 = 7.5 \times 10^{20}\,\mathrm{m}^{-3}\mathrm{s}^{-1}$. The electric field distributions corresponding to the results presented in figure 13 are shown in figure 14.

The emission pattern in figure 13(a) is almost uniform and correlates with the experimental observations at low discharge powers, when no void is present. The uniformity of the emission pattern is explained by the fact that the time-averaged electric field is almost zero in the bulk plasma. The results shown in figures 12(a) and 13(a) are in qualitative agreement with the results of particle-in-cell simulations presented in [16]. The emission pattern in figure 13(d) correlates with the experimental observations at elevated discharge powers (the case of a bright void). The maximum of the emission intensity in the bulk region is located at the void boundary. This correlates with the corresponding distribution of the electric field shown in figure 14.

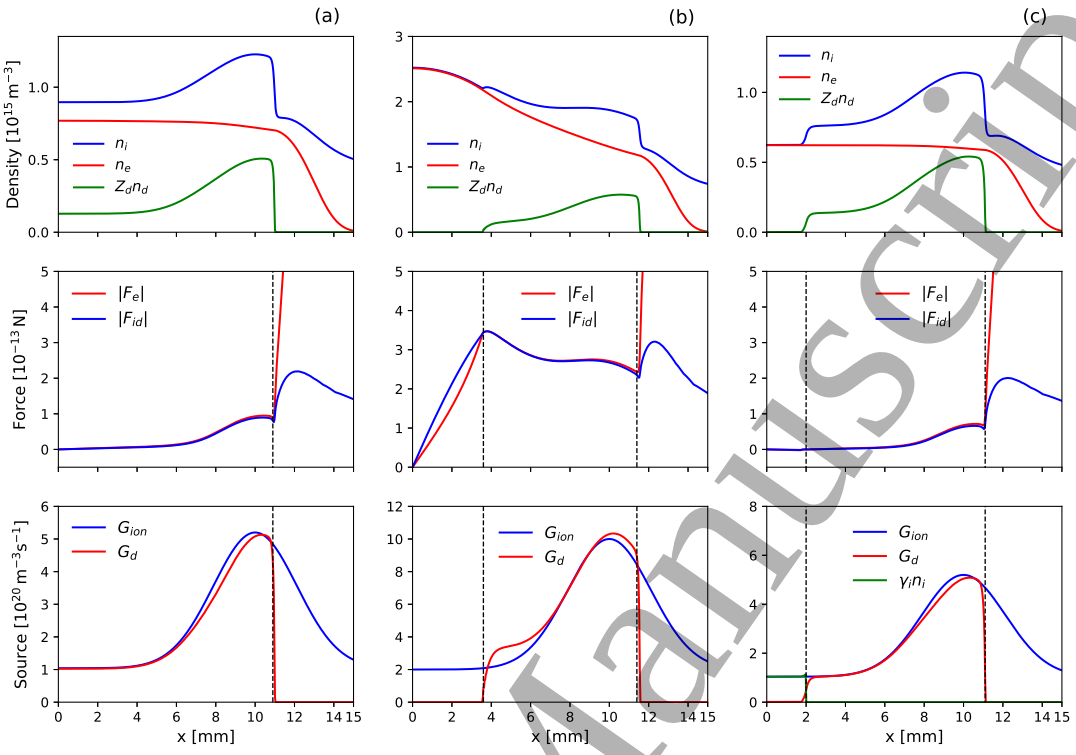

Figure 12. The computation results for $G_0 = 5.2 \times 10^{20}\,\mathrm{m^{-3}s^{-1}}$ (a), $G_0 = 10 \times 10^{20}\,\mathrm{m^{-3}s^{-1}}$ (b) and $G_0 = 5.2 \times 10^{20}\,\mathrm{m^{-3}s^{-1}}$, $\gamma_i = 1.67 \times 10^5\mathrm{s^{-1}}$ (c) : density profiles, distribution of the electric and ion drag forces, distribution of the ionization and sink terms. The dashed lines show the boundaries of the microparticle suspension.

4.4. The effect of radial diffusion

The emission pattern in figure 13(c) could probably explain the experimental observations in the case of a dim void. In fact, the electric field is almost uniformly distributed within the microparticle suspension in this case. Thus, the emission intensity at the void boundary is approximately at the same level as in the cloud. Moreover, the experimental picture is obviously affected by the emission from the outer discharge regions, where the microparticles are distributed uniformly (as it was discussed in [16], this argumentation should be taken with care).

At the same time, the emission pattern observed for the case of a dim void is similar to that shown in figure 13(a). The emission pattern is not noticeably affected by the presence of the void in this regime. This observation is similar to that reported previously in [16]. Thus, it is questionable that the results in figure 13(c) can reliably explain the experimental observations for the case of a dim void. This, in turn, indicates that there exists another mechanism of the void formation at low discharge powers. Below, we discuss the results which could provide a hint to such a mechanism.

First, it should be noted that 1D model described in subsection 4.1 does no take into account the loss of ions due to radial diffusion. At the same time, the rate of

this process in dust-free plasma can be comparable to that of ionization and absorption of ions by the microparticles. In fact, the second order expansion of the ion density near the discharge axis can be written as $n_i(r) = n_{i0}\,[1 - \delta(r/r_0)^2]$, where n_{i0} is the on-axis ion density, r is the radial coordinate, r_0 is the characteristic length in the radial direction and δ is the relative density drop. For pure plasma, the loss rate due to radial diffusion can be estimated as $(D_a/r)d/dr(rdn_i/dr)_{r\to 0} \approx -4D_a\delta n_{i0}/r_0^2$, where $D_a \approx \mu_i D_e/\mu_e$ is the ambipolar diffusion coefficient (here $\mu_i = e/(m_i n_g \sigma_0 u_0)$ is the ion mobility). For the conditions of our study we get $D_a \approx 4\,\mathrm{m^2\,s^{-1}}$. Taking, for example, $r_0 = 5\,\mathrm{mm}$ (characteristic radius of the dim void), $n_{i0} = 10^{15}\,\mathrm{m^{-3}}$ and $\delta = 16\%$ we get $4D_a\delta n_{i0}/r_0^2 \approx 10^{20}\,\mathrm{m^{-3}\,s^{-1}}$. This value is comparable with typical values of G_{ion} and G_d in figure 12(a).

In order to assess the possible effect of radial ion diffusion on the microparticle arrangement, we consider the modified ion continuity equation:

$$\frac{\partial}{\partial x}(n_i u_i) = G_{ion} - G_d - \gamma_i n_i, \tag{11}$$

where $\gamma_i n_i$ simulates the loss of ions due to radial diffusion. The remaining equations of the model are the same as described in section 4.1.

The general trend observed in different simulations is that $G_{ion} \approx G_d$ in the microparticle suspension (see figures 12(a–b), and the results in [16, 46]), and the ion flow tends to be divergence-free. This is taken into account by setting $\gamma_i = 0$ within the microparticle cloud. On the other hand, if we assume, that there is a microparticle-free region $x \le x_v$, where $\gamma_i \neq 0$ and $G_{ion} = \gamma_i n_i$, then n_d can become zero in this region, i.e., the void is formed. It is remarkable that our model can indeed reproduce such a configuration. In figure 12(c), we show the results obtained for $G_0 = 5.2 \times 10^{20}\,\mathrm{m^{-3}\,s^{-1}}$, $\gamma_i = 1.67 \times 10^5\,\mathrm{s^{-1}}$ and $x_v = 2\,\mathrm{mm}$ ($\gamma_i = 0$ for $x > x_v$). The solution shown in figure 12(c) represents a stable configuration with the microparticle-free region in the center. The electric force is positive in the void and dominates over the negative ion drag force. This explains the stability of the void in this regime.

In addition, it should be emphasized that the electric force (and consequently the electric field) at the void boundary is lower than that shown in figure 12(b) by two orders of magnitude. Thus, it is clear that this electric field has no noticeable effect on the emission picture at the discharge axis. This is visible in figure 13(b), where we demonstrate the emission pattern estimated for the solution presented in figure 12(c). The emission pattern in figure 13(b) correlates with the experimental results at moderate discharge powers (the case of a dim void). Thus, it can be hypothesized that the dim void observed in the present work corresponds to the microparticle configuration shown in figure 12(c). At the same time, inclusion of the radial diffusion for the conditions of the bright void does not lead to qualitative changes.

The novel void formation mechanism demonstrated above can be physically explained as follows. The gradient of the ion density in the cloud is determined by the distribution of the microparticle number density (this is also true in the radial direction). The ion flux in the radial direction can be relatively low since $G_{ion} \approx G_d$

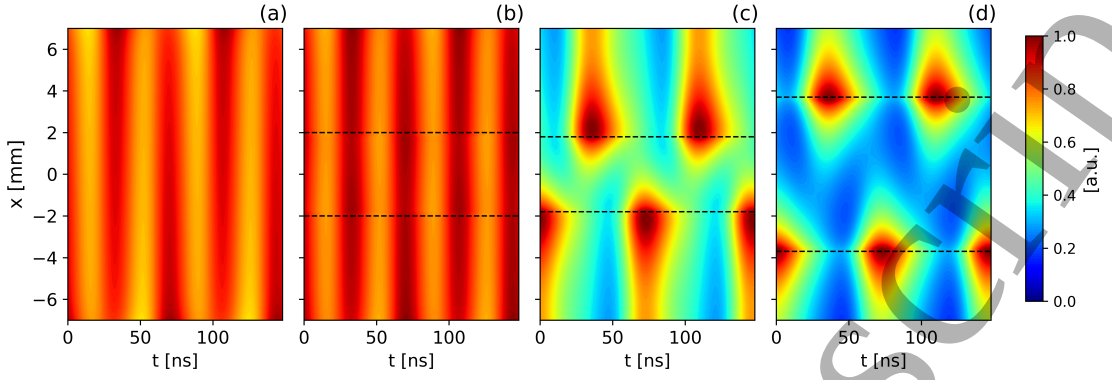

Figure 13. The simulated spatio-temporal emission patterns in the bulk plasma region. The results are presented for different values of the parameter G_0: (a, b) $5.2 \times 10^{20}\,\mathrm{m^{-3}s^{-1}}$, (c) $7.5 \times 10^{20}\,\mathrm{m^{-3}s^{-1}}$, (d) $10 \times 10^{20}\,\mathrm{m^{-3}s^{-1}}$. The pattern (b) was obtained taking into account the radial ion diffusion, $\gamma_i = 1.67 \times 10^5 \mathrm{s^{-1}}$. The dashed lines show the positions of the void edges.

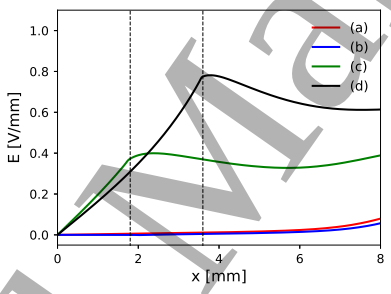

Figure 14. Distributions of the time-averaged electric field for the emission patterns presented in figures 13(a), (b), (c) and (d), respectively. The dashed lines show the position of the void edge.

inside the microparticle suspension. This is not true in the microparticle free region, where the radial gradient of n_i is inevitably connected with the formation of the radial ion flux. Therefore, it can be expected that the solution shown in figure 12(c) is realistic, at least near the discharge axis. It is clear, however, that this hypothesis can only be confirmed (or rejected) by rigorous two-dimensional modelling studies or by direct local measurements of electric fields and ion velocity distributions.

5. Conclusion

We have experimentally shown that the void (microparticle-free area) in the center of a capacitively-coupled rf complex plasma has two regimes, which we call "dim" and "bright". The dim void forms at relatively low discharge powers and exhibits no emission feature associated with it. With the increase of the discharge power, the bright emission from the void appears, i.e. the void experiences a transition from dim to bright regime. With further discharge power increase, the plasma emission concentrates near the void

boundaries, especially at higher gas pressure.

The transition between the regimes has a discontinuous character. The threshold is manifested by a kink in the void size power dependencies. Also, the microparticle density peak at the void boundary disappears with the power growth.

RF-period-resolved optical emission spectroscopy revealed that the presence of the microparticles increases the emission in the entire axial extension of the discharge every half of the period in the case of the dim void, whereas for the bright void, the emission increase appears only between the expanding sheath and the opposite void boundary.

The bright void is reproduced by the time-averaged 1D fluid model. The bright emission in the void is caused by the strong time-averaged electric field at the void boundary. In this case, the void boundary stabilizes as a result of the balance of ion drag and electrostatic forces. This balance can only be satisfied at the elevated discharge power.

On the contrary, the dim void could not be obtained within the framework of the same 1D model: the bright void was closing with the decrease of the ionization rate as soon as the ion drag force was unable to balance the electrostatic force. Dim void could be, however, obtained by artificially including the radial diffusion term into the ion flux continuity equation. Assuming radial diffusion term to be comparable to the ionisation and microparticle sink terms in a certain range of axial positions around the discharge midplane allowed to obtain a microparticle-free region, whose boundary is stabilized by the week electrostatic forces. Electric field at the void boundary was in this case two orders of magnitude lower than that in the bright void regime. Therefore, it did not lead to the appearance of the emission on the void boundary. The modified model was able to qualitatively explain the experimentally observed dim void formation as well as the respective experimentally measured RF-period-resolved spatiotemporal emission profile. At the same time, inclusion of the radial diffusion for the conditions of the bright void did not lead to qualitative changes.

Such an approach could qualitatively reproduce the void formation and the RF-period-resolved emission patterns in case of dim and bright void. We could therefore, demonstrate that the void in dim and bright void regimes forms due to two different mechanisms. Complete understanding of the dark void formation requires a self-consistent 2D model and local measurements of the electric field or ion velocity distribution.

Acknowledgments

We would like to thank Dr. S. Khrapak for helpful discussions and Dr. C. Knapek for careful reading of our manuscript and valuable suggestions.

The PK-3 Plus chamber was funded by the space agency of DLR with funds from the federal ministry for economy and technology according to a resolution of the Deutscher Bundestag under grants No. 50WP0203, 50WM1203. A. Pikalev acknowledges the financial support of Deutscher Akademischer Austauschdienst (DAAD) with funds from

Deutsches Zentrum für Luft- und Raumfahrt e.V. (DLR).

Appendix A. Characterization of the microparticle-plasma interaction

The sink term due to absorption of ions by the microparticles is given by

$$G_d = n_d J_i, \tag{A.1}$$

where J_i is the ion current collected by a single microparticle. The ion current is computed using the model presented in [47]:

$$J_i = J_{\mathrm{OML}} + \left[J_{\mathrm{coll}} - J_{\mathrm{OML}}\right](R_0/l_{ia}), \tag{A.2}$$

where J_{OML} is the current derived from the orbital-motion-limited (OML) theory [48], J_{coll} is the current related to the ion-atom collisions, l_{ia} is the mean free path for the ion-atom collisions, R_0 is the characteristic length scale of the perturbed plasma region around the microparticle. Here, $J_{\mathrm{OML}} = \sqrt{8\pi}a_d^2 n_i \upsilon_i (1 - e\varphi_d/k_{\mathrm{B}}T_g)$ and $J_{coll} = \sqrt{8\pi}R_0^2 n_i \upsilon_i$, where $\upsilon_i = \sqrt{k_{\mathrm{B}}T_g/m_i}$. The mean free path l_{ia} is estimated as $l_{ia} = 1/(n_g\bar{\sigma})$, where $\bar{\sigma} = 1.32 \times 10^{-18}\,\mathrm{m}^2$ is the characteristic cross-section at the collision energy of $k_{\mathrm{B}}T_g$ (the cross-sections are taken from [49]). The ions are assumed to interact with the microparticle via the Yukawa potential with the screening length λ_s. In this case, the ratio R_0/λ_s is given by the root of the nonlinear equation $\beta\exp(-\xi) = \xi$, where $\beta = (e|\varphi_d|/k_{\mathrm{B}}T_g)(a_d/\lambda_s)$.

The ion drag force is calculated using the well-known expression [1]:

$$F_d = \alpha\, m_i n_i \int \upsilon_x \upsilon \sigma(\upsilon) f(\vec{v}) d\vec{v}, \tag{A.3}$$

where $\vec{v}$ is the ion molecular velocity ($\upsilon = |\vec{v}|$), $f(\vec{v})$ is the ion velocity distribution function, σ is the momentum transfer cross section for the ion-dust collisions, α is the correction factor accounting for the effect of ion-atom collisions. The ion distribution function is given by the distribution for the drift flow with constant electric field [50,51]. The cross section σ is taken as the momentum transfer cross section for the attractive Yukawa potential [52]. The correction factor α was estimated using the approximate expression presented in [51] (namely, equation (33) in [51]). For the conditions of our study we get $\alpha \approx 1.4$ (this coefficient depends weakly on the ion velocity). Using equation (A.3), the ion drag force was calculated as a function of u_i and coupling parameter β.

The effective screening length for the Yukawa potential is defined using the following approximate expression [53]:

$$\lambda_s^{-2} = \lambda_{\mathrm{D}e}^{-2} + \tilde{\lambda}_s^{-2}\left[1 + (u_i/\upsilon_i)^2\right]^{-1}, \tag{A.4}$$

where $\lambda_{\mathrm{D}e} = \sqrt{e^2 n_e/\varepsilon_0 k_{\mathrm{B}}T_e}$ is the electron Debye radius and $\tilde{\lambda}_s$ is the screening length for the isotropic case ($u_i \to 0$). The screening length for the isotropic case is defined as [54]: $\tilde{\lambda}_s = \lambda_{\mathrm{D}i}\sqrt{1 + 0.48\sqrt{\beta_i}}$, where $\beta_i = (e|\varphi_d|/k_{\mathrm{B}}T_g)(a_d/\lambda_{\mathrm{D}i})$ and $\lambda_{\mathrm{D}i} = \sqrt{e^2 n_i/\varepsilon_0 k_{\mathrm{B}}T_g}$ is

the ion Debye radius.

The thermophoretic force is evaluated using the conventional expression [1]:

$$F_{th} = -\frac{8\sqrt{2\pi}}{15}\frac{a_d^2}{\upsilon_a}\lambda_a\frac{\partial T_a}{\partial x}, \tag{A.5}$$

where T_a is the temperature of the gas atoms, λ_a is the thermal conductivity and $\upsilon_a = \sqrt{k_\mathrm{B}T_g/m_a}$, with m_a being the atom mass. Here T_a is assumed to be close to T_g. The thermal conductivity of argon is taken as 17.8 $\mathrm{mW\,m^{-1}\,K^{-1}}$ [55].

The distribution of T_a is expressed as $T_a = \bar{T}_a + \tilde{T}_a$, where $\bar{T}_a$ is the linear temperature distribution between the electrodes and $\tilde{T}_a$ is the solution of the heat conduction equation in the interelectrode region with zero boundary conditions. We assume that F_{th} corresponding to the linear term $\bar{T}_a$ is balanced by the gravity force. Thus, the nontrivial contribution of F_{th} to the force balance given by equation (4) is related to the second term $\tilde{T}_a$. The distribution of $\tilde{T}_a$ is found by solving the heat conduction equation:

$$\lambda_a\frac{d^2\tilde{T}_a}{dx^2} = Q_d, \tag{A.6}$$

where $d\tilde{T}_a/dx = 0$ at $x = 0$ (the symmetry condition), $\tilde{T}_a = 0$ at $x = L$, and Q_d is the heat source due to the heat exchange between the gas and the dust particles. As it was discussed in [56], the effect of Q_d is not negligible for the conditions of our study (moreover, Q_d dominates over the contribution from the heat exchange between atoms and electrons). In this work, we estimate Q_d as follows [57]:

$$Q_d = n_d\pi a^2\sqrt{\frac{8}{\pi}\frac{p_g\upsilon_a}{2}\frac{\gamma+1}{\gamma-1}}\left(\frac{T_p}{T_g}-1\right), \tag{A.7}$$

where T_p is the microparticle surface temperature and $\gamma = 5/3$. The particle temperature can be estimated by considering the balance of heat fluxes at the particle surface [58, 59]. For the conditions of our study, this estimate gives $(T_p - T_g)/T_g \approx 0.2 - 0.5$. For simplicity, we used the fixed value $(T_p - T_g)/T_g = 0.2$ in all computations. Equation (A.6) was solved numerically using the finite difference method.

In the case without the void, the microparticle heating induces $F_{th} \sim 10^{-15}\,\mathrm{N}$ at $x = 2\,\mathrm{mm}$. Elastic collisions with the electrons induce the thermophoretic force one order of magnitude smaller.

References

[1] Fortov V, Ivlev A, Khrapak S, Khrapak A and Morfill G 2005 *Phys. Rep.* **421** 1–103

[2] Morfill G E and Ivlev A V 2009 *Rev. Mod. Phys.* **81**(4) 1353–1404

[3] Ivlev A, Löwen H, Morfill G and Royall C P 2012 *Complex Plasmas and Colloidal Dispersions: Particle-Resolved Studies of Classical Liquids and Solids* (*Series in Soft Condensed Matter* vol 5) (World Scientific Publishing Co. Pte. Ltd.)

[4] Nefedov A P, Morfill G E, Fortov V E, Thomas H M, Rothermel H, Hagl T, Ivlev A V, Zuzic M, Klumov B A, Lipaev A M, Molotkov V I, Petrov O F, Gidzenko Y P, Krikalev S K, Shepherd W, Ivanov A I, Roth M, Binnenbruck H, Goree J A and Semenov Y P 2003 *New Journal of Physics* **5** 33–33

[5] Thomas H M, Morfill G E, Fortov V E, Ivlev A V, Molotkov V I, Lipaev A M, Hagl T, Rothermel H, Khrapak S A, Suetterlin R K, Rubin-Zuzic M, Petrov O F, Tokarev V I and Krikalev S K 2008 *New J. Phys.* **10** 033036

[6] Pustylnik M Y, Fink M A, Nosenko V, Antonova T, Hagl T, Thomas H M, Zobnin A V, Lipaev A M, Usachev A D, Molotkov V I, Petrov O F, Fortov V E, Rau C, Deysenroth C, Albrecht S, Kretschmer M, Thoma M H, Morfill G E, Seurig R, Stettner A, Alyamovskaya V A, Orr A, Kufner E, Lavrenko E G, Padalka G I, Serova E O, Samokutyayev A M and Christoforetti S 2016 *Review of Scientific Instruments* **87** 093505

[7] Land V and Goedheer W J 2008 *New Journal of Physics* **10** 123028

[8] Schmidt C, Arp O and Piel A 2011 *Physics of Plasmas* **18** 013704

[9] Stefanović I, Sadeghi N, Winter J and Sikimic B 2017 *Plasma Sources Science and Technology* **26** 065014

[10] Bouchoule A and Boufendi L 1993 *Plasma Sources Science and Technology* **2** 204

[11] Bouchoule A and Boufendi L 1994 *Plasma Sources Science and Technology* **3** 292–301

[12] Tachibana K, Hayashi Y, Okuno T and Tatsuta T 1994 *Plasma Sources Science and Technology* **3** 314

[13] Fridman A A, Boufendi L, Hbid T, Potapkin B V and Bouchoule A 1996 *Journal of Applied Physics* **79** 1303–1314

[14] Mitic S, Pustylnik M Y and Morfill G E 2009 *New Journal of Physics* **11** 083020

[15] Killer C, Bandelow G, Matyash K, Schneider R and Melzer A 2013 *Phys. Plasmas* **20** 083704

[16] Pustylnik M Y, Semenov I L, Zähringer E and Thomas H M 2017 *Phys. Rev. E* **96**(3) 033203

[17] Lipaev A M, Khrapak S A, Molotkov V I, Morfill G E, Fortov V E, Ivlev A V, Thomas H M, Khrapak A G, Naumkin V N, Ivanov A I, Tretschev S E and Padalka G I 2007 *Physical Review Letters* **98**(26) 265006

[18] Annaratone B M, Khrapak S A, Bryant P, Morfill G E, Rothermel H, Thomas H M, Zuzic M, Fortov V E, Molotkov V I, Nefedov A P, Krikalev S and Semenov Y P 2002 *Physical Review E* **66**(5) 056411

[19] Goree J, Morfill G E, Tsytovich V N and Vladimirov S V 1999 *Phys. Rev. E* **59**(6) 7055–7067

[20] Tsytovich V N, Vladimirov S V, Morfill G E and Goree J 2001 *Physical Review E* **63**(5) 056609

[21] Tsytovich V N, Vladimirov S V and Morfill G E 2004 *Physical Review E* **70**(6) 066408

[22] Vladimirov S V, Tsytovich V N and Morfill G E 2005 *Physics of Plasmas* **12** 052117

[23] Gozadinos G, Ivlev A V and Boeuf J P 2003 *New Journal of Physics* **5** 32

[24] Akdim M R and Goedheer W J 2003 *Physical Review E* **67**(6) 066407

[25] Land V and Goedheer W J 2007 *New Journal of Physics* **9** 246

[26] Goedheer W J and Land V 2008 *Plasma Physics and Controlled Fusion* **50** 124022

[27] Goedheer W J, Land V and Venema J 2009 *Journal of Physics D: Applied Physics* **42** 194015

[28] Goedheer W J, Land V and Venema J 2009 *Contributions to Plasma Physics* **49** 199–214

[29] Tawidian H, Diop F, Lecas T, Gibert T and Mikikian M 2013 Void behavior and profile using laser induced fluorescence *40th EPS Conference on Plasma Physics* (Espoo, Finland) p P1.304

[30] Samsonov D and Goree J 1999 *Physical Review E* **59**(1) 1047–1058

[31] Schulze M, von Keudell A and Awakowicz P 2006 *Plasma Sources Science and Technology* **15** 556–563

[32] Lagrange J F, Géraud-Grenier I, Faubert F and Massereau-Guilbaud V 2015 *Journal of Applied Physics* **118** 163302

[33] Mikikian M, Couëdel L, Cavarroc M, Tessier Y and Boufendi L 2007 *New Journal of Physics* **9** 268

[34] Pustylnik M Y, Ivlev A V, Sadeghi N, Heidemann R, Mitic S, Thomas H M and Morfill G E 2012 *Physics of Plasmas* **19** 103701

[35] Rothermel H, Hagl T, Morfill G E, Thoma M H and Thomas H M 2002 *Physical Review Letters* **89**(17) 175001

[36] Schwabe M, Hou L J, Zhdanov S, Ivlev A V, Thomas H M and Morfill G E 2011 *New Journal of*

Physics **13** 083034
[37] Wiese W L, Brault J W, Danzmann K, Helbig V and Kock M 1989 *Physical Review A* **39**(5) 2461–2471
[38] Sarkar S, Mondal M, Bose M and Mukherjee S 2015 *Plasma Sources Science and Technology* **24** 035007
[39] Brinkmann R 2011 *J. Phys. D: Appl. Phys.* **44** 042002
[40] Semenov I 2017 *Phys. Rev. E* **95** 043208
[41] Khrapak S, Khrapak A, Ivlev A and Thomas H 2014 *Phys. Plasmas* **21** 123705
[42] Khrapak S, Khrapak A, Ivlev A and Morfill G 2014 *Phys. Rev. E* **89** 023102
[43] Khrapak S A and Thomas H M 2015 *Phys. Rev. E* **91** 023108
[44] Hagelaar G and Pitchford L 2005 *Plasma Sources Sci. Technol.* **14** 722
[45] Biagi database, private communication, www.lxcat.net, retrieved on July 15, 2020
[46] Sukhinin G, Fedoseev A, Antipov S, Petrov O and Fortov V 2013 *Phys. Rev. E* **87** 013101
[47] Khrapak S, Ratynskaia S V, Zobnin A, Usachev A, Yaroshenko V, Thoma M, Kretschmer M, Höfner H, Morfill G, Petrov O *et al.* 2005 *Phys. Rev. E* **72** 016406
[48] Khrapak S and Morfill G 2009 *Contrib. Plasma Phys* **49** 148–68
[49] Phelps A V 1994 *J. Appl. Phys.* **76** 747–53
[50] Patacchini L and Hutchinson I H 2008 *Phys. Rev. Lett.* **101** 025001
[51] Hutchinson I and Haakonsen C 2013 *Phys. Plasmas* **20** 083701
[52] Khrapak S 2014 *Phys. Plasmas* **21** 044506
[53] Khrapak S, Ivlev A, Zhdanov S and Morfill G 2005 *Phys. Plasmas* **12** 042308
[54] Semenov I, Khrapak S and Thomas H 2015 *Phys. Plasmas* **22** 053704
[55] Lemmon E W and Jacobsen R T 2004 *Int. J. Thermophys* **25** 21–69
[56] Pikalev A, Pustylnik M, Räth C and Thomas H 2020 *J. Phys. D: Appl. Phys.* **53** 075203
[57] Liu F, Daun K, Snelling D R and Smallwood G J 2006 *Appl. Phys. B* **83** 355–82
[58] Swinkels G, Kersten H, Deutsch H and Kroesen G 2000 *J. Appl. Phys.* **88** 1747–55
[59] Khrapak S and Morfill G 2006 *Phys. Plasmas* **13** 104506

Heartbeat instability as auto-oscillation between dim and bright void regimes

A. Pikalev,* M. Pustylnik, C. Räth, and H. M. Thomas
Institut für Materialphysik im Weltraum, Deutsches Zentrum für Luft- und Raumfahrt e. V. (DLR), 82234 Weßling, Germany

(Received 9 April 2021; revised 30 August 2021; accepted 4 October 2021; published 26 October 2021)

We investigated the self-excited as well as optogalvanically stimulated heartbeat instability in RF discharge complex plasma. Three video cameras measured the motion of the microparticles, the plasma emission, and the laser-induced fluorescence simultaneously. Comprehensive studies of the optogalvanic control of the heartbeat instability revealed that the microparticle suspension can be stabilized by a continuous laser, whereas a modulated laser beam induces the void contraction either transiently or resonantly. The resonance occurred when the laser modulation frequency coincided with the frequency of small breathing oscillations of the microparticle suspension, which are known to be a prerequisite to the heartbeat instability. Based on the experimental results we suggest that the void contraction during the instability is caused by an abrupt void transition from the dim to the bright regime [Pikalev *et al.*, Plasma Sources Sci. Technol. **30**, 035014 (2021)]. In the bright regime, a time-averaged electric field at the void boundary heats the electrons causing bright plasma emission inside the void. The dim void has much lower electric field at the boundary and exhibits therefore no emission feature associated with it.

DOI: 10.1103/PhysRevE.104.045212

I. INTRODUCTION

Complex or dusty plasma is a medium containing ionized gas and micron-sized solid particles [1–3]. The strongly coupled subsystem of such microparticles can be used for particle resolved studies of generic classical phenomena in condensed matter. For such studies, homogeneous microparticle suspensions are desirable. However, even microgravity does not guarantee homogeneous distribution and stability of the microparticle component. A void, i. e., a microparticle-free area, is one of most common disturbances of the complex plasma homogeneity under microgravity conditions. The void formation and growth also determine the nanoparticle generation cycle in plasma reactors [4].

Due to its small charge-to-mass ratio and its mesoscopic nature, the dust component introduces a variety of instabilities including dust density waves [5], transverse instability [6], filamentary mode and the void rotation [7–9], plasmoids and carousel instability [10,11]. Because of their multi-time-scale character, the instabilities in complex plasma pose a hard problem for numerical studies. The physical mechanism of most of these instabilities is still unknown.

In the first microgravity experiments with complex plasmas, a spontaneous periodic contraction of the void boundary was reported [12]. Because of its characteristic appearance as well as due to very low repetition frequency (from single contractions to hundreds Hz), this phenomenon was termed "heartbeat" instability. This particular instability is the subject of the present work.

The heartbeat instability is a complex auto-oscillation phenomenon, which was treated in Ref. [13] as mixed-mode oscillations. Mixed-mode oscillations occur when a dynamical system switches between fast and slow motion and small and large amplitude [14]. The mixed-mode oscillations are encountered in a wide range of phenomena including glow discharges [15,16], chemical processes [17,18], models of neuronal activity [19] and the real mammal heartbeat [20].

The heartbeat instability was investigated in microgravity conditions on board the International Space Station [21,22], in experiments with grown nanoparticles [13,23–25] and with the thermophoretic gravity compensation [26]. These experiments showed that oscillations of the discharge electrical parameters and the plasma emission are inherent in the heartbeat instability. Just before every void contraction, a short bright flash appears in the void. In some experiments, small oscillations of the plasma emission and the electrical signals occurs between the void contractions [13,24]. The heartbeat instability is sensitive to the amount and size of the microparticles, the gas pressure, and the discharge power making it difficult to reproduce the instability quantitatively. Such phenomena as "trampoline effect" [27] and "delivery instability" [28] seem to be qualitatively similar to the heartbeat instability. In Ref. [26], the heartbeat instability was resonantly stimulated by modulating the ionization rate with a tunable laser. It remained, however, unclear, which oscillatory mode of the void was excited by the tunable laser.

The heartbeat instability represents a very complex process involving the microparticle-plasma interactions. Despite several attempts to explain the heartbeat instability theoretically [21,26,29], its physical mechanism is still unclear. Understanding of this phenomenon is essential for the physics of microparticle-plasma interactions and the void formation. It needs a comprehensive model of the microparticle dynamics coupled with plasma conditions. For such a model, understanding of the void formation mechanism is required.

It is commonly supposed that the void in complex plasmas is formed due to a balance between the electrostatic and the ion drag forces with the ion flow from the void into the

*Aleksandr.Pikalev@dlr.de

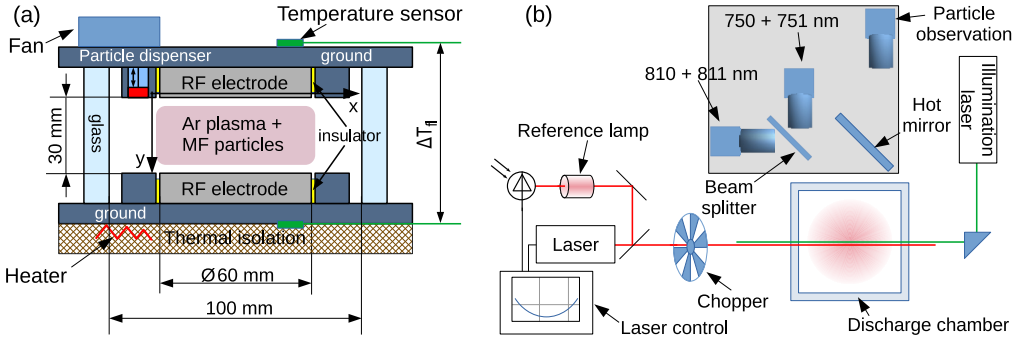

FIG. 1. Scheme of the experimental setup, (a) side view, (b) top view. The heart of the experiment is the PK-3 Plus chamber [34]. The bottom flange of the chamber can be heated to control the temperature gradient between the electrodes. The cameras observe the microparticle motion and plasma emission. The reference Ar lamp is used to control the wavelength of the tunable laser.

microparticle suspension [27,29–31]. However, this mechanism cannot explain the void formation at low discharge powers [32,33]. The experiment and the model in Ref. [33] demonstrated that the void can exist in one of two regimes depending on the discharge power. The so-called bright void regime corresponds to the conditions with higher RF discharge power and is characterized by the bright emission inside the void. In this case, strong time-averaged electric field at the top and the bottom void boundaries heats up the electrons enhancing the ionization and the emission. The mechanical stability of the boundary is in this case indeed determined by the balance of electrostatic and ion drag forces. The dim void regime corresponds to relatively low discharge power conditions and is characterized by the diffuse emission profile inside and around the void. The transition between the regimes has a discontinuous character. After the void formation, its size is almost independent of the discharge power in the dim regime, but the bright void grows rapidly with the discharge power increase after the transition. A simplified time-averaged one-dimensional (1D) fluid model in Ref. [33] could reproduce the dim void only when the radial ion losses were artificially introduced into the microparticle-free region of the plasma. In this case, the force balance on the top and bottom void boundaries could be satisfied for low plasma density and with much weaker time-averaged electric field.

Combining the comprehensive investigation of the optogalvanic control of the heartbeat instability with the concept of dim and bright void, we decompose the entire heartbeat process into several stages, which can be investigated separately.

II. EXPERIMENT

The experiments were conducted in the ground-based PK-3 Plus chamber (see Fig. 1) [34]. The plasma was produced by means of a capacitively coupled RF discharge. Two electrodes were driven in a push-pull mode by a sinusoidal signal with the frequency of 13.56 MHz. We used two types of melamine formaldehyde spheres with the diameters of 1.95 μm and 2.15 μm as microparticles. During a particular experiment, the microparticles of one of these types were injected into the discharge by an electromagnet-driven dispenser through a sieve.

Argon was fed into the chamber with 3-sccm gas flow during the entire experiment. We mainly investigated the heartbeat instability with the gas pressure of 36 Pa. We also observed the heartbeat instability at the pressures of 20 and 55 Pa. In the case of lower pressure, other instabilities [7,8,11] made the discharge behavior complex and difficult to interpret. In the case of higher pressure, gas friction made the heartbeat less pronounced.

Under ground laboratory conditions, the microparticles concentrate themselves in the vicinity of the lower electrode. To obtain large volumetric microparticle suspensions, we compensated the gravitational force by means of thermophoresis [35]. The temperature gradient between the electrodes was controlled by heating the bottom flange with an electric heater and cooling the top flange with fans. A symmetrical void position was achieved with the temperature difference between the flanges of 14–15 K for the 1.95 μm diameter microparticles and 15–17 K for the 2.15 μm diameter microparticles.

The microparticles were illuminated by a laser sheet with the wavelength of 532 nm. Three Ximea MQ042RG-CM video cameras with interference bandpass filters captured the microparticle motion and the plasma emission in the same discharge area. The filters had the central wavelengths of 532, 750, and 810 nm, respectively, and the width of transmission band of the filters was about 10 nm. Hence, one plasma glow observation camera captured the plasma radiation in 750.4 and 751.5 nm spectral lines, these lines correspond to the transitions $2p_1 \rightarrow 1s_2$ and $2p_5 \rightarrow 1s_4$ in the Paschen notation, respectively. Another camera captured the light in 810.4 and 811.5 nm spectral lines, which correspond to the transitions $2p_7 \rightarrow 1s_4$ and $2p_9 \rightarrow 1s_5$, respectively. The spatial resolution of the cameras was about 37 μm/pixel. The frame rate of the cameras was 200 fps. The video capture of all three cameras was started by the software approximately at the same time. The difference between the time stamps of the frames with the same number was less than the duration of a single frame. All three cameras were focused on the central cross section of the discharge chamber.

We used the optogalvanic effect [36,37] induced by the Toptica DL Pro laser for the investigation of the void stability [26]. The width of the laser spectral line was less than 1 MHz. The power of the laser beam entering the plasma chamber was about 50 mW, and its diameter was 2 mm. The laser was tuned to the 772.38 nm transition of argon and scanned the spectral range of about 220 MHz in the vicinity of its center

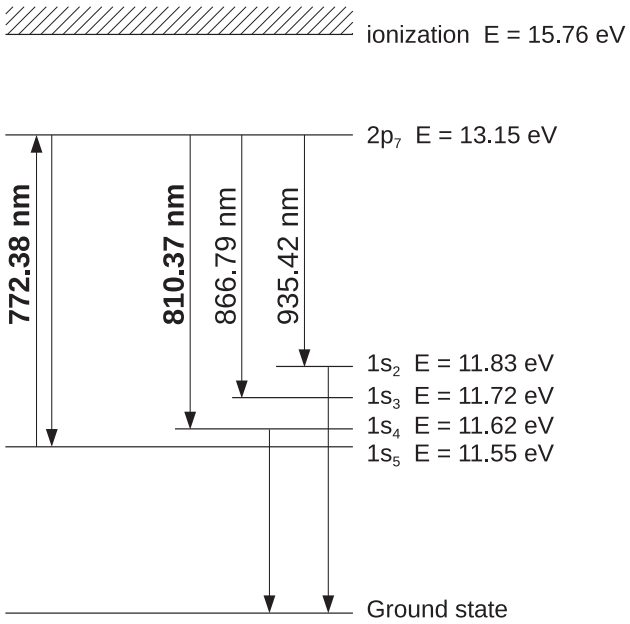

FIG. 2. Electronic levels of argon involved in the optogalvanic effect. The laser pumps the transition at 772.38 nm and fluorescence in the 810.37-nm spectral line is observed.

with the repetition frequency of 100 Hz. A small fraction of the laser light passed though a reference argon lamp to control the scanning range. A mechanical chopper was used to modulate the laser beam. The laser light induced the fluorescence in the 810.4 nm spectral line (see Fig. 2), which was used to match the laser modulation with the video frames.

At the beginning of every experiment, after stabilization of the temperature gradient, we set the discharge power to 500 mW and injected the microparticles till the onset of the heartbeat instability. The parameters of the instability, such as its frequency, the threshold discharge power of the instability onset, and necessary laser parameters for the optogalvanic control, drifted on the time scales of minutes making the measured quantities difficult to reproduce. Such evolution of the conditions is typical for complex plasma experiments [38]. However, the qualitative effects reported in this paper are well reproducible.

III. RESULTS

A. Self-excited instability

The self-excited heartbeat instability existed within a certain range of the discharge power and the gas pressure and required relatively high density of the microparticle suspension. An example of the heartbeat self-excitation region in pressure–discharge power space was published in Ref. [26]. This region was expanding with the increase of the amount of microparticles.

At the lower discharge power boundary of the instability range, the void underwent sporadic contractions with strong variation of the void size, while near the higher power boundary, the void size variation was decreasing with the increase of the discharge power, until the oscillations became undetectable. For example, in one experiment with the microparticle diameter of 2.15 μm, the heartbeat appeared as the sporadic contractions at the discharge power of 500 mW with the variation of the void cross-section area between 31 and 7 mm^2. After the discharge power was increased to 750 mW, the void cross-section area oscillated between 30 and 27 mm^2 with the frequency of 26 Hz. In other our experiments, the lower discharge power of the heartbeat self-excitation was 300–600 mW, and the oscillations became invisible for the discharge powers higher than 800 mW.

The reported experiments were conducted near the lower power boundary, where the instability onset had the threshold character and the void oscillations were well pronounced. In the experiments with the self-exited heartbeat instability, the amount of microparticles only slightly exceeded the instability onset threshold.

Similarly to Ref. [21], we obtained the spatiotemporal distributions (periodograms) of the microparticle velocity. First, we calculated the velocities v_x using OpenPIV code [39] in cells 32 × 32 pixels with 50% overlap. Then, for every frame, we averaged the velocities along the vertical direction in a horizontal stripe with the width of four cells. The stripe was located at the height of the void [see Fig. 3(a)]. The obtained horizontal velocity profiles were stacked into a spatiotemporal distribution [see an example in Fig. 3(c)].

In a similar way, x and y distributions of emission intensity were obtained by stacking the profiles of the averaged emission intensities across the respective narrow stripes. The directions of x and y axes are shown in Fig. 1(a). In order to obtain the emission variation, the time-averaged intensity was subtracted. The emission variations for the filter with the central wavelength of 750 nm in horizontal and vertical directions (I^x_{750} and I^y_{750}, respectively) are presented in Fig. 3(c). Just before the void contraction, the plasma glow shortly flashed in the void [see Figs. 3(b) and 3(c) and movie_fig3.avi in Supplemental Material [40]]. The intensity at the flash maximum was 30–40% higher than the time-averaged value. At the same time, the discharge edge regions became darker. After that, the emission decreased in the contracted void, whereas the emission from the edge regions increased above the level before the flash. This effect was already reported in several works [23–26]. The plasma emission measured with 750- and 810-nm filters behaved similarly. If the amount of microparticles in the suspension was slightly below the instability onset threshold, the spatial distribution of plasma emission was diffuse. Therefore, in this case, the void was in the dim regime (in the terminology of Ref. [33]).

Small oscillations of the microparticle motion and the plasma emission are visible in the spatiotemporal distributions between the large void collapses. They were termed "failed contractions" in Refs. [24,25]. In the velocity spatiotemporal distributions, a small slope of the oscillations can be seen, which suggests that the oscillation propagated from the discharge edges to the center. In our paper, we would therefore refer to them as to "breathing oscillations".

B. Optogalvanic control

We will describe the effects of the optogalvanic control of the heartbeat instability using the three spatiotemporal distributions: the distributions of v_x and I^x_{750} as in Fig. 3(c) and

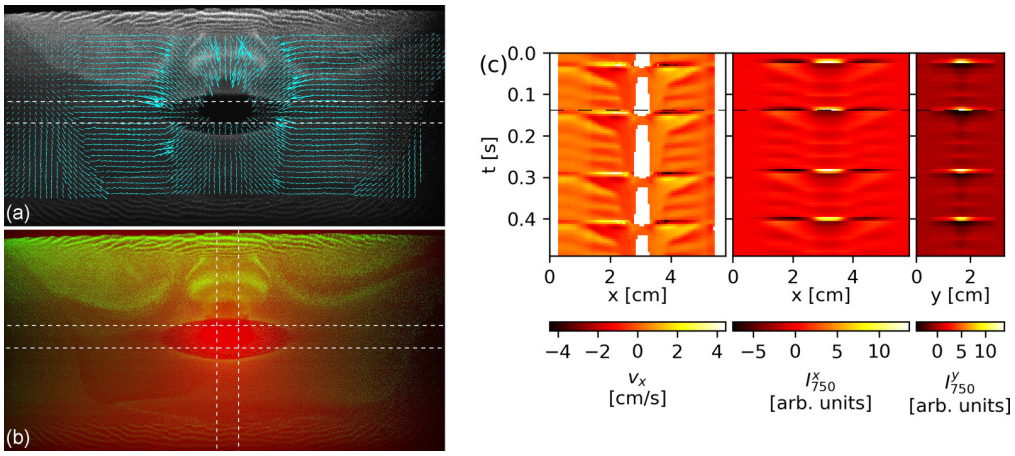

FIG. 3. Self-excited heartbeat instability. (a) One of the frames with the velocity field reconstructed using the OpenPIV software [39]. (b) The same frame with superimposed images of (green) the microparticle suspension and (red) the plasma emission captured with the filter with the central wavelength of 750 nm. The dashed lines in plates (a) and (b) depict the areas used for the calculation of the spatiotemporal distributions. (c) Spatiotemporal distributions of the velocity v_x and the plasma emission variations I^x_{750} and I^y_{750} during the self-excited heartbeat instability. The white color in the v_x plot depicts the areas in which no microparticles are present. The black dashed lines depict the temporal position of the frames shown in plates (a) and (b). The microparticle diameter was 2.15 μm, the discharge power was 400 mW. See also Supplemental Material [40].

additionally x distribution of the emission intensity variation for the filter with the 810-nm central wavelength I^x_{810}. The I^x_{810} distribution shows the periods when the laser was open or closed in the experiments with the modulated laser due to the laser-induced fluorescence (see Fig. 2). In all cases, these distributions were obtained in the same way using the technique described in Sec. III A.

1. Continuous laser

The continuous laser beam passing through the void stabilized the microparticle suspension. Without the laser, the heartbeat instability was present in the suspension. The frequency of the heartbeat instability in that case was 17.9 Hz [see Fig. 4(a)]. We modulated the laser with the frequency of 3.6 Hz. While the laser was closed, the heartbeat instability was observed in the suspension. However, once the laser was opened, the instability disappeared and only breathing oscillations being slowly damped remained visible. This effect is demonstrated in Fig. 4(b) and movie_4b.avi in the Supplemental Material [40]. The continuous laser beam stabilized the void completely, and no oscillations were visible [see Fig. 4(c)].

2. Transient stimulation

The laser beam could transiently, either on its opening or closing, excite the heartbeat instability in a stable microparticle suspension. If the laser beam passed through the void, the void collapse occurred just after the beam closing. The spatiotemporal distributions of the transient heartbeat stimulation are presented in Fig. 5 and corresponding movies are available in Supplemental Material [40]. In the case of the chopper frequency of 1.7 Hz [Fig. 5(a)], every closing of the beam caused the void collapse. Also, small breathing oscillations quickly damped after opening the beam are visible. For the chopper frequencies of 19.6 Hz [Fig. 5(b)] and 44.0 Hz [Fig. 5(c)], the void collapses occurred every two and every four laser pulses, respectively. It seems the void needs to reach a certain phase of expansion after the collapse to be ready for a new stimulated contraction.

At the same time, the chopper frequency must not be too low. In one experiment, the transiently induced contractions occurred with the chopper frequency of 4.6 Hz, but did not appear with the chopper frequency of 3 Hz.

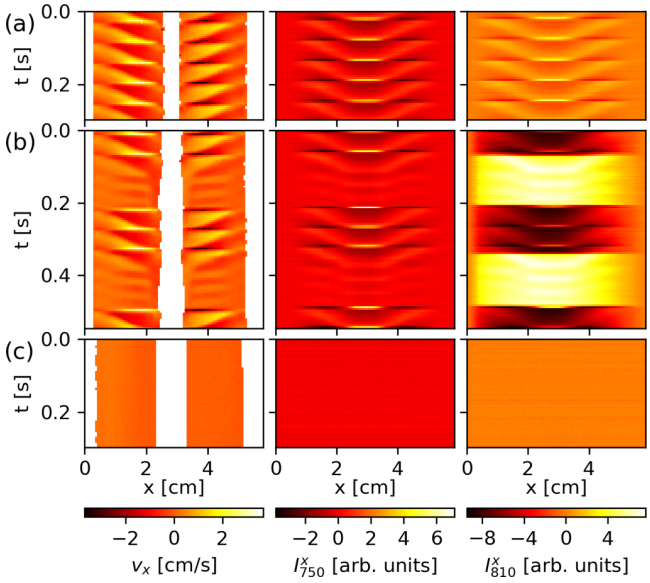

FIG. 4. The horizontal spatiotemporal distributions of the velocities v_x and the plasma emission variations I^x_{750} and I^x_{810} (a) without the laser, (b) with the modulated laser, and (c) with continuous laser. The diameter of the microparticles was 1.95 μm, the discharge power was 500 mW. See also Supplemental Material [40].

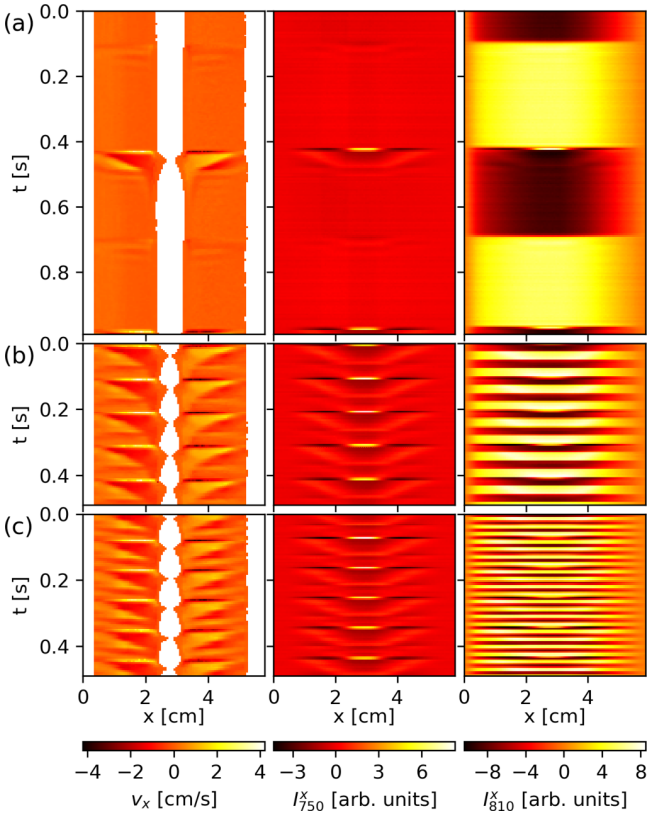

FIG. 5. Transient optogalvanic heartbeat excitation with the chopper frequency of (a) 1.7 Hz, (b) 19.6 Hz, (c) 44.0 Hz. The microparticle diameter was 1.95 μm, the discharge power was 500 mW. See also Supplemental Material [40].

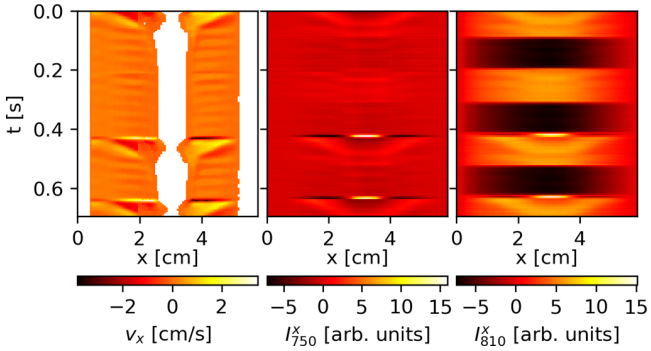

FIG. 7. Effect of the beam horizontal shift by 10 mm. The microparticle diameter was 2.15 μm, the discharge power was 500 mW.

To evaluate how the effect depends on the laser intensity, we equipped the chopper with neutral density filters of different transmission. The experiments showed that the further the suspension is from the self-excitation threshold, the higher laser power is necessary to stimulate the contraction. An example of the results is presented in Fig. 6. In this experiment, the measurements with the discharge power of 250 mW were performed 6 min after the measurements with the discharge power of 350 mW without injection of the microparticles in between.

If the laser beam was shifted horizontally from the void center to the distance of 1 cm, the void collapsed after the laser opening (see Fig. 7) in contrast with the experiments where the unshifted laser beam caused the void contraction after closing. We could not obtain this change of the void collapse phase with a vertical shift of the laser beam: the effect of the laser beam under or above the void became weaker, as it was reported in Ref. [26], and only rare void

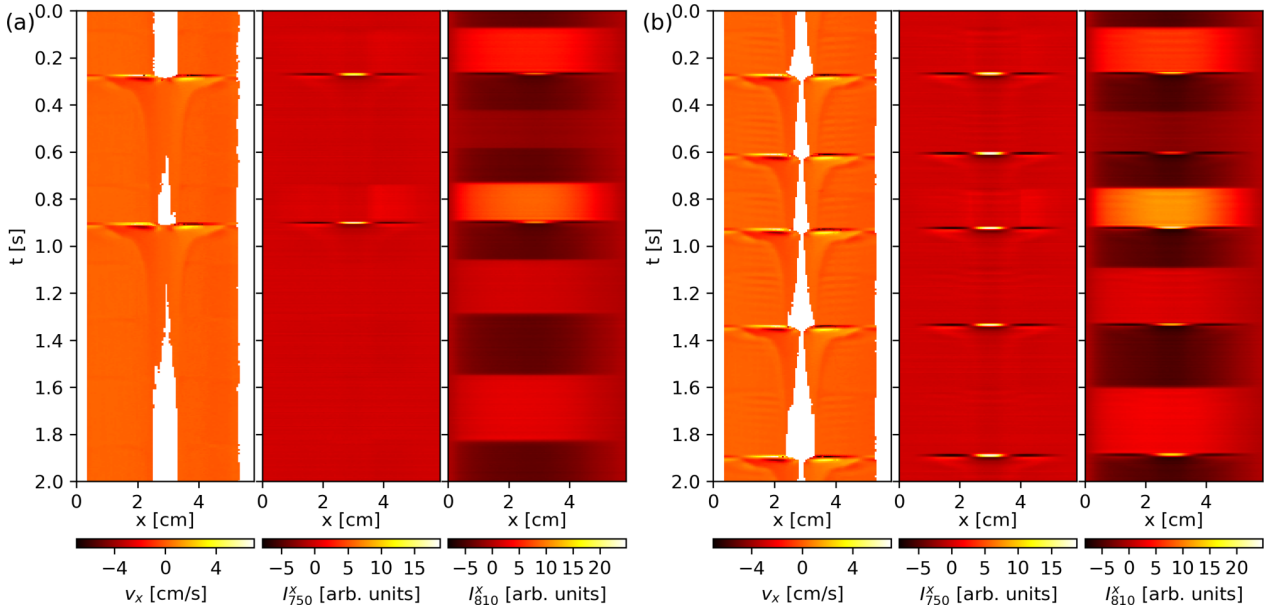

FIG. 6. Transient optogalvanic heartbeat excitation with the attenuated laser beam. The microparticle diameter was 1.95 μm, the discharge power was (a) 250 mW, (b) 350 mW. The bright stripes in the I^x_{810} distribution correspond to the time intervals when the laser was crossing the void through the filters with the following values of the transmission (from the top to the bottom): 0.45, 0.014, 1, 0.12, and 0.19.

contractions occurred, still after the laser closing. This difference between the horizontal and vertical shifts of the beam corresponds to the difference between horizontal and vertical spatiotemporal emission distributions during the flash [see Fig 3(c)].

3. Resonant stimulation

If the void contractions could not be induced transiently, the heartbeat instability could be stimulated resonantly. This effect was reported in Ref. [26]. It was discovered using the same laser and discharge chamber as in this work. An example of this effect is shown in Fig. 8. In the case of the lowest chopper frequency [Fig. 8(a)], small breathing oscillations, whose phase is disturbed by the modulated laser beam, are visible. Horizontally averaged Fourier spectra of the spatiotemporal distributions for this case are shown in Fig. 9(a). In this spectrum, mainly two modes are visible: The first one with the frequency of about 10 Hz corresponds to the laser modulation, whereas the second one with the frequency of about 29 Hz corresponds to the breathing oscillations. At higher chopper frequency, the microparticle suspension oscillated with the frequency of the laser modulation and low amplitude [Fig. 8(b)]. At the chopper frequencies close to the frequency of the breathing oscillations, the heartbeat instability occurred [see Figs. 8(c)–8(e) and movie_fig8d.avi in the Supplemental Material [40]]. The width of this resonance was several Hz.

The Fourier spectra for the spatiotemporal distributions in Fig. 8(d) are shown in Fig. 9(b). Mixing of the modulation frequency of 27.3 Hz with four times lower heartbeat frequency of 6.8 Hz leads to the frequency comb spectrum [41]. We note that the spectrum of the heartbeat instability observed in Refs. [13,23] also has a frequency comb character.

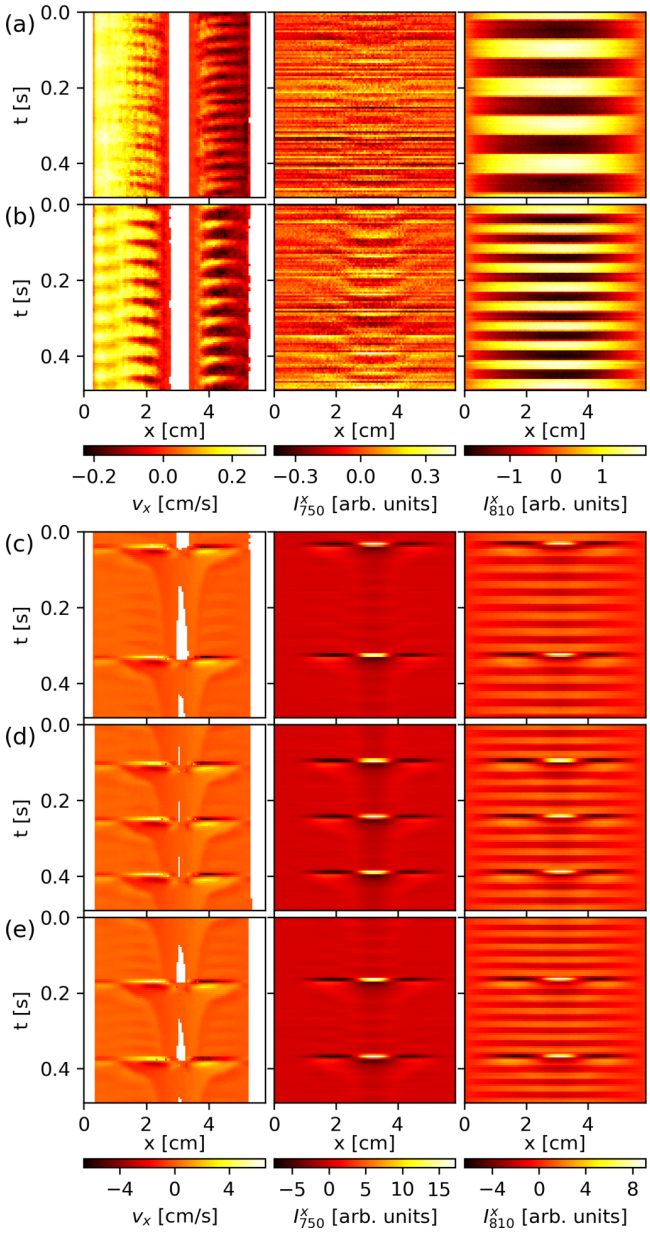

FIG. 8. Stimulation of the heartbeat instability with low laser power. The laser beam was attenuated down to 0.7 mW. The microparticle diameter was 2.15 μm, the discharge power was 350 mW. The laser modulation frequency was (a) 9.8 Hz, (b) 19.5 Hz, (c) 23.9 Hz, (d) 27.3 Hz, and (e) 29.5 Hz. See also Supplemental Material [40].

IV. DISCUSSION

A. Dim-to-bright void transition and void collapse

In Refs. [26], the heartbeat instability was supposed to occur due to a critical transformation on the void boundary from a smooth potential profile to the sheath. The sheath was suggested to appear when the microparticle number density reaches a certain value: When the amount of microparticles is small, they do not significantly disturb the plasma, and the potential profile across the void boundary should be smooth. If the suspension is however dense, the void boundary should act similarly to a solid surface, in front of which the sheath potential drop should occur. However, simulation with a 1D hybrid model and fixed microparticle distribution showed a linear growth of the electric field with increasing the microparticle number density without any critical phenomena [42]. According to recent findings [33], a steep growth of the electric field accompanies the transition between dim and bright void regimes. Since the heartbeat instability is accompanied by the flash inside the void, it is reasonable to suppose that the void contractions are caused by an abrupt transition between dim and bright void regimes.

This process is fast in comparison with the microparticle motion: In Ref. [26] the flash was measured with a photomultiplier and looked as a pulse with the duration of 5 ms and steep edges. In the experiments with growing nanoparticles, the flash duration of 2 ms was reported [24]. It leads therefore to the transient formation of a bright-void-like emission (and, consequently, ionization) profile under the plasma conditions of a dim void. Similar situation was considered in Ref. [32] using a 1D hybrid model: Simulations with a fixed microparticle distribution with a void resulted in a strong emission inside the void and uncompensated electrostatic forces pushing the microparticles to the void center.

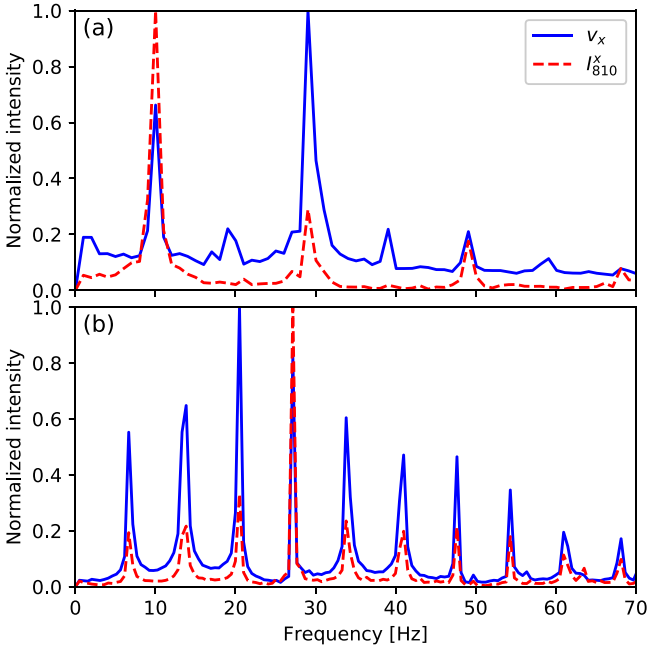

FIG. 9. Horizontally averaged Fourier spectra of v_x and I^x_{810} spatiotemporal distributions shown in (a) Fig. 8(a); (b) Fig. 8(d). The laser modulation frequency was (a) 9.8 Hz, (b) 27.3 Hz. Every spectrum is normalized to its maximal value.

B. Optogalvanic effect

In Ref. [33], it was pointed out that an increase of the ionization rate may switch the void from the dim to bright regime. The laser whose wavelength is tuned to the electron transition of the plasma forming gas atoms is capable of modifying the ionization rate in the plasma. This is the underlying mechanism of the optogalvanic effect [43,44]. The ionization energy of argon from the ground state is 15.76 eV [45], which is much higher than the electron temperature in our plasma ($T_e \sim 4$ eV, $n_e \sim 10^{15}$ m^{-3} [32,33]). The bottom state of the transition pumped by the laser is the lowest metastable level, which lies only 4.21 eV below the ionization energy. Although, after additional excitation by the laser, the atom can be ionized even easier, it can spontaneously relax to the ground state (see Fig. 2). The optogalvanic effect is therefore determined by the interplay between the growth of the ionization rate due to the increase in the population of the upper level of the laser-pumped transition and the decrease of the ionization due to the decrease in the population of the lower level of the laser-pumped transition. The sign of the effect depends on the experimental conditions. For example, nanosecond laser pulses in the 696.5 nm argon spectral line caused a decrease of ionization in a glow discharge [43], whereas much longer pulses (0.4 ms) in the same spectral line increased the ionization in a RF discharge [44].

In our case, the probability of the relaxation to $1s_2$ and $1s_4$ resonant states is one order of magnitude higher than the probability to relax to the $1s_3$ metastable state [46]. According to Ref. [43], a laser pulse in 772.38 nm argon spectral line caused a positive pulse of DC discharge voltage (at constant discharge current), which implies the decrease of the ionization rate. The laser-induced decrease of the ionization rate is consistent with the stabilization of the heartbeat instability by the continuous laser since the dim void condition corresponds to the lower ionization rate [33].

C. Laser control of the heartbeat instability

In the case of self-excited heartbeat instability, the transition from the dim to bright void regime is evidently mediated by the breathing oscillations: They are always seen as precursors of the heartbeat instability as pointed out also in Refs. [13,24]. The dim void formation requires significant radial ion losses [33], which could be modulated by the breathing oscillations. In the case of resonant optogalvanic stimulation of the heartbeat instability, the laser slightly modulates the ionization rate (as pointed out in Ref. [26]). The heartbeat instability is excited when the modulation frequency is close to the frequency of the breathing oscillations. Also, the breathing oscillations are damped, once the heartbeat instability is switched off by the continuous laser beam [see Fig. 4(c)].

During the transient heartbeat stimulation, the transition from dim to bright void occurs immediately after opening or closing the laser beam independent of the existence or phase of the breathing oscillations. We suppose that in this case, the ionization rate inside the void increases due to the transient processes in the plasma. If the laser beam passes though the void, its closing causes this increase directly. If the beam is shifted, a decrease of the ionization near the beam requires an ionization increase in other parts of the discharge.

V. CONCLUSION

The presented experiments reproduced earlier reported behavior of the plasma emission during the heartbeat instability, small breathing oscillations that appear in the suspension between the void contractions, and resonant optogalvanic stimulation of the instability. It was demonstrated that the resonance is observed when the laser modulation frequency coincides with the frequency of these breathing oscillations. The experiments with high laser power revealed that individual laser switching can cause the void contraction transiently. The void contracts after closing of the laser beam if it passes through the void center, and after opening of the laser beam if it was shifted horizontally to the void periphery. However, continuous laser beam stabilizes the microparticle suspension.

The experimental results allow us to describe the cycle of the heartbeat instability in the following way (Fig. 10): It starts from a microparticle suspension with a dim void. The void transits abruptly to the bright regime due to the breathing oscillations, whose amplitude grows beyond a critical value [24]. The transition can also be induced by a steep change of ionization rate by the laser or the laser working in resonance with the breathing oscillations. In the bright regime, the void boundary becomes mechanically unstable and the void collapses due to large electrostatic forces on its boundaries. After the collapse, the microparticles absorb the surplus of electrons and ions and move back restoring the dim-void configuration.

We were, therefore, able to identify a sequence of physical conditions the plasma acquires during the cycle of the heartbeat instability (green boxes in Fig. 10). However, most of

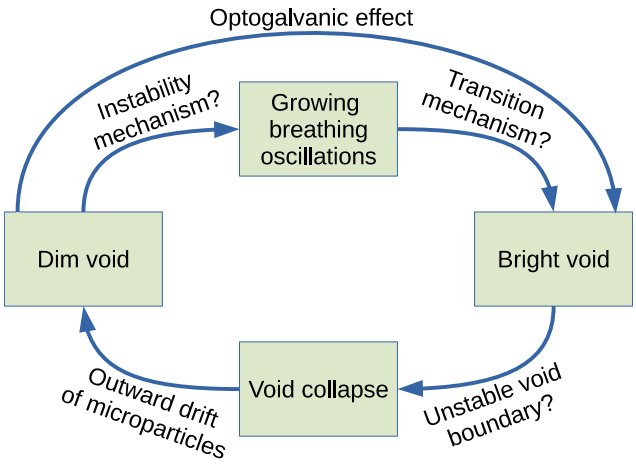

FIG. 10. Schematic representation of the heartbeat instability cycle. Initially dim void transits to the bright regime. This transition is mediated either by the breathing-oscillations-related mechanism or by the transient optogalvanic effect. The boundary of the bright void becomes unstable and the void collapses due to the electrostatic force prevailing over the ion drag and thermophoretic forces. The dim void recovers due to the outward drift of microparticles.

the transitions between them (arrows in Fig. 10) are still not clear. What is the self-excitation mechanism of the breathing oscillations in the dim void regime? How does their growth lead to the abrupt transition to the bright void regime? Why does the void boundary in the bright regime get mechanically unstable? What makes the microparticles move backward and form the dim void after the bright void collapse? In the discussion we suggested hypothetical mechanisms which could explain some of these transitions. They need to be proved by further investigations, theoretical as well as experimental.

As we already mentioned, the heartbeat instability is a multi-time-scale process. Its direct simulation is, therefore, computationally very expensive. Decomposing the heartbeat into stages allows us to model each of them individually. The optogalvanic control allows us to experimentally separate the void collapse from the breathing oscillations. This approach could be applied to other instabilities in complex plasmas.

ACKNOWLEDGMENTS

We thank Dr. V. Nosenko for careful reading of our manuscript. The PK-3 Plus chamber was funded by the space agency of the German Aerospace Center (DLR) with funds from the federal ministry for economy and technology according to a resolution of the Deutscher Bundestag under Grants No. 50WP0203 and No. 50WM1203. A. P. acknowledges the financial support of Deutscher Akademischer Austauschdienst (DAAD) with funds from DLR.

[1] V. E. Fortov, A. V. Ivlev, S. A. Khrapak, A. G. Khrapak, and G. E. Morfill, Complex (dusty) plasmas: Current status, open issues, perspectives, Phys. Rep. **421**, 1 (2005).

[2] G. E. Morfill and A. V. Ivlev, Complex plasmas: An interdisciplinary research field, Rev. Mod. Phys. **81**, 1353 (2009).

[3] A. Ivlev, H. Löwen, G. Morfill, and C. P. Royall, *Complex Plasmas and Colloidal Dispersions: Particle-Resolved Studies of Classical Liquids and Solids*, Series in Soft Condensed Matter (World Scientific, Singapore, 2012), Vol. 5.

[4] I. Pilch and F. Greiner, Diagnostics of void expansion during cyclic growth and formation of layered nanoparticle clouds, J. Appl. Phys. **121**, 113302 (2017).

[5] R. L. Merlino, 25 years of dust acoustic waves, J. Plasma Phys. **80**, 773 (2014).

[6] A. V. Zobnin, A. D. Usachev, A. M. Lipaev, O. F. Petrov, V. E. Fortov, M. Y. Pustylnik, H. M. Thomas, M. A. Fink, M. H. Thoma, and G. I. Padalka, Transverse ionization instability of the elongated dust cloud in the gas discharge uniform positive column under microgravity conditions, J. Phys.: Conf. Ser. **774**, 012174 (2016), XXXI International Conference on Equations of State for Matter (ELBRUS 2016) 1–6 March 2016, Elbrus, Russia.

[7] G. Praburam and J. Goree, Experimental observation of very low-frequency macroscopic modes in a dusty plasma, Phys. Plasmas **3**, 1212 (1996).

[8] D. Samsonov and J. Goree, Instabilities in a dusty plasma with ion drag and ionization, Phys. Rev. E **59**, 1047 (1999).

[9] M. Mikikian, M. Cavarroc, L. Couëdel, and L. Boufendi, Low frequency instabilities during dust particle growth in a radio-frequency plasma, Phys. Plasmas **13**, 092103 (2006).

[10] M. Mikikian, H. Tawidian, and T. Lecas, Merging and Splitting of Plasma Spheroids in a Dusty Plasma, Phys. Rev. Lett. **109**, 245007 (2012).

[11] M. Mikikian, L. Couedel, Y. Tessier, and L. Boufendi, Carousel instability in a capacitively coupled rf dusty plasma, IEEE Trans. Plasma Sci. **39**, 2748 (2011).

[12] J. Goree, R. Quinn, G. Morfill, H. Thomas, T. Hagl, U. Konopka, H. Rothermel, and M. Zuzic, Plasma dust crystallization, in *Proceedings of the 4th Microgravity Fluid Physics and Transport Phenomena Conference, Cleveland* (NASA, 1998), pp. 105–106.

[13] M. Mikikian, M. Cavarroc, L. Couëdel, Y. Tessier, and L. Boufendi, Mixed-Mode Oscillations in Complex-Plasma Instabilities, Phys. Rev. Lett. **100**, 225005 (2008).

[14] M. Brøns, T. J. Kaper, and H. G. Rotstein, Introduction to focus issue: Mixed mode oscillations: Experiment, computation, and analysis, Chaos **18**, 015101 (2008).

[15] T. Braun, J. A. Lisboa, and J. A. C. Gallas, Evidence of Homoclinic Chaos in the Plasma of a Glow Discharge, Phys. Rev. Lett. **68**, 2770 (1992).

[16] T. Hayashi, Mixed-Mode Oscillations and Chaos in a Glow Discharge, Phys. Rev. Lett. **84**, 3334 (2000).

[17] F. N. Albahadily, J. Ringland, and M. Schell, Mixed-mode oscillations in an electrochemical system. I. A Farey sequence which does not occur on a torus, J. Chem. Phys. **90**, 813 (1989).

[18] V. Petrov, S. K. Scott, and K. Showalter, Mixed-mode oscillations in chemical systems, J. Chem. Phys. **97**, 6191 (1992).

[19] J. Rubin and M. Wechselberger, Giant squid-hidden canard: The 3D geometry of the Hodgkin-Huxley model, Biol. Cybern. **97**, 5 (2007).

[20] B. van der Pol D.Sc. and J. van der Mark, LXXII. The heartbeat considered as a relaxation oscillation, and an electrical model of the heart, Philos. Mag. J. Sci. **6**, 763 (1928).

[21] S. K. Zhdanov, M. Schwabe, R. Heidemann, R. Sütterlin, H. M. Thomas, M. Rubin-Zuzic, H. Rothermel, T. Hagl, A. V. Ivlev, G. E. Morfill, V. I. Molotkov, A. M. Lipaev, O. F. Petrov, V. E. Fortov, and T. Reiter, Auto-oscillations in complex plasmas, New J. Phys. **12**, 043006 (2010).

[22] R. J. Heidemann, L. Couëdel, S. K. Zhdanov, K. R. Sütterlin, M. Schwabe, H. M. Thomas, A. V. Ivlev, T. Hagl, G. E. Morfill, V. E. Fortov, V. I. Molotkov, O. F. Petrov, A. I. Lipaev, V. Tokarev, T. Reiter, and P. Vinogradov, Comprehensive experimental study of heartbeat oscillations observed under microgravity conditions in the PK-3 Plus laboratory on board the International Space Station, Phys. Plasmas **18**, 053701 (2011).

[23] M. Mikikian and L. Boufendi, Experimental investigations of void dynamics in a dusty discharge, Phys. Plasmas **11**, 3733 (2004).

[24] M. Mikikian, L. Couëdel, M. Cavarroc, Y. Tessier, and L. Boufendi, Self-excited void instability in dusty plasmas: Plasma and dust cloud dynamics during the heartbeat instability, New J. Phys. **9**, 268 (2007).

[25] M. Mikikian, L. Couëdel, M. Cavarroc, Y. Tessier, and L. Boufendi, Threshold Phenomena in a Throbbing Complex Plasma, Phys. Rev. Lett. **105**, 075002 (2010).

[26] M. Y. Pustylnik, A. V. Ivlev, N. Sadeghi, R. Heidemann, S. Mitic, H. M. Thomas, and G. E. Morfill, On the heterogeneous character of the heartbeat instability in complex (dusty) plasmas, Phys. Plasmas **19**, 103701 (2012).

[27] M. Kretschmer, S. A. Khrapak, S. K. Zhdanov, H. M. Thomas, G. E. Morfill, V. E. Fortov, A. M. Lipaev, V. I. Molotkov, A. I. Ivanov, and M. V. Turin, Force field inside the void in complex plasmas under microgravity conditions, Phys. Rev. E **71**, 056401 (2005).

[28] L. Couëdel, M. Mikikian, A. A. Samarian, and L. Boufendi, Self-excited void instability during dust particle growth in a dusty plasma, Phys. Plasmas **17**, 083705 (2010).

[29] S. V. Vladimirov, V. N. Tsytovich, and G. E. Morfill, Stability of dust voids, Phys. Plasmas **12**, 052117 (2005).

[30] J. Goree, G. E. Morfill, V. N. Tsytovich, and S. V. Vladimirov, Theory of dust voids in plasmas, Phys. Rev. E **59**, 7055 (1999).

[31] A. M. Lipaev, S. A. Khrapak, V. I. Molotkov, G. E. Morfill, V. E. Fortov, A. V. Ivlev, H. M. Thomas, A. G. Khrapak, V. N. Naumkin, A. I. Ivanov, S. E. Tretschev, and G. I. Padalka, Void Closure in Complex Plasmas under Microgravity Conditions, Phys. Rev. Lett. **98**, 265006 (2007).

[32] M. Y. Pustylnik, I. L. Semenov, E. Zähringer, and H. M. Thomas, Capacitively coupled rf discharge with a large amount of microparticles: Spatiotemporal emission pattern and microparticle arrangement, Phys. Rev. E **96**, 033203 (2017).

[33] A. Pikalev, I. Semenov, M. Pustylnik, C. Räth, and H. Thomas, Dim and bright void regimes in capacitively coupled RF complex plasmas, Plasma Sources Sci. Technol. **30**, 035014 (2021).

[34] H. M. Thomas, G. E. Morfill, V. E. Fortov, A. V. Ivlev, V. I. Molotkov, A. M. Lipaev, T. Hagl, H. Rothermel, S. A. Khrapak, R. K. Suetterlin, M. Rubin-Zuzic, O. F. Petrov, V. I. Tokarev, and S. K. Krikalev, Complex plasma laboratory PK-3 plus on the International Space Station, New J. Phys. **10**, 033036 (2008).

[35] H. Rothermel, T. Hagl, G. E. Morfill, M. H. Thoma, and H. M. Thomas, Gravity Compensation in Complex Plasmas by Application of a Temperature Gradient, Phys. Rev. Lett. **89**, 175001 (2002).

[36] J. E. M. Goldsmith and J. E. Lawler, Optogalvanic spectroscopy, Contemp. Phys. **22**, 235 (1981).

[37] B. Barbieri, N. Beverini, and A. Sasso, Optogalvanic spectroscopy, Rev. Mod. Phys. **62**, 603 (1990).

[38] C. Killer, F. Greiner, S. Groth, B. Tadsen, and A. Melzer, Long-term spatiotemporal evolution of the dust distribution in dusty argon rf plasmas, Plasma Sources Sci. Technol. **25**, 055004 (2016).

[39] Z. J. Taylor, R. Gurka, G. A. Kopp, and A. Liberzon, Long-duration time-resolved PIV to study unsteady aerodynamics, IEEE Trans. Instrum. Meas. **59**, 3262 (2010); OpenPIV C++ with Qt frontend., Source code: https://github.com/OpenPIV/openpiv-c--qt.

[40] See Supplemental Material at http://link.aps.org/supplemental/10.1103/PhysRevE.104.045212 for videos with the data that were used to obtain Figs. 3, 4(b), 5, and 8(d).

[41] R. Holzwarth, T. Udem, T. W. Hänsch, J. C. Knight, W. J. Wadsworth, and P. S. J. Russell, Optical Frequency Synthesizer for Precision Spectroscopy, Phys. Rev. Lett. **85**, 2264 (2000).

[42] M. Y. Pustylnik, I. L. Semenov, and H. M. Thomas, Emission and microparticle arrangement in capacitavely coupled rf discharge, in *Asia-Pacific Conference on Plasma and Terahertz Science* (Xi'an, China, 2018).

[43] J. R. Nestor, Optogalvanic spectra of neon and argon in glow discharge lamps, Appl. Opt. **21**, 4154 (1982).

[44] D. E. Murnick, R. B. Robinson, D. Stoneback, M. J. Colgan, and F. A. Moscatelli, Optogalvanic signals from argon metastables in a rf glow discharge, Appl. Phys. Lett. **54**, 792 (1989).

[45] L. Minnhagen, Spectrum and the energy levels of neutral argon, Ar I, J. Opt. Soc. Am. **63**, 1185 (1973).

[46] W. L. Wiese, J. W. Brault, K. Danzmann, V. Helbig, and M. Kock, Unified set of atomic transition probabilities for neutral argon, Phys. Rev. A **39**, 2461 (1989).